FAST, SELECTIVE, AND STABLE HIGH TEMPERATURE HUMIDITY SENSORS ENABLED BY MICROFABRICATED YTTRIUM-DOPED BARIUM ZIRCONATE THIN FILMS

by

Xiaoxin Chen

A dissertation submitted to the faculty of
The University of Utah
in partial fulfillment of the requirements for the degree of

Doctor of Philosophy

Department of Electrical and Computer Engineering

The University of Utah

December 2010

The University of Utah Graduate School

STATEMENT OF DISSERTATION APPROVAL

The dissertation of **Xiaoxin Chen**

has been approved by the following supervisory committee members:

Mark S. Miller	, Chair	**10/13/2010** Date Approved
Loren W. Rieth	, Member	**10/13/2010** Date Approved
Eric Eddings	, Member	**10/18/2010** Date Approved
Anil Virkar	, Member	**10/15/2010** Date Approved
Michael Toepper	, Member	**n/a** Date Approved

and by **Gianluca Lazzi**, Chair of

the Department of **Electrical and Computer Engineering**

and by Charles A. Wight, Dean of The Graduate School.

ABSTRACT

This work tested the viability of microfabricated humidity sensors based on Y-doped $BaZrO_3$ by developing thin film deposition processes, fabricating devices, and characterizing the device response. At high temperatures, this material becomes conductive depending on temperature, water vapor, and other gas concentrations. Such devices should help increase efficiency and decrease emissions through improved combustion process control. Using microfabrication may lead to reduced size and faster sensor response. Two hundred and twelve variations of thin film layers were deposited and characterized out of which 112 were used in sensors.

$BaZrO_3$:Y thin films (200 – 750 nm) were sputtered onto oxidized n-type silicon substrates at room temperature from a ceramic target in an Ar sputtering ambient. Various deposition pressures and powers were used to correlate process parameters with film properties. Films were annealed at 800 and 1000°C (3 hours, air) and characterized by X-ray diffraction (XRD), atomic force microscopy (AFM), and X-ray photoelectron spectroscopy (XPS) to determine microstructure, surface morphology, and film composition. For comparison, 30 – 500 nm thick films were deposited onto identical substrates using PLD (various substrate temperatures) and characterized as deposited. Selected samples were annealed at 1000°C (3 hours in air) and characterized again. Transmission electron microscopy (TEM) of 30 and 50 nm PLD films confirmed the

particle sizes found by AFM of 19 – 25 nm. Although all layers show Barium deficiencies, stable process windows were established for sputtering and PLD close to stoichiometric compositions.

Sensors with the sensitive material deposited on top of the interdigitated test structure (IDE) showed no response to changes in humidity. Sensors with the IDE placed on top of the sensing film showed sensitive response, suggesting a strong surface dominated sensing effect. Ti/Pt as contact metal yielded an unrepeatable humidity response. Cr/Au gave sensitive, selective, and long term stable humidity response.

All films were exposed to varying partial pressures of water vapor, (400 to 650°C) with and without exhaust gas mixtures. Sensitivities of 0.2 to 62 atm^{-1} were demonstrated with tenfold selectivity towards other gases and sensor life time in excess of a year. Response times are 4 - 20 times faster than reports in literature.

TABLE OF CONTENTS

LIST OF TABLES

LIST OF FIGURES

ACKNOWLEDGMENTS

I would like to express my sincere appreciation to Dr. Mark Miller for his guidance, support and continuous encouragement throughout my graduate studies, no matter what impasse my work was hitting. He was a wonderful teacher. He helped me lay the foundations and learn not only how to be a good engineer, but also a better scientist. I would like to thank Dr. Loren Rieth for helping me to set up my experiments and teaching me to critically analyze and interpret results. I am grateful for the many opportunities I had to discuss my work with Dr. Anil Virkar, Dr. Eric Eddings, and Dr. Michael Toepper. All of them helped me broaden my perspectives on the field and this subject in particular.

A sincere thank you goes to all my former research group members and the Microfab staff: your constant support and encouragement provided a great framework and strong team which helped me get through the ups and downs of any research project: Srinivasan Kannan, Hannwelm Steinbach, Clayton Bulter, Mike Sorenson, Mike Orthner, Mahender Avula, Quirong Ruan, Xianzong Xie, Sandeep Negi, Raj Bhandari, Rohit Sharma, Kirk Hofeling, Sohee Kim, Asha Sharma, Prashant Tathireddy, Brian Baker, Tony Olsen, Paul Cole, Brian van Devener, Ian Harvey, and Monica Heaton: it was you who made the research fun.

I would like to thank Elsevier Publishers and the Sensors and Actuators Journal for allowing me to publish my papers in this dissertation. I would also like to gratefully

acknowledge the financial support from the U.S. Department of Energy through the National Energy Technology Laboratory NETL, contract number: DE-FC26-05NT42440 for this work.

I am eternally grateful to my parents, Peiyuan Li and Kefei Chen, for their endless understanding and love. I would like to thank Florian Solzbacher who accompanied me throughout the entire journey and has been encouraging me every step of my life.

CHAPTER 1

INTRODUCTION

Yttrium-doped barium zirconate (Y-doped $BaZrO_3$ or YBZO or $BaZr_xY_{1-x}O_{3-y/2}$, x = 0.2, y>0) thin films might enable microfabricated humidity sensors for use at high temperatures [1-6]. This material becomes conductive at high temperatures, typically above 500°C, with its conductivity depending on temperature, water vapor, and other gas concentrations. These characteristics open up a wide range of existing and potential new applications in industrial process control, energy, and automotive applications. Using microfabrication may lead to mass producible devices with comparable small dimensions. The use of thin film technology may also enable faster sensor response times.

Literature reports on these materials have focused primarily on bulk or thick film material prepared by ceramic techniques of a few microns to several millimeters thickness [1-2]. The present work studied Y-doped $BaZrO_3$ thin films of 30 to 750 nm thickness fabricated into sensors for measuring of relative humidity at high temperatures ($T \geq 400°C$). These efforts have sought to answer the following questions: (1) can this material be deposited/fabricated using thin film technologies and is this technique practical? (2) is the response and response time as good or better than observed in bulk material? (3) what are the mechanisms that govern the sensor response and do they differ from what is observed in bulk material?

The first section below gives a brief overview of current combustion process technologies, the role of humidity sensors in these processes, and the suitability of using perovskite materials such as YBZO. The second section surveys relevant gas sensors and materials, both commercially available devices and reported research devices. The additional opportunities define the research and engineering objectives for the study of Y-doped $BaZrO_3$ thin films in high temperature humidity sensors. The final section outlines

the organization of the dissertation.

1.1 Combustion processes and the role of humidity sensors with suitable materials

Fossil fuel power plants are major emitters of greenhouse gases, which according to the consensus of various scientific organizations, may have been one of the causes for global warming over the last 50 years [7]. Global power demands are expected to rise more than 60% by 2030. With the world-wide total of active coal plants over 50,000 and rising, the International Energy Agency estimates that fossil fuels will account for 85% of the energy market by 2030 [8]. Power generation using fossil fuels (coal, natural gas, or petroleum) generally requires a high temperature ($T \geq 500°C$) combustion process. Byproducts of power plant operation include formation of a number of gaseous species, whose discharge to the atmosphere is undesirable. These gaseous species include CO, CO_2, H_2O, H_2S, N_2, H_2S, NO_x and SO_2. The concentration and type of these gases are often determined by the combustion process and process control. In order to prevent incomplete combustion, intensive research is being conducted on investigating improved processes for increased burner efficiency, e.g., the “clean coal” program in the US. As more recent advances in “clean coal” technology, carbon capture and sequestration are being studied, capturing carbon dioxide emissions from coal-fired plants and permanently burying them in soil or underwater. Currently, there are more than 80 carbon capture and sequestration projects underway in the United States with major activities being conducted in Utah [9]. Sequestration technology has yet to be tested on a large scale and may not be a complete solution to reducing airborne pollution. Until then, monitoring and controlling combustion processes and exhaust gas concentrations could help increase

process efficiency.

Also, new emissions regulations that started in 2007 require a significant NO_x concentration reduction in all truck and car exhaust gases [10] and will see further tightening of the emissions standards by 2012. Thus, it is well recognized that control and monitoring of these gaseous species is critical. Cummins Engines Co. Inc, one of the largest manufacturers of mobile and stationary diesel engines projects the requirements for sensors accuracy to reach about 3 ppm with time constants of 30 seconds and operation temperatures of 800°C to satisfy the future emissions standards [11]. Usually, emissions are measured using continuous emission monitor systems (CEMs), which typically sample volumes of gas and measure composition, particulate matter outside the actual burner/boiler. In automotive applications, engines are optimized in development to run efficiently based on a number of parameters including the design of the combustion chamber, cylinder head and piston shape, ignition cycles, intake and outlet valve opening times, air/gas mixture, injection pressure, injection spray pattern and engine load. During operation/use of the engine, far less accurate measurements (10's to 1000's of ppm resolution, 2-10% accuracy) of only temperature, throttle, manifold air flow, oxygen content in exhaust (lambda sensor) and more recently NO_x and NH_3 in diesel engines have to suffice in helping control emissions and efficiency during changing load cycles. The engine management software adjusts parameters such as injection timing, valve timing accordingly within an allowable process window. A key challenge is that current sensor technology is not accurate enough to allow engine manufacturers to guarantee abiding by already defined future emissions standards because the allowable tolerances are starting to become smaller than the resolution and accuracy of the available

automotive sensors.

Stationary engines and combustors, e.g., as found in power plants, tend to be run at an optimum operating point and do not suffer from drastic load changes as found in an automotive engine. Hence they can be designed to run in a predefined parameter space, optimized to run efficiently and then left in that state without the immediate need for continuous close feedback control of the process. On a regular basis (every few weeks or months), lance probes are inserted into the combustion chamber, drawing gas and cooling it along the shaft of the lance before passing it to an analysis system. The analyzing techniques are varies with the gas species, e.g., a Zirconia sensor is used for measuring O_2, chemoluminescence is used for NO_x, UV/VIS (ultraviolet/visible spectroscopy) is used for SO_2, and NDIR (nondispersive infrared sensor) is used for CO/CO_2. In addition, out of spec test cycles are run to see how the plant responds to load changes or drift of parameters. A key problem with these technologies is that they are extractive, i.e., they require sampling and removal of a gas volume. Gas samples can condense if the sampling line is not temperature controlled, especially if humidity is present in the gas. The availability of in-situ sensors that could be placed at multiple locations inside a burner or boiler would allow a better understanding and 3D modeling of the combustion process and improved continuous monitoring or process parameters for improved emission and efficiency.

An attractive technical approach for these devices and materials is the integration of multiple sensors on a single array chip to achieve reliable, stable, high temperature, and gas mixture compatible sensors. In order to accurately measure a large variety of gaseous species and concentrations, the reliable measurement of water vapor is essential since the

water vapor can have a large impact on the accuracy of other gas measurements at high temperature [12].

Many examples of humidity sensors based on chemisorption (surface adsorption) of water vapor have been reported [3, 13-15], but often 1) lack selectivity towards NO_x, and O_2 at high temperature [16-19], and 2) exist only in bulk material or thick film forms [1-2]. To be suitable for high temperature humidity sensors, the materials must have suitable conductivity (i.e., neither too low nor too high) and high selectivity towards water vapor. Perovskite oxides are particularly attractive for high temperature applications because of their 1) high melting and decomposition temperature, 2) microstructure and morphological stability, improving the reliability and long-term sensor performance at high temperatures, 3) ionic conductivity across different temperature ranges, and 4) an atomic structure with two differently sized cations that are suitable for a variety of dopants and that allow the control of the electrical transport and catalytic properties of the material to optimize sensor performance for specific applications [20].

Data obtained from doping perovskites, such as $BaCeO_3$, $SrCeO_3$, and $BaZrO_3$ suggest that these materials can exhibit proton conductivity and could be used in a variety of electrochemical devices including fuel cells, gas sensors, and hydrogen pumps [21-22]. The earliest studies of doped $BaZrO_3$ showed a poor conductivity of less than 50 μS/cm compared with doped $BaCeO_3$ which could be as high as 10 mS/cm at 600°C [23-25]. In 1999, Kreuer reported the conductivity of YBZO to be 50 μS/cm at only 140°C [26], which was confirmed by Bohn and Schober [27]. In later publications, Kreuer noted that Y-doped $BaZrO_3$ combines not only high proton conductivity with excellent mechanical

strength, but also has chemical stability under CO_2-containing atmospheres [28], which is highly relevant for combustion monitoring applications. Wang and Virkar investigated the electrical conductivity at various partial pressures oxygen and water in the temperature range of 500 to 800°C of 7 wt% Y-doped $BaZrO_3$ bulk material (10 ~ 100 mS/cm) and have demonstrated high selectivity to humidity [1-2]. Therefore, Y-doped $BaZrO_3$ is a promising sensing material for high temperature humidity micro sensors allowing for 1) high melting temperature ~ 2600°C [29], 2) high conductivity (10 μS/cm ~ 10 mS/cm) [1, 20-27, 29-34], 3) excellent mechanical strength up to 86 GPa [35], and 4) high chemical stability in humid and CO_2-containing atmospheres [23].

1.2 Solid state gas sensors

The expression "Sensor" can refer to components also known as transducers, test heads, sensing elements, probes, etc. [36-37]. Two major applications of gas sensors are the detection of single gases (e.g., NO_x, CO, O_2, CH_4, H_2O, etc) and the monitoring of changes in the ambient (i.e., gas mixture). Solid state based conductivity or electrochemical micro gas sensors constitute one of the largest growing groups of micro gas sensors and are considered henceforth.

In this section, solid state gas sensors are divided into two groups, which are simple model metal oxide gas sensors (a binary compound of oxygen with another metal element) and mixed model metal oxide gas sensors (an oxide with 2 or more metal elements, e.g., perovskite oxide based gas sensors). The conduction mechanism could be electronic, ionic, or mixed depending on material composition.

1.2.1 Metal oxide based gas sensors

Simple metal oxides sensors, referred to as metal oxide based sensors in the rest of the thesis, are commercially available and mostly ZnO and SnO_2 based. Since the 1920s, studies have investigated the influence of the gas atmosphere on conductivity, free carrier mobility, surface potential, and work functions in (semiconductor) materials [38]. These investigations led to the understanding that the semiconductor material surface is highly sensitive to chemical reactions and resulted in the "theory of traps" by Brattain and Bardeen [39], the "boundary layer theory of chemisorption" by Engel and Hauffe as well as Schottky [40-43], and the "electron theory of chemisorption and catalysis on semiconductors" by Volkenstein [38, 44-45], which was expanded by Geistlinger [46]. Fundamental theories contributed to the first metal-oxide gas sensor in 1954 that was presented by Heiland Bielanski et al. [47]. In 1971, the Taguchi-type SnO_2 sensor (TGS), which is thick film resistive based gas sensors, was patented in the U.S. and commercialized by Figaro Engineering Inc. [48]. Current commercially available metal-oxide gas sensors are mostly using thick film technology. Thin film technology was not commonly used for high temperature applications due to the higher instability of the chemical and physical properties of the metal-oxide thin films at the elevated temperatures compared to thick films or bulk material [49]. Table 1-1 summarizes selected metal-oxide materials for gas sensing applications including their operating temperature range and response time.

Table 1-1: Summary of selected metal-oxide materials reported for gas-sensing applications

Material	Target gas	Operating Temperature (°C)	Response Time (τ_{60})	Reference
Al_2O_3	H_2	450	< 1min	[50]
	CO_2			
	O_2			
	Humdity	-60 – 40	N.A.	[51]
Bi_2O_3	H_2	450	< 1 min	[50]
	CO_2			
	O_2			
	CO	200 – 350	80 – 90 s	[52]
CdO	H_2	450	< 1min	[50]
	CO_2			
	O_2			
	Acetone	300	3 s	[53]
CeO	H_2	500	< 1 min	[50]
	O_2	700 to 1100	5 – 10 ms	[54]
	CO_2	550 – 600	N.A.	[55]
	H_2S	7 – 127	20 – 40 s	[56]
Cr_2O_3	H_2	450	< 1 min	[50]
	CO_2			
	O_2			
	NO_2	350 – 400	1 – 3 min	[57]
	NH_3	200 – 500	2 – 5 min	[58]
Fe_2O_3	H_2	450	< 1 min	[50]
	CO_2			
	O_2			
	CO	525 – 1075	N. A.	[59]
	CH_4			
	NO_2	150 – 400	2 – 5 min	[60]
	Humidity	25	< 150 s	[61]
Ga_2O_3	O_2	480 – 820	N. A.	[62]
	CH_4	500 - 1000	30 ms	[63]
	CO			
	NO	600 – 1000	< 1 min	[64]
	NH_3			

Table 1-1 (Cont.)

Material	Target gas	Operating Temperature (°C)	Response Time (τ_{60})	Reference
In_2O_3	O_3	40 – 500	30 min – 2 hr	[65]
	H_2	350	5 – 90 s	[66]
	CO			
	C_3H_8			
	NO_2	250	5 min	[67]
	NH_3	300 – 640	2 min	[68]
	NO_x	129	4 – 20 min	[69]
MnO_2	H_2O	25	2 – 5 min	[70]
NiO_x	H_2	30	N.A.	[71]
	NH_3			
	NO_2			
	SO_2			
	CO			
SnO_2	CO	200 – 500	< 1 min	[72]
	CO_2	450	< 1 min	[73]
	H_2S	300 – 450	< 1 min	[74]
	NO_2			
	SO_2	200 – 500	10 – 20 min	[75]
	O_2	27 – 650	N.A.	[76]
	H_2			
	Humidity			
	CH_4	320	< 1 min	[77]
	NH_3	450 – 500	3 min	[78]
	NO_x	150 – 300	N. A.	[79]
TiO_2	H_2	450	< 1 min	[50]
	CO_2			
	O_2			
	CH_4	700 – 1000	N. A.	[59]
WO_3	H_2S	300 – 800	N. A.	[80]
	NO	100 – 250	2 min	[81]
	NO_2	200 – 450	5 min	[82]
	NO_x	25 – 350	3 – 5 min	[83]
ZnO	CO	300 – 500	2 min	[84]
	CH_4			
	H_2			
	Humidity	20	< 1 min	[85]
	NO	775	N.A.	[86, 87]
	NO_2			

Two models typically used to explain these metal oxide sensor response are the Charge-Transfer-Model (CTM) and defect chemistry theory. For the CTM, oxygen ions are formed through the transfer of electrons from the conduction band (CB) and are electrostatically stabilized in the vicinity of the surface. For example, oxygen adsorbs on SnO_2 as a molecule (O^{2-}_{ads}) and atomic ions (O^{2-}_{ads}, O^{-}_{ads}) that trap electrons from the conduction band.

Reducing gases (e.g., CO) react with the oxygen ions and release electrons, which return to the conduction band. In an oxygen-free atmosphere, CO could also act like an ion (CO^{+}) and adsorb on the material surface, inserting an electron into the conduction band. Thus, the electrical conductivity is changed.

The defect chemistry theory holds that CO removes oxygen from the surface of the lattice to yield CO_2, and creates an oxygen vacancy. When there is no oxygen, the vacancy becomes ionized and the electrons are introduced into the conduction band, which causes the conductivity to increase. If oxygen is present, oxygen fills the oxygen vacancy, for which one or more electrons are taken from the conduction band. Therefore, the conductivity decreases. Both models cannot give a complete picture of the mechanism since this process typically studies only the effect of a single gas rather than that of gas mixtures (e.g., N_2, H_2O, CO_2, etc.) as found in combustion applications.

Most metal-oxide based gas sensors operate in a temperature range around 450 – 500°C that is too low for many combustion processes, unless the exhaust gases are measured further downstream. Some metal oxides with higher melting temperature and lower vapor pressure at high temperatures could allow higher temperature gas

measurements, such as CeO, TiO_2, Ga_2O_3 and WO_3. Most metal oxides are however based on surface adsorption effects and not sufficiently selective towards a particular gas.

1.2.2 Perovskite oxide based gas sensors

Perovskite oxides based gas sensors are based on bulk effects (absorption into the lattice) and can tolerate high temperatures (T > 500°C) and thermal cycling [1-2, 34-35]. Electrons, holes, or ions contribute to the electrical conductivity in these materials. The dominant conduction mechanism in perovskite materials depends on doping, temperature, and the oxygen partial pressure. Perovskite oxides based gas sensors have been investigated in the research domain and tested under industrial conditions. Doped $SrTiO_3$ has been tested in lean-burning engines as oxygen sensor [88]. Yttrium-stabilized Zirconia (YSZ) is commercially used in automotive oxygen (Lambda-) sensors. Research on perovskite materials focuses on bulk or thick film devices, not on thin films. Table 1-2 lists selected perovskite materials used in gas sensing.

$SrTiO_3$ is one of the most commonly used and the earliest material studied for high temperature oxygen sensors. The strontium and oxygen vacancies act as intrinsic ionic point defects. At low oxygen partial pressures, the predominant charge carriers are oxygen vacancies and electrons (according to Kroeger-Vink notation [96-100]),

$$O_o^x = \tfrac{1}{2}\, O_2 + 2e' + V_o^{\bullet\bullet}. \qquad (1.1)$$

At high oxygen partial pressures, the predominant charge carriers are strontium vacancies and holes [96-100],

$$\tfrac{1}{2}\, O_2 + Sr_{sr}^x = V_{sr}'' + 2h^{\bullet} + SrO. \qquad (1.2)$$

Table 1-2: Summary of selected perovskite materials used in gas-sensing applications

Material	Target gas	Operating Temperature (°C)	Response Time (τ_{60})	Reference
$SmFeO_3$	CO	200 – 400	3 min	[89]
Fe doped $LaGaO_3$	O_2	800	N.A.	[90]
LSGF/LSFC	CH_4	1025	N.A.	[90]
La doped $CaTiO_3$	O_2	1050	N.A.	[91]
In doped $BaZrO_3$	Humidity	300	N.A.	[92]
Y doped $BaZrO_3$	Humidity	400 – 700	120 s	[1]
La doped $BaTiO_3$	CO	400	6 min	[93]
$LaFeO_3$	NO_x	400 – 900	4 min	[94]
$BaSnO_3$	O_2 CO NO_2	400 – 700 400 – 600 400 – 600	N.A	[95]
$SrTiO_3$	O_2	400 – 700	N.A.	[96-100]
$GdCo_{1-x}Cu_xO_3$	O_2 CO_2	300 – 400	N.A.	[101]

In oxygen atmosphere, oxygen ions diffuse into the lattice and fill the vacancies. This absorption process causes a change in electrical conductivity [102]. The conductivity of both doped and undoped $SrTiO_3$ contains *n*-type and *p*-type regimes depending on oxygen partial pressure, stoichiometry of the film, and doping concentrations.

Perovskite oxides based gas sensors can be used in a variety of resistance-based gas sensors, particular for high temperature applications. The electrical conductivity and sensing mechanisms not only provide for a comparably high conductivity, but also a sufficiently high selectivity allowing distinguishing of individual species in mixed gas environments [102].

1.2.3 Humidity sensors

Humidity plays a major role in industrial and combustion processes. Humidity (water vapor) is difficult to measure in those processes since it is associated with other parameters, such as temperature and pressure [103]. Humidity is usually measured and denoted as either relative humidity (RH %), partial pressure of water (atm/Pa), dew/frost point (D/F PT), or parts per million (PPM) water. Absolute humidity or the dew point is used for monitoring in some medical devices and air conditioning. Relative humidity has to be controlled in many industrial processes [104]. Current commercially available humidity sensors with temperature range between -40°C and 200°C can measure relative humidity from 2% to 90% (Fig. 1-1). Their response time varies from 30 seconds to 5 minutes [105-106]. The cost for each humidity sensor ranges from $39 to $1,500 depending on its application, accuracy, size, and long-term stability.

The materials used in most humidity sensors can be classified into three groups: electrolytes, organic polymers, and ceramics [107]. Table 1-3 gives an overview of some humidity sensors based on those materials, their operating temperature, and response time.

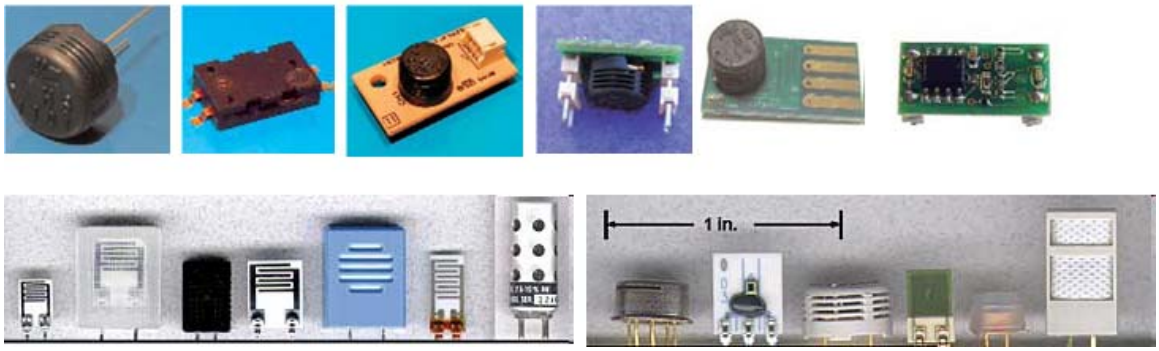

Fig. 1-1: Examples of current market available humidity sensors with temperature range from -40°C to 200°C are used in air conditioners, weather stations, printers, humidifiers, and medical devices. Relative humidity measurement ranges between 2% and 90% [106].

Table 1-3: Example humidity sensors with their operating temperature and response time

Material	Operating Temperature (°C)	Response Time (τ_{60})	References
$MgAl_2O_4$	40	150 s	[108]
LiCl	25	30 min	[109]
TiO_2	25	N.A.	[110]
NASICON	0 – 60	90 s	[111]
ZrO_2-MgO	400 – 700	N.A.	[112]
YSZ	300-450	< 1 min	[113]
Zerolite based materials	125	2 min	[114-118]
$SrCe_{0.95}Yb_{0.05}O_3$	600 – 1000	1 min	[119]
ZnO-CuO	30	20 s	[120]

Humidity sensors must meet the following requirements: 1) a good sensitivity over a wide range of humidity and temperature, 2) fast response time, 3) good reproducibility and small hysteresis, 4) long-term stability, 5) resistance against contaminants, and 6) low cost.

Commercially available humidity sensors are used in a variety of applications ranging from process control, biomedical devices, home appliances, to air quality control. These devices usually work at temperature between 0°C and 85°C, with some device allowing up to 125°C with comparably response time of τ_{60} that is defined as the time required for the conductivity of the sensor element to reach 60% of the equilibrium value have demonstrated humidity sensitivity at high temperatures (300°C to 1000°C) and response times of τ_{60} from 60 to 360 seconds (Fig. 1-2).

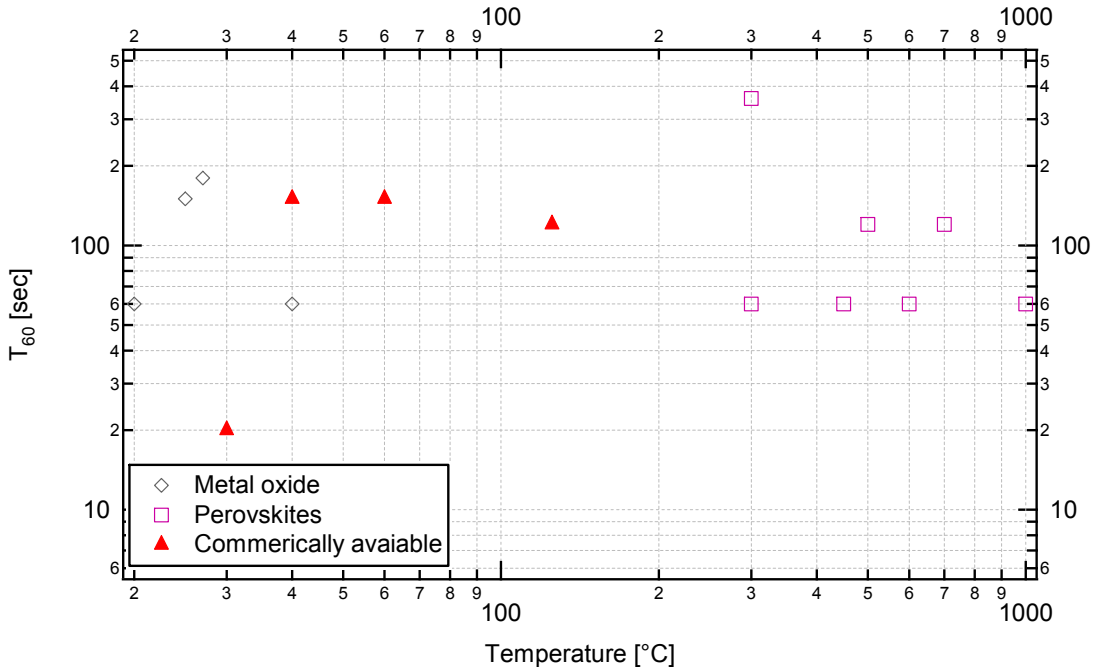

Fig. 1-2: Temperature vs. sensor response time of τ_{60} for some metal oxide, perovskite oxide, and commercial available humidity sensors based on Table 1-1, 1-2 and 1-3. (τ_{60} = 20 to 180 s). Some metal oxide and perovskite materials presented in literature.

1.3 Research objectives for Y-doped $BaZrO_3$ thin films for high temperature humidity sensors

The broader objectives of this project were to develop and investigate Y-doped $BaZrO_3$ thin films and their feasibility in humidity micro sensors at high operating temperatures (> 500°C) with fast response. Particular objectives included: 1) establish Y-doped $BaZrO_3$ thin films process window for physical vapor deposition (PVD) techniques, 2) characterize and study the material properties to gain a better understanding of the sensing mechanism, 3) develop testing conditions of Y-doped $BaZrO_3$ humidity sensors at high temperatures and broad humidity range, 4) characterize operating temperature ranges, response time, sensitivity, repeatability, and long-term stability of the humidity sensors for high temperature applications, and 5) evaluate Y-

doped $BaZrO_3$ thin films as a high temperature humidity sensors in a mixed gas species environment for its selectivity.

We have demonstrated the feasibility of fast, highly selective, and stable humidity sensors based on Y-$BaZrO_3$ thin films. We identified Ba deficiencies in all deposited layers and defined suitable process windows for sputtering and PLD deposition of films with closer stoichiometric compositions with good sensitive response. We were able to demonstrate the impact of Cr with Au and Ti with Pt as contact material on the sensor response leading to the recommendation of Cr with Au as reliable contact, thereby limiting the operating temperature to below 1000°C. We were able to demonstrate sensors with higher sensitivity and selectivity towards humidity and 4-20 times faster response than reported elsewhere in literature. In addition, we tested selectivity towards humidity in a typical mixture of combustion gases to simulate the real world environment. Finally, we have presented long term stability and sensor lifetime data in excess of one year.

1.4 Organization and structure of dissertation

Chapter 2 introduces the technical background on material properties, defect chemistry, proton incorporation and transfer mechanism, oxygen conduction, the interfaces between metal contact and Y-doped $BaZrO_3$ materials, and thin film deposition techniques.

In Chapter 3, selected results using sputter deposited Y-doped $BaZrO_3$ thin film as high temperature (up to 400°C) humidity sensors are presented. The experimental investigations include characterizing film composition, microstructure, surface morphology, annealing parameters, device fabrication, electrical conductivity as a

function of temperature, gas sensitivity, and cross-sensitivity with mixed gaseous.

Chapter 4 discusses alternative solutions to solve the difficulties in control of film stoichiometry and thermal stress during sputter deposition and annealing, by using pulsed laser deposition (PLD). To evaluate the suitability of PLD as deposition method for Y-doped $BaZrO_3$ thin films in high temperature ($T \geq 500°C$) humidity sensors, all films are characterized as done with sputtered films.

A comparative study of Y-doped $BaZrO_3$ thin films as high temperature humidity sensors deposited by sputtering and PLD methods is presented in Chapter 5. The effects of experimental deposition parameters and annealing conditions may cause different chemical composition, morphology structure, and sensors response. Experimental data are presented and discussed to find the process window for Y-doped $BaZrO_3$ thin films for use in high temperature humidity sensors. The causes of some technical challenges are discussed.

Chapter 6 is a study of the correlation between film thickness, sensitivity and response time for fast high temperature humidity sensors based on PLD Y-doped $BaZrO_3$thin films with thicknesses down to 30 nm. Both surface ion exchange and bulk diffusion contribute to electrical conduction according to current understanding of the defect chemistry of the material. Decreasing film thickness increases the impact of surface effects and leads to strong improvements of sensitivity and response time, allowing the combination of the higher PLD stability with the faster and more sensitive response of sputtered films.

Chapter 7 gives a concise overview of the work done, key accomplishments and initial interpretation of the data presented in this work, including the material

characterization, device development, and sensor response. Future work and improvements of the sensor performance are identified focusing on key challenges identified in Chapters 3, 4, 5, and 6. Limiting factors such as stoichiometry of films and sensor contact materials will be reviewed and discussed.

1.5 References

[1] W. Wang, A.V. Virkar, Ionic and electron-hole conduction in $BaZr_{0.93}Y_{0.07}O_{3-\delta}$ by 4-probe dc measurements, J. Power Source 142 (2005) 1-9.

[2] W. Wang, A.V. Virkar, A conductimetric humidity sensor based on proton conducting perovskite oxides, J. Sens. Actuators, B Chem. 98 (2004) 282-290.

[3] N. Yamazoe, Y. Shimizu, Humidity sensors: principles and applications, Sens. Actuators, B Chem. 10 (1986) 379-398.

[4] C. D. Zuo, Doping and defects structure for mix-conducting ceramics for gas separation, Ph.D. dissertation (2006).

[5] J. Wu, Defect chemistry and proton conductivity for Ba-based pervoskites, Ph.D dissertation (2005).

[6] A.S. Nowick, Y. Du, High-temperature protonic conductors with perovskite-related structures, Solid State Ionics, vol. 77 (1995) 137.

[7] Solomon, S., D. Qin, M. Manning, Z. Chen, M. Marquis, K.B. Averyt, M.Tignor, H.L. Miller (eds.), IPCC, 2007: Summary for Policymakers. In: Climate Change 2007: The Physical Science Basis. Contribution of Working Group I to the Fourth Assessment Report of the Intergovernmental Panel on Climate Change, Cambridge University Press, Cambridge, United Kingdom and New York, NY, USA.

[8] http://en.wikipedia.org/wiki/Fossil_fuel_power_plant.

[9] http://en.wikipedia.org/wiki/Clean_coal_technology

[10] http://www.airquality.utah.gov/Air-Quality-Board/index.htm

[11] E. Andrews, Advanced sensors, Presentation, Cummins Engines Co Inc., University of Utah (2007).

[12] R.K. Hanson, D.S. Baer, Multiplexed diode-laser gas sensor system for in-situ multispecies emissions measurements, Final report of National Center for Environmental Research (1995).

[13] B.M. Kulwicki, Humidity sensors, J. Am. Ceram. Soc. 74 (1991) 697-708.

[14] E. Traversa, Ceramic sensors for humidity detection : the state-of-the art and future development, Sens. Actuators, B Chem. 23 (1995) 135-136.

[15] P. Shuk, M. Greenblatt, Solid-state electrolyte film humidity sensor, Solid State Ionics, vol. 113-115 (1998) 229-233.

[16] X. Shi, Q. Chen, J. Fang, K. Varahramyan, H. Ji, Al_2O_3-coated microcantilevers for detection of moisture at ppm level, Sens. Actuators, B Chem. 129 (2008) 241-225.

[17] G. Di Francia, A. Castaldo, E. Masserra, I. Nasti, L. Quercia, I. Rea, A very sensitive porous silicon based humidity sensor, Sens. Actuators, B Chem. 111-112 (2005) 135-139.

[18] K. Arshaka, K. Twomey, D. Egan, A ceramic thick film humidity sensor based on MnZn ferrite, Sensors 2 (2002) 50-61.

[19] Y. Sakai, Y. Sadaoka, M. Matsuguchi, Humidity sensors based on polymer thin films, Sens. Actuators, B Chem. 35-36 (1996) 85-90.

[20] J. W. Fergus, Perovskite oxides for semiconductor-based gase sensors, Sens. Actuators, B Chem. 123 (2007) 1169-1179.

[21] H. Iwahara, T. Esaka, H. Uchida, N. Maeda, Proton conduction in sintered oxides and its applicaiton to steam electrolysis for hydrogen prodution, Solid State Ionics, vol. 3-4 (1981) 359-363.

[22] T. Norby, Solid-state protonic conductors: principles, properties, progress and prospects, Solid State Ionics, vol. 125 (1999) 1-11.

[23] H. Iwahara, T. Yajima, T. Hibino, K. Ozaki, H. Suzuki, Protonic conduction in calcium, strontium and barium zirconates, Soild State Ionics, vol. 62 (1993) 225.

[24] A. Manthiram, J. F. Kuo, J. B. Goodenough, Characterization of oxygen-deficient perovskites as oxide-ion electrolytes, Solid State Ionics, vol. 62 (1993) 225.

[25] R.C.T. Slade, S.D. Flint, N. Singh, Investigation of protonic conduction in Yb-and Y-doped barium zirconates, Solid State Ionics, vol. 82 (1995) 135.

[26] K.D. Kreuer, Aspects of the formation and mobility of protonic charge carriers and the stability of perovskite-type oxides, Solid State Ionics, vol. 125 (1999) 285-302.

[27] H.G. Bohn, T. Schober, Electrical conductivity of the high temperature proton conductor $BaZr_{0.9}Y_{0.1}O_{2.95}$, J. Am. Ceram. Soc., 83 (2000) 768.

[28] K.D. Kreuer, Proton conducting oxides, Ann. Rev. Mater. Res. 33 (2003) 333-359.

[29] C.D. Savaniu,J. Canales-Vazquez, J.T.S. Irvine, Investigation of proton conducting $BaZr_{0.9}Y_{0.1}O_{2.95}$: $BaCe_{0.9}Y_{0.1}O_{2.95}$ core shell structure, J. Mater. Chem. 15 (2005) 598.

[30] K. Katahira, Y. Kohchi, T. Shimura, H. Iwahara, Protonic conduction in Zr-substituted $BaCeO_3$, Soild State Ionics, vol. 138 (2000) 91.

[31] V.P. Gorelov, V.B. Balakireva, Y.N. Kleshchev, V.P. Brusentsov, Preparation and electrical conductivity of $BaZr_{1-x}R_xO_{3-\delta}$ (R = Sc, Y, Ho, Dy, Gd, In), Inorg. Mater. 37 (2001) 535.

[32] M. Laidoudi, I.A. Talib, R. Omar, Investigation of the bulk conductivity of $BaZr_{0.95}M_{0.05}O_3$ (M= Al, Er, Ho, Tm, Yb, and Y) under wet N_2, J. Phys. D Appl. Phys. 35 (2002) 397.

[33] F.M.M. Snijkers, A. Buekenhoudt, J. Cooymans, J.J. Luyten, Proton conductivity and phase composition in $BaZr_{0.9}Y_{0.1}O_{3\text{-delta}}$, Scripta Mater. 50 (2004) 655.

[34] D.C. Li, W. Liu, Y.X. Zhang, P.H. Yang, C.S. Chen, Fabrication, microstructure, mechanical and transporting properties of $BaZrO_3$-particles-dispersed $YBa_2Cu_3O_{7-\delta}$ mixed conduction composites, Solid State Comm. 131 (2004) 235-239.

[35] F. Iguchi, T. Yamada, N. Sata, T. Tsurui, H. Yugami, The influence of grain structures on the electrical conducitivity of a $BaZr_{0.95}Y_{0.05}O_3$ proton conductor, Solid State Ionics, vol.177 (2006) 2281.

[36] H. Norton, Transducer fundamentals, in: Handbook of Transducers, Englewood Cliffs, NJ: Prentice Hall (1989).

[37] F. Solzbacher, Lecture notes: Sensors and Actuators, Chapter 1 (2006).

[38] T. Wolkenstein, Electronic processes on the surface of semiconductors during chemisorption, Consult. Bureau, New York (1987).

[39] W. H. Brattain, J. Bardeen, Surface properties of germanium, Bell syst. Tech. J. 32 (1953) 1.

[40] H.J. Engell, K.H. Hauffe, Surface potential, field-effect mobility, and surface conductivity of ZnO crystals, Phys. Rev. 114 (1959) 655.

[41] O. Jaentsch, Slow surface states and chemisorption, J. Phys. Chem. Solids, 26 (1965) 1233.

[42] K. Hauffe in Semiconductor surface physics (Ed.: R.H. Kingston), University of Pennsylvania Press, Philadelphia, (1956) 259.

[43] W. Schottky, Vereinfachte und erweiterte Theorie der Randschicht-gleichrichter, Zeitschrift für Physik A Hadrons and Nuclei, 1941.

[44] T. Volkenstein, Elektronentheorie der Katalyse an halbleitern, VEB, Berlin (1964).

[45] T. Volkenstein, The Electron Theory of Catalysis on Semiconductors, Adv. Catal. 12 (1960) 189.

[46] H. Geistlinger, Interface and surface statics for a Schottky-barrier gas sensors, Sens. Actuators, B Chem., vol. 7 issues 1-3 (1992) 615-629.

[47] G. Heiland, Zum Einfluss von Wasserstoff auf die elektrische Leitfähigkeit von ZnO-Kristallen.Z.Physik. 138 (1954) 459-464.

[48] A. Chiba, Chemical Sensor Technology, vol. 4 (Ed.: S. Yamauchi), Elsevier, Amsterdam, (1992) 1.

[49] G. Eranna, B. C. Joshi, D. P. Runthala, R. P. Gupta, Oxide materials for development of integrated gas sensors – A comprehensive review, C. R. in Solid State and Materials Sci. 29 (2004) 111-188.

[50] T. Seiyama, S. Kagawa, Study on a detector for gaseous components using semiconductive thin films, Analytical Chemistry 38 (1966) 1069–1073.

[51] G. Sberveglieri, R. Anchisini, R. Murri, C. Ercoli, N. Pinto, An Al_2O_3 sensor for low humidity content: characterization by impedance spectroscopy, Sens. Actuators, B Chem. 32 (1996) 1-5.

[52] G.S. Devi, S. V. Manorama, V. J. Rao, SnO_2/Bi_2O_3: A suitable system for selective carbon monoxide detection, J. Electrochem. Soc. 145 (1998) 1039–1044.

[53] S.V. Ryabtsev, A. V. Shaposhnick, A. N. Lukin, E. P. Domashevskaya, Application of semiconductor gas sensors for medical diagnostics, Sens. Actuators, B Chem. 59 (1999) 26-29.

[54] H.J. Beie, A. Gn'orich, Oxygen gas sensors based on CeO_2 thick and thin films, Sens. Actuators, B Chem. 4 (1991) 393–399.

[55] S. Matsubara, S. Kaneko, S. Morimoto, S. Shimizu, T. Ishihara, Y. Takita, A practical capacitive type CO_2 sensor using $CeO_2/BaCO_3/CuO$ ceramics, Sens. Actuators, B Chem. 65 (2000) 128– 132.

[56] G. Fang, Z. Liu, C. Liu, K. Yao, Room temperature H_2S sensing properties and mechanism of CeO_2-SnO_2 sol-gel thin films, Sens. Actuators, B Chem. 66 (2000) 46–48.

[57] Y. Li, W. Wlodarski, K. Galatsis, S. H. Moslih, J. Cole, S. Russo, and N. Rockelmann, Gas sensing properties of p-type semiconducting Cr-doped TiO_2 thin films, Sens. Actuators, B Chem. 83 (2002) 160–163.

[58] P.T. Moseley, D. E.Williams, A selective ammonia sensor, Sens. Actuators, B Chem. 1 (1990) 113–115.

[59] R.M. Geatches, A.V. Chadwick, J. D. Wright, Single crystal metal oxide gas sensors, Sens. Actuators, B Chem. 4 (1991) 467–472.

[60] G. Neri, A. Bonavita, S. Galvagno, P. Siciliano, S. Capone, CO and NO_2 sensing properties of doped-Fe_2O_3 thin films prepared by LPD, Sens. Actuators, B Chem. 82 (2002)40–47.

[61] G. Neri, A. Bonavita, C. Milone, A. Pistone, S. Galvagno, Gold promoted Li-Fe_2O_3 thin films for humidity sensors, Sens. Actuators, B Chem. 92 (2003) 326–330.

[62] V. K. Josepovits, O. Krafcsik, G. Kiss, I. V. Perczel, Effect of gas adsorption on the surface structure of β-Ga_2O_3 studied by XPS and conductivity measurements, Sens. Actuators, B Chem. 48 (1998) 373–375.

[63] M. Fleischer, H. Meixner, Fast gas sensors based on metal oxides which are stable at high temperatures, Sens. Actuators, B Chem. 43 (1997) 1–10.

[64] M. Fleischer, M. Seth, C.-D. Kohl, H. Meixner, A study of surface modification at semiconducting Ga_2O_3 thin film sensors for enhancement of the sensitivity and selectivity, Sens. Actuators, B Chem. 35-36 (1996) 290–296.

[65] T. Doll, A. Fuchs, I. Eisele, G. Faglia, S. Groppelli, G. Sberveglieri, Conductivity and work function ozone sensors based on indium oxide, Sens. Actuators, B Chem. 49 (1998) 63–67.

[66] W.Y. Chung, G. Sakai, K. Shimanoe, N. Miura, D.-D. Lee, N. Yamazoe, Preparation of indium oxide thin film by spin-coating method and its gas-sensing properties, Sens. Actuators, B Chem. 46 (1998) 139–145.

[67] C. Cantalini, W. Wlodarski, H. T. Sun, M. Z. Atashbar, M. Passacantando, S. Santucci, NO_2 response of In_2O_3 thin film gas sensors prepared by sol-gel and vacuum thermal evaporation techniques, Sens. Actuators, B Chem. 65 (2000) 101–104.

[68] H. Yamaura, T. Jinkawa, J. Tamaki, K. Moriya, N. Miura, N. Yamazoe, Indium oxide-based gas sensor for selective detection of CO, Sens. Actuators, B Chem. 35-36 (1996) 325–332.

[69] T. Ishihara, S. Sato, T. Fukushima, Y. Takita, Capacitive gas sensor of mixed oxide CoO-In_2O_3 to selectively detect nitrogen monoxide, J. Electrochem. Soc. 143(1996) 1908–1914.

[70] C.N. Xu, K. Miyazaki, T. Watanabe, Humidity sensors using manganese oxides, Sens. Actuators , B Chem. 46 (1998) 87–96.

[71] A. Neubecker, T. Pompl, T. Doll, W. Hansch, I. Eisele, Ozone-enhanced molecular beam deposition of nickel oxide (NiO) for sensor applications, Thin Solid Films 310 (1997) 19–23.

[72] H. Windischmann, P. Mark, A model for the operation of a thin-film SnO_x conductance-modulation carbon monoxide Sensor, J. Electrochem. Soc. 126 (1979) 627–633.

[73] T. Seiyama, S. Kagawa, Study on a detector for gaseous components using semiconductive thin films, Analytical Chemistry 38 (1966) 1069–1073.

[74] C. D. Natale, F. Davide, G. Faglia, P. Nelli, Study of the effect of the sensor operating temperature on SnO_2-based sensor-array performance, Sens. Actuators, B Chem. 23 (1995) 187– 191.

[75] D. Girardin, F. Berger, A. Chambaudet, R. Planade, Modelling of SO_2 detection by tin dioxide gas sensors, Sens. Actuators, B Chem. 43 (1997) 147–153.

[76] N. Yamazoe, J. Fuchigami, M. Kishikawa, T. Seiyama, Interactions of tin oxide surface with O_2, H_2O and H_2, Surface Science 86 (1979) 335–344.

[77] G. S. V. Coles, G.Williams, B. Smith, The effect of oxygen partial pressure on the response of tin (IV) oxide based gas sensors, J. Phys. D: Appl. Phys. 24 (1991) 633–641.

[78] L. Chambon, J. P. Germain, A. Pauly, V. Demarne, A. Grisel, A metallic oxide gas sensor array for a selective detection of the CO and NH_3 gases, Sens. Actuators, B Chem. 60 (1999) 138–147.

[79] N. Y. Shishkin, I. M. Zharsky, V. G. Lugin, V. G. Zarapin, Air sensitive tin dioxide thin films by magnetron sputtering and thermal oxidation technique, Sens. Actuators, B Chem. 48(1998) 403–408.

[80] E. P. S. Barrett, G. C. Georgiades, P. A. Sermon, The mechanism of operation of WO_3-based H_2S sensors, Sens. Actuators, B Chem. 1(1990) 116–120.

[81] M. Penza, L. Vasanelli, SAW NOx gas sensor using WO_3 thin-film sensitive coating, Sens. Actuators, B Chem. 41(1997) 31–36.

[82] C. Cantalini, M. Pelino, H. T. Sun, M. Faccio, S. Santucci, L. Lozzi, M. Passacantando, Cross sensitivity and stability of NO_2 sensors fromWO_3 thin film, Sens. Actuators, B Chem. 35- 36 (1996) 112–118.

[83] A. A.Tomchenko,V.V. Khatko, I. L. Emelianov,WO_3 thick-film gas sensors, Sens. Actuators, B Chem. 46 (1998) 8–14.

[84] B. Bott, T. A. Jones, B. Mann, The detection and measurement of CO using ZnO single crystals, Sens. Actuators 5 (1984) 65–73.

[85] Y. Toyoshima, M. Miyayama, H. Yanagida, K. Koumoto, Effect of relative humidity on current-voltage characteristics of Li-doped CuO/ZnO junction, Jpn. J. Appl. Phys. 22 (1983) 1933.

[86] C. N. R. Rao, A. R. Raju, K. Vijayamohanan, Gas-sensor materials, in New Materials (S. K. Joshi, T. Tsuruta, C. N. R. Rao, S. Nagakura, Eds., Narosa, New Delhi, 1992, and the references therein).

[87] P. Romppainen, V. Lantto, S. Lepp¨avuori, Effect of water vapour on the CO response behaviour of tin dioxide sensors in constant temperature and temperature-pulsed modes of operation, Sens. Actuators, B Chem. 1 (1990) 73–78.

[88] R. Moos, F. Rettig, A. Huerland, C. Plog, Temperature-independent resistive oxygen exhaust gas sensor for lean-burn engines in thick film technology, Sens. Actuators, B Chem. 93 (2003) 43-50.

[89] M.C. Carotta, G. Matinelli, Y. Sadaoka, P. Nunziante, E. Traversa, Gas sensitive electrical properties of perovskite-type $SmFeO_3$ thick films, Sens. Actuators, B Chem. 48 (1998) 270-276.

[90] T. Ishihara, T. Yamada, H. Aikawa, H. Nishiguchi, Y. Takita, Mixed electronic oxide ionic conductivity and oxygen permeating property of Fe-, Co-, or Ni-doped $LaGaO_3$ perovskite oxide, Solid State Ionics, vol.135 (2000) 631-636.

[91] T. Bak, J. Nowotny, C.C. Sorrell, M. F. Zhou, E. R. Vance, Charge transport in $CaTiO_3$: I. electrical conductivity, J. Material Sci.: Materials in Electronics, vol. 15 (2004).

[92] I. Ahmed, S. G. Eriksson, E. Ahlberg, C.S. Knee, M. Karlsson, A. Matic, D. Engberg L. Boerjesson, Proton conductivity and low temperature of In-doped $BaZrO_3$, Solid State Ionics, vol. 177 (2006) 2357-2362.

[93] Z.G. Zhou, Z.L. Tang, Z.T. Zhang, W. Wlodarski, Perovskite oxide of PTCR ceramics as chemical sensors, Sens. Actuators, B Chem. 77 (2001) 22-26.

[94] M.L. Grilli, E.D. Bartolomeo, E. Traversa, Electrochemical No_x sensors based on interfacing nanosized $LaFeO_3$ perovskite-type oxide and ionic conductors, J. Electrochemical Society 148 (2001) H98 – H102.

[95] J. Cerda, J. Arbiol, G. Dezanneau, R. Diaz, J.R. Morante, Perovskite-type $BaSnO_3$ powders for high temperature gas sensor application, Sens. Actuator, B Chem. 84 (2002) 21-25.

[96] R. Meyer, R. Waser, Resistive donor-doped $SrTiO_3$ sensors, I. Basic model for a fast sensor response, Sens. Actuators B Chem. 101 (2004) 335-345.

[97] J. Gerblinger, H. Meixner, $SrTiO_3$ thin films for oxygen sensors, in: O. Auciello, R. Waser (Eds.) Science and Technology of Electrocramic thin films, Kluwer Acad. Publ., Dordrecht, The Nertherlands (1995) 439-453.

[98] N.H. Chan, R.K. Sharma, D.M.Smyth, Nonstoichiometry in $SrTiO_3$, J. Electrochem. Soc. 128 (1981) 1762-1769.

[99] Y. Yoo, S. Koutcheiko, A. Petric, Strontium titanate doped with lanthanides for SOFC anode materials, in: J. Huijsmans (Ed.), Fifth European Solid Oxide Fuel Cell Forum, European Fuel Cell Forum, Oberrohrdorf, Switzerland (2002) 507-514.

[100] W. Menesklou, H.J. Schreiner, K.H. Haerdtl, E. Ivers-Tiffee, High temperature oxygen sensors based on doped $SrTiO_3$, Sens. Actuators B Chem. 59 (1999) 184-189.

[101] C.R. Michel, E.R. Lopez, A. Chavez, Sensing behavior of perovskites $GdCo_{1-x}Cu_xO_3$ prepared by solution and ultrasonic-assisted aerosol methods, Mater. Res. Soc. Symp. Proc. 828 (2005) 211-216.

[102] J.W. Fergus, Perovskite oxides for semiconductor-based gas sensors, Sens. Actuators, B Chem. 123 (2007) 1169-1179.

[103] http:// www.iceweb.com.au/Analyzer/humidity_sensors.html.

[104] E. Traversa, Ceramic sensors for humidity detection: the state-of-the-art and future developments, Sens. Actuators, B Chem. 23 (1995) 135-156.

[105] http://www.humirel.com/tech/doc/ProductSelectorGuide.pdf.

[106] http://www.sensorsmag.com/sensors.

[107] N. Yamazoe, Y. Shimizu, Humidity sensors: principles and applications, Sens. Actuators, B Chem. 10 (1986) 379-398.

[108] G. Gusmano, G. Montesperelli, P. Nunziante, E. Traversa, Microstructure and electrical properties of $MgAl_2O_4$ and $MgFe_2O_4$ spinel porous compacts for use in humidity sensors, Br. Ceram. Trans. 92 (1993) 104-108.

[109] F.W Dunmore, An electrometer and its application to radio meteorography, J. Res. Nat. Bur. Std., 20 (1938) 724-744.

[110] H. Yagi, M. Nakata, Humidity sensor using Al_2O_3, TiO_2 and SnO_2 prepared by sol-gel method, J. Ceram. Soc. Jpn., Int. Ed., 95 (1987) 683-687.

[111] H. Yagi, T. Saiki, Humidity sensor using NASICON not containing phosphorus, Sens. Actuators, B Chem. 5 (1991) 135-138.

[112] T. Nitta, F. Fukushima, Y. Matsuo, Water vapor gas sensor using ZrO2-MgO ceramic body, in T. Seiyama, K. Fueki, J. Shiokawa and S, Suzuki (Eds.), Analytical Chemistry Symp. Series; Chemical Sensors 17 (1983) 387-392.

[113] H. Yagi, K. Horii, Humidity sensing characteristics of a limiting current type plane oxygen sensor in high temperature environment, Denki Kagaku 60 (1992) 220-225.

[114] J. Zou, H.Y. He, J.P Dong, Y.C. Long, A guest/host material of LiCl/H-STI (stilbite) zeolite assembly: preparation, characterization and humidity-sensitive properties. J. Mater. Chem. 14 (2004) 2405-2411.

[115] J. Zou, H.Y. He, J.P. Dong, Y.C Long, A novel LiCl/H-STI zeolite guest/host assembly material with superior humidity sensitivity: fabrication and characterization. Chem. Lett. 8 (2001) 810-811.

[116] J. Zou, H.Y. He, J.P. Dong, Y.C Long, Y.C. Studies on CXN natural zeolite IV. Research on the humidity-sensitive property of the novel LiCl/H STI guest/host material. Acta Chim. Sin. 59 (2001) 862-866.

[117] N. Li, X.T. Li, T. Zhang, S.L. Qiu, G.S. Zhu, W.T. Zheng, W.X. Yu, Host-guest composite materials of LiCl/NaY with wide range of humidity sensitivity. Mater. Lett. 58 (2004) 1535-1539.

[118] X.T. Li, C.L. Shao, H. Ding, T. Zhang, N. Li, S.L. Qiu, F.S. Xiao, Preparation and humidity sensitive property of LiCl/NaY composite materials. Chem. J. Chin. Univ.-Chin. 21 (2000) 1167-1170.

[119] K. Nagata, M. Nishino, K.S. Goto, Humidity sensor with $SrCe_{0.95}Yb_{0.05}O_3$ solid electrolyte for high temperature use, J. Electrochem. Soc. 135 (1988) 529-533.

[120] D.J. Yoo, K.H. Song, S.J. Park, Humidity sensing characteristics of CuO/ZnO heterojunctions, Tech. Digest, 4th Int. Meet. Chem. Sensors, Tokyo, Japan (1992) 108-111.

CHAPTER 2

TECHNICAL BACKGROUND

This chapter overviews the literature and discusses perovskite materials, proton conductivity, electrochemical sensor devices and thin film deposition methods. The first section introduces the $BaZrO_3$ structure used in this project and its Goldschmidt factor. The second section discusses proton conduction and proton transfer mechanisms. Protons are the dominant charge carriers at temperatures of 400 – 650°C. Their concentration in Y-doped $BaZrO_3$ thin films is influenced by humidity or partial pressure of water. Section 2.3 discusses other charge carriers that contribute to electrical conductivity and how they are affected by temperature and the partial pressure of oxygen. This is relevant because humidity measurements happen typically in air. Furthermore, the sensing mechanism is based on the dissociation of water into hydrogen and oxygen. Section 2.4 introduces basic models for the overall electrochemical absorption based humidity sensing mechanism in Y-doped $BaZrO_3$ thin films. In the final section, sputtering and pulsed laser depositions (PLD) are introduced as deposition methods for the $BaZrO_3$ thin films.

2.1 Introduction to perovskites

Perovskite is a mineral that was discovered and named by Gustav Rose in 1893 after a Russian mineralogist, L.A. Perovski [1-3]. The name perovskite was later used for the general group of crystals having the same structure. The basic chemical formula is ABO_3, where A and B are differently sized cations. The general crystal structure for a perovskite is cubic, with the A-cation situated in the middle of the cube, the B-cation placed in the corner and the anion (oxygen) in the center of the face. The A-cation can be either A^+ (Na, K, etc.), A^{2+} (Ca, Ba, etc.), or A^{3+} (La, Fe, etc.) and the B-site can be B^{5+} (Nb, W, etc.), B^{4+} (Ce, Zr, etc.), or B^{3+} (Mn, Fe, etc.). These materials find applications in many technological areas, such as ferroelectrics, catalysts, superconductors, and sensors.

Table 2-1 lists the applications and properties for selected perovskite materials.

2.1.1 $BaZrO_3$ structure

The alkaline earth metal compound $BaZrO_3$ has an ideal perovskite structure, i.e., cubic (Fig.2-1) with O atoms at the face center and metal atoms Ba and Zr at the cubic corner and body center, respectively [10, 26-28]. $BaZrO_3$ is a proton conducting material at high temperatures (500 – 700°C) [29], in which oxygen vacancies are generated by doping with trivalent cations, e.g., Y^{3+}. Besides its high proton conductivity ($1x10^{-5}$S/cm), it is also chemically and mechanically stable at elevated temperature.

Table 2-1: Properties and applications for some perovskite materials

Properties	Applications	Materials	References
Optical properties	Electrooptical modulator Laser host, switch Harmonic generator	(Pb, La)(Zr, Ti) O_3 $YALO_3$, $LiNbO_3$ $KNbO_3$	[4-9]
Ferroelectric/ Piezoelectric	Piezoelectric transducer P.T.C thermistor Electrostrictive actuator	$BaTiO_3$ $Pb(Zr, Ti)O_3$ $Pb(Mg, Nb)O_3$	[10-11]
Magnetic properties	Magnetic bubble Memory, ferromagnet	$GdFeO_3$ $LaMnO_3$	[12-13]
Dielectric	Multilayer capacitor Dielectric resonator Thin film resistor	$BaTiO_3$, $BaZrO_3$	[14]
Proton conducting	SOFC electrolyte Hydrogen sensor	$BaCeO_3$, $SrCeO_3$ $SrZrO_3$, (La, Sr) MnO_3	[15-16]
Ionic conducting	Solid electrolyte	$(La, Sr)(Ga, Mg)O_3$	[17]
Mixed conduting	SOFC electrode	$BaPrO_3$, $LaCoO_3$	[18-20]
Super conducting	Superconductor	$Ba(Pb, Bi)O_3$	[21-23]
Catalytic properties	Catalyst	$La(Ce, Co)O_3$	[24-25]

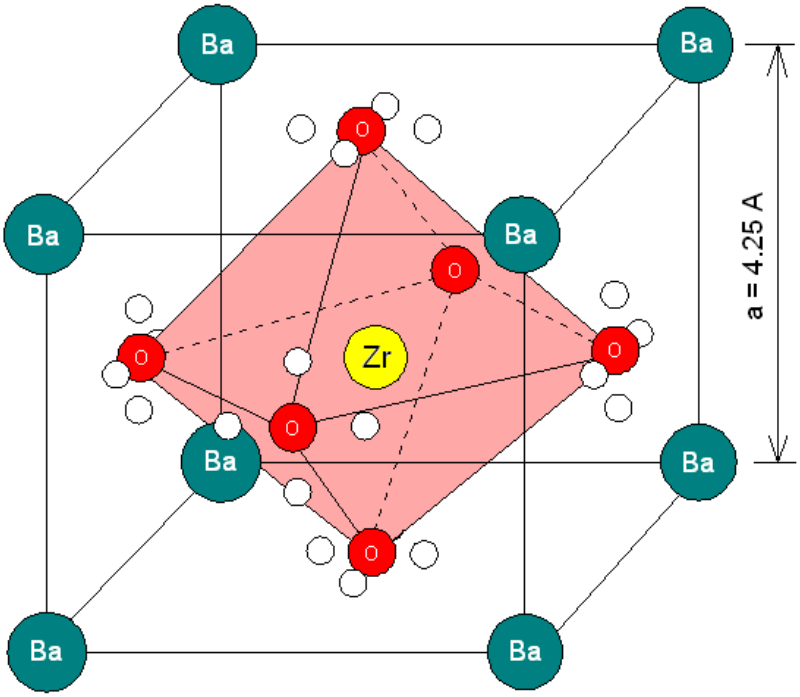

Fig. 2-1: Schematic of ideally packed ABO_3 perovskite structure, with A=Ba, B=Zr with the calculated lattice constant $a_0 = 4.25$ Å [31].

Therefore, it is a potential candidate as high temperature proton conductor with possible applications in high temperature gas sensing and fuel cells [29, 30]. The Goldschmidt tolerance factor *t* determines the degree of distortion of the perovskite [32]. It is based on the geometrical packing of charge spheres and is determined from ionic radii R_A, R_B, and R_O:

$$t = \frac{(R_A + R_o)}{\sqrt{2}(R_B + R_o)} \tag{2.1}$$

The $BaZrO_3$ structure is simple cubic as the ideally packed perovskite with tolerance factor t =1. In 1994, K.S. Knight proposed different distortion mechanisms in perovskite structures [33] based on *t* values that generally vary between 0.75 and 1. The less the distortion the crystal structure (i.e., the closer t =1), the higher the resulting electrical conductivity for the same doping concentration. For the same material depending on the

value of ionic radii that were used different t values were reported by different research groups. In the work presented here, $t = 1$ was assumed.

2.2 Proton conductivity

Electrical conductivity requires mobile charge carriers. These can include electrons, holes, or ions. Proton conduction as a type of ionic conductions was first suggested by Alfred Rene Jean Paul Ubbelohde and S.E. Rogersis [34]. The proton transfer motion is usually coupled with other phenomena, e.g., the internal rotation of methyl groups, since there is a strong interaction between a proton and the electron cloud of the environment [34].

2.2.1 Proton incorporation mechanism

The transport property of perovskite oxides varies with dopant materials, temperature and atmosphere. For example, when Y^{3+} is doped into the $BaZrO_3$ structure, oxygen vacancies are created that result in proton conduction in atmospheres containing H_2O vapor [35-36]

$$H_2O\ (gas) + Vo^{\bullet\bullet} + O_o^{x} \Leftrightarrow 2OH_o^{\bullet}, \qquad (2.2)$$

where two positively charged protonic defects ($OH_o^{\bullet}$) are formed. The charged protonic defects can diffuse through the bulk of the oxide when accompanied by the counter diffusion of oxide ion vacancies ($Vo^{\bullet\bullet}$). The equilibrium constant of the water incorporation is

$$K = [OH_o^{\bullet}]^2/([\ Vo^{\bullet\bullet}][\ O_o^{x}]\ p_{H2O}). \qquad (2.3)$$

A water molecule can split into a hydroxide ion and a proton. Simulations reported in the literature have been carried out to determine the enthalpy of the reaction presented in equation 2.2. A correlation has been found between the hydration enthalpies and the differences of the electronegativities of A and B site cations [37], where the most negative hydration enthalpies have been reported for similar electronegativity A and B site cations. The interaction between the dopants and incorporated proton is still not clear and is subject to continued investigation using computer simulation [38-42].

2.2.2 Proton transfer mechanisms

Mechanisms for proton transfer can be divided into two categories: the vehicle mechanism [4, 43-44] and the Grotthuss mechanism [45-47]. The transport of protons by another species is termed vehicle mechanism. Transport of protons between relatively stationary host anions is termed as the Grotthuss or free-proton mechanism.

According the vehicle mechanism, the proton does not migrate as H^+ but as H_3O^+, NH_4^+, etc., bonded to a "vehicle" such as H_2O and NH_3 and the complex moves as a whole. The "empty" vehicles move in the opposite direction (Fig. 2-2). This mechanism is mainly applied in compounds with loosely bonded molecules. A proton may be involved in two different O-H bonds: a short, strong bond with a proton donor and a long weak bond with a proton acceptor. Since the probability for the proton to jump the distance (250-280 pm) to the neighboring oxygen atom and stay there is small, the proton has to diffuse through the medium together with a "vehicle". The observed conductivity is directly dependent on the rate of vehicle diffusion Γ_D.

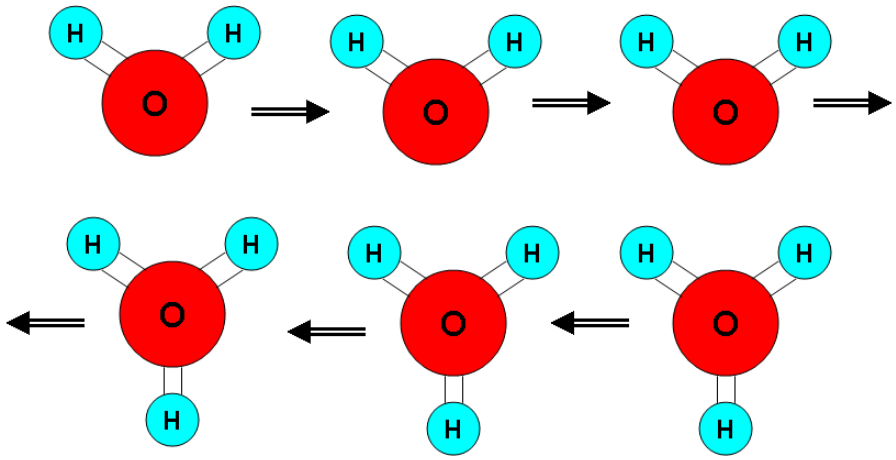

Fig. 2-2: The schematic plot of the vehicle mechanism for proton transfer, H_2O acts as an "empty" vehicle moves to one direction, and H^+ bonded with H_2O move as a whole to the other direction.

In the Grotthuss mechanism, the proton diffuses through reorientation and proton displacement (it is also called proton "hopping"). The relevant rates are the proton transportation Γ_{tras} and the molecular reorientation Γ_{reo}. The mechanism is observed in solid acids and the perovskite materials. A schematic for the Grotthuss mechanism for proton transfer in the perovskite structure is shown in Fig. 2-3 [48]: (a) proton is oriented to molecule on the left, (b) proton attraction connects it to the molecule on right, (c) proton severs connection to the molecule on the left, and the "hopping" process is completed. Quantum molecular dynamics simulations can help explain details of the Grotthuss mechanism in proton conducting perovskites [49-50]. The principal mechanism of the proton transport process is a rotational diffusion of the proton followed by a proton transfer towards an adjacent oxygen ion. The rotational motion of the proton in the O-H group is fast, which allows the reorientation of the proton and alignment with the next oxygen ion before the transfer process takes place. The energy barrier for that particular

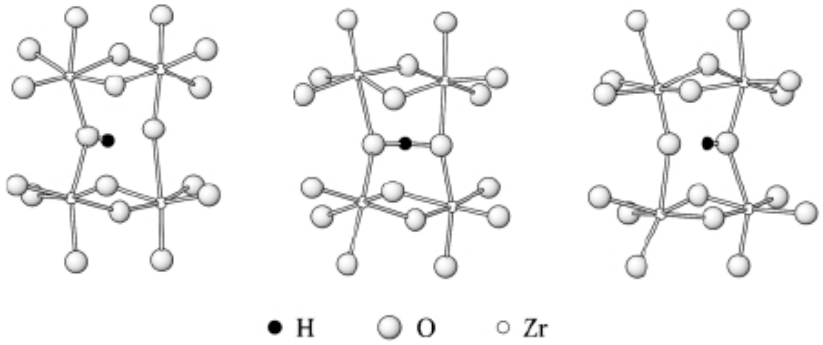

(a) (b) (c)

Fig. 2-3: The schematic plot of the Grotthuss mechanism for proton transfer in perovskite [48].

proton transfer process is then described as the energy difference between two states: a ground state in which the proton is bonded to a specific oxygen ion and a barrier state in which the proton is equidistant between two adjacent oxygen ions, as shown in Fig. 2-4 [50], prior to connecting to the next oxygen ion.

Simulation results for $LaAlO_3$, $BaZrO_3$, $BaCeO_3$, $CaZrO_3$ etc. indicate that the proton locally "softens" the lattice to allow the transient formation of hydrogen bonds, allowing the proton transfer between adjacent oxygen ions [51-55]. The energy difference between the ground state and the barrier state is less than 0.2 eV for most of the proton conducting perovskites found in literature. This is much less than the observed activation energy of 0.35-1.1 eV for proton conductors [29, 36, 56-57]. Further investigation reveals that the energy required for the adjacent oxygen ions to acquire an equivalent lattice position and to enter the barrier state is of the same magnitude as the activation energy. Therefore there must be an intermediate state between the ground and barrier states, which suggests that proton transfer may take place via a "barrierless" or tunneling mechanism. In other words, in order for proton tunneling to occur, a state at the same energy should be available on both sides of the barrier (Fig.2-5) [47]. This "relaxation"

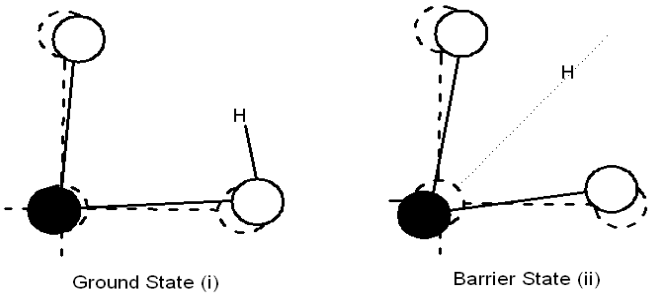

Fig. 2-4: Ground and barrier state configurations for proton transfer between adjacent oxygen ions. Solid lines represent the minimum energy positions, and the dashed lines indicate the perfect lattice geometry [50].

step is the key contribution to the proton conductivity activation energy.

2.3. Other charge carriers in Y-doped $BaZrO_3$

(oxygen ions, electrons, and holes)

As stated above, the transport properties of perovskite oxides vary with dopant material, temperature and atmosphere. For example, when Y^{3+} is doped into the $BaZrO_3$ structure, oxygen vacancies are created. In general, the conductivity, σ, of Y-doped $BaZrO_3$ exposed to water vapor can have contributions from four groups of charge carriers: oxygen ions (σ_{VO}••), electrons ($\sigma_{e'}$), holes (σ_{h}•) and protons (σ_{H}•) [54]

$$\sigma = \sigma_{VO}{}^{\bullet\bullet} + \sigma_{h}{}^{\bullet} + \sigma_{e'} + \sigma_{H}{}^{\bullet}$$

$$= F/V_m \left(2[V_O{}^{\bullet\bullet}]\,\mu_{VO}{}^{\bullet\bullet} + [h^{\bullet}]\,\mu_{h}{}^{\bullet} + [e']\,\mu_{e'} + [H^{\bullet}]\,\mu_{H}{}^{\bullet}\right), \qquad (2.4)$$

where F is the Faraday number, V_m is the molar volume of Y-doped $BaZrO_3$, $[V_O{}^{\bullet\bullet}]$, $[h^{\bullet}]$, $[e']$, and $[H^{\bullet}]$ are the molar concentration of oxygen vacancies, holes, electrons, and protons, respectively, and $\mu_{VO}{}^{\bullet\bullet}$, $\mu_{h}{}^{\bullet}$, $\mu_{e'}$, and $\mu_{H}{}^{\bullet}$, are the corresponding mobilities. Under

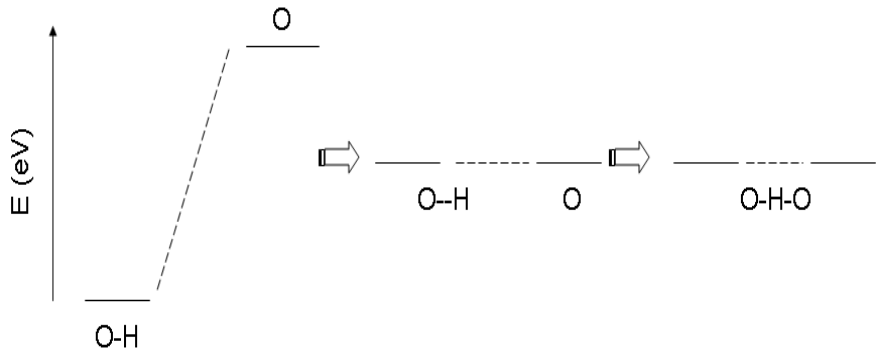

Fig. 2-5: A schematic of the proton transfer process indicating equilibration of the energy levels of the two adjacent oxygen ions [47].

equilibrium conditions, the material could exchange oxygen with the surrounding atmosphere at high p_{O2}

$$\tfrac{1}{2}\, O_2\,(gas) + Vo^{\bullet\bullet} \Leftrightarrow O_o^{x} + 2h^{\bullet}, \tag{2.5}$$

which leads to

$$\sigma = \sigma_{h\bullet}\, \alpha\, [V_O{}^{\bullet\bullet}]\, p_{O2}{}^{1/4}\, \alpha\, p_{O2}{}^{1/n}. \qquad 4 \le n \le 6 \tag{2.6}$$

For low p_{O2}

$$O_o^{x} \Leftrightarrow \tfrac{1}{2}\, O_2\,(gas) + Vo^{\bullet\bullet} + 2e', \tag{2.7}$$

which leads to

$$\sigma = \sigma_{e'}\, \alpha\, 1/([V_O{}^{\bullet\bullet}]\, p_{O2}{}^{1/4})\, \alpha\, p_{O2}{}^{-1/n}. \qquad 4 \le n \le 6. \tag{2.8}$$

When a proton conductor is exposed to a wet environment, H_2O is incorporated into the material filling up oxygen vacancies and the electron-hole density decreases, while the proton density increases as described in section 2.3.1. The total electrical conductivity can subsequently decrease or increase depending on the change in charge carrier

concentrations and charge carrier mobilites. The total conductivity of $Ba_3Ca_{1.18}Nb_{1.82}O_{9-\delta}$ (BCN 18) has been reported to increase with the absorption of H_2O at temperatures above 800°C [36]. The total conductivity of $BaZr_{0.93}Y_{0.07}O_{3-\delta}$, however, decreases with increasing p_{H2O} above 550°C and increases with increasing p_{H2O} below 550°C [29]. Such behavior suggests that the electron-hole conductivity exhibits a stronger dependence on temperature and p_{O2} than the proton conductivity. On the other hand, the increase in proton conductivity is less than the decrease in electron-hole conductivity at elevated temperature or high p_{O2} while the increase in proton conductivity exceeds the decrease in electron-hole conductivity at lower temperature or lower p_{O2} [29]. The total conductivity of this material is however about one order of magnitude smaller in a dry environment, which suggests Y-doped $BaZrO_3$ is preferably a high-temperature ($T < 700°C$) proton conductor [29, 36].

2.4 Electrochemical sensor devices

A model explaining the sensing mechanism for high temperature humidity sensors based on Y-doped $BaZrO_3$ thin films is shown in Fig. 2-6. The material exhibits oxygen vacancies when doped with a lower valence ion, e.g., yttrium on the Zr-site. The same material when heated in an environment containing H_2O allows the absorption of H_2O into the lattice. Absorption of H_2O into the lattice lowers the oxygen vacancy concentration, and releases protons by the following reaction,

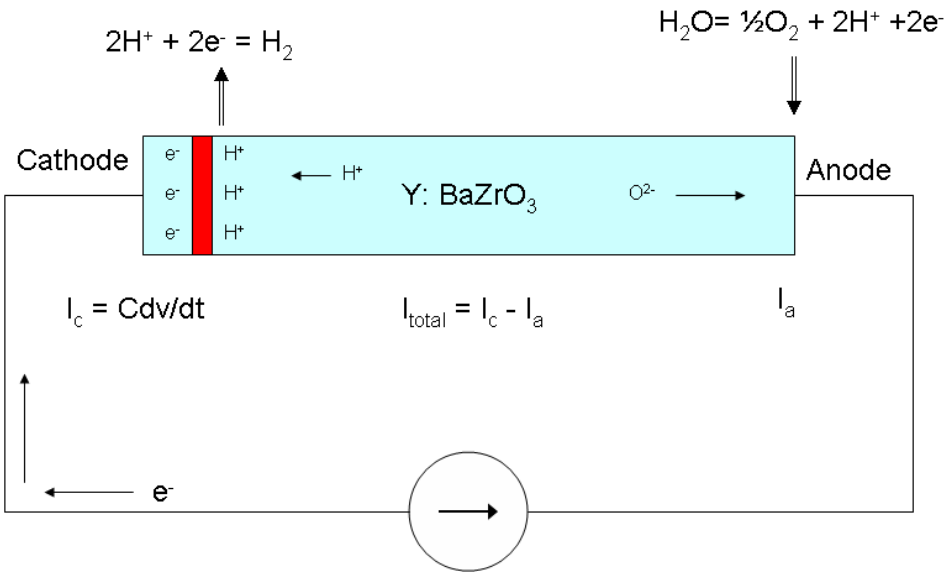

Figure 2-6: Conduction mechanism of Y-doped $BaZrO_3$ thin films for humidity sensors

$$BaZr_{(1-x)}Y_xO_{(3-x/2)} + (y/2)H_2O \rightarrow BaZr_{(1-x)}Y_xH_yO_{(3-x/2+y/2)} \quad \text{where } y<x \qquad (2.9)$$

H_2O molecules disassociate while the water vapor is passing by the Y-doped $BaZrO_3$ material at high temperature. H_2O molecules will fill in oxygen vacancies, and release protons and electrons at the anode. Since protons and electrons travel in opposite direction, H^+ travels through the material and combines with e^- at the cathode becoming H_2 that will escape into the air. O^{2-} hops through the material in opposite direction and combines with the positive charges becoming O_2 that will be released into the air at the anode.

From the electrical point of view, the cathode is a leaky capacitor with its first plate being the electrode and the second plate being a double-layer capacitor made from the ionic charges accumulating at the interface (Fig. 2-7). The voltage applied to it determines the energy of this capacitor. This model can have a cumulative effect (electrochemical polarization) on the sensing measurements, when the products of the

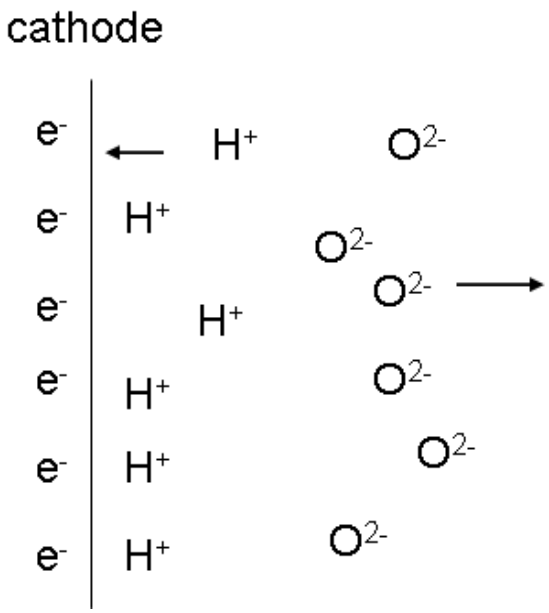

Fig. 2-7: Model of a capacitor layer at the cathode.

electrochemical reaction are not removed rapidly from, and the electro-active species supplied to, the interface. Therefore, electrochemical polarization may occur in this sensor systems as follows: 1) the negative charges are accumulated at the cathode when no proton or very few protons travels through the material, 2) the positive charges are accumulated at the anode when there are not enough oxygen ions hopping through the material or the speed of oxygen ion hopping is slower than the recombination. If both possibilities occur at the same time, the material becomes a capacitor that allows no current flow through unless a high voltage or a high frequency voltage is applied.

2.5 Thin film deposition

Thin film deposition techniques are typically in the range of several nm to a few μm. A variety of materials and methods can be used. The most relevant methods here are vacuum based physical and chemical vapor deposition. In physical vapor deposition

(PVD) (a line of sight impingement technique) material is deposited by ablating a target with the desired material in a vacuum environment, leading to a vapor that is deposited on a substrate. Examples are sputtering and pulsed laser deposition (PLD), both of which typically allow maintaining the approximate composition of the target in the resulting film. Chemical vapor deposition (CVD) uses the decomposition of precursors and chemical reactions which transform gaseous molecules, into a solid material, depositing in the form of a thin film on the substrate surface, i.e., a diffusive-convective mass transfer technique. This work focuses on PLD and sputtering as deposition methods, circumventing the need for the development of suitable CVD precursors and processes.

2.5.1 Sputtering

Sputtering is a vacuum coating process which physically removes portions of a coating material from a target. The process works by bombarding the surface of the sputtering target with gaseous ions (typically Ar) under high voltage acceleration. Atoms or molecules of the target material are ejected into the gas phase and deposit on the substrate. Fig. 2-8 [60] schematically shows the sputtering process. Sputtering is a preferred method of thin film coating in many applications due to the wider choice of materials that can be deposited as well as the easier maintenance of the target material composition in the film. The deposition rate is however very slow for some materials, typically for all oxides and ceramics. Some impurities are easily introduced into the film during the sputtering process. Sputtering can be carried out using DC, pulsed DC, RF and RF magnetron generated plasmas. The Ar atoms ionize to become Ar^+ ions. Whilst simple DC sputtering will allow the continued ablation of the target for conductive materials, nonconductive materials require pulsed DC or RF sputtering, since the target

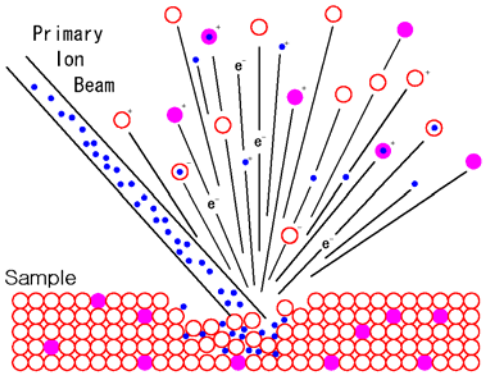

Fig. 2-8: A schematic of the sputtering process [60].

would otherwise charge upon constant bombardment with ions and eventually repel the ions, stopping the sputtering process. Using an RF plasma alleviates this problem. Magnetron sputtering makes use of magnets attached to the backside of the substrate that forces the electrons in the plasma onto an elliptical path in close vicinity of the target, leading to a higher ionization rate of Ar in the vicinity of the target and hence a high sputtering rate. A consequence of the localized high ionization and sputtering rate is the formation of a "race track" that erodes the target more rapidly along the path of the electrons. The sputter rate also depends on the incident angle of the ions with respect to the target, with a maximum around 60° (orthogonal impact causes the ion momentum to dissipate in the bulk of the target, parallel direction of ion flight does not transfer any momentum). Sputtering can be carried out in inert gases (such as Ar) and reactive gases, yielding, e.g., oxide and nitride films, when depositing in O_2 or N_2.

2.5.2 Pulsed laser deposition (PLD)

Pulsed laser deposition (PLD) is a thin film deposition technique where a high power pulsed laser beam is focused inside a vacuum chamber striking a target. The target

material is vaporized and deposited onto a substrate. The process can occur in ultra high vacuum or in the presence of a background gas. Fig.2-9 [61] shows the basic setup for PLD. While the basic setup of the system is simple, the physical phenomena of the laser-target interaction and film growth are quite complex. When a laser pulse is absorbed by the target, energy is first converted to electronic excitation and then into thermal, chemical and mechanical energy resulting in evaporation, ablation, plasma formation and even exfoliation [62].

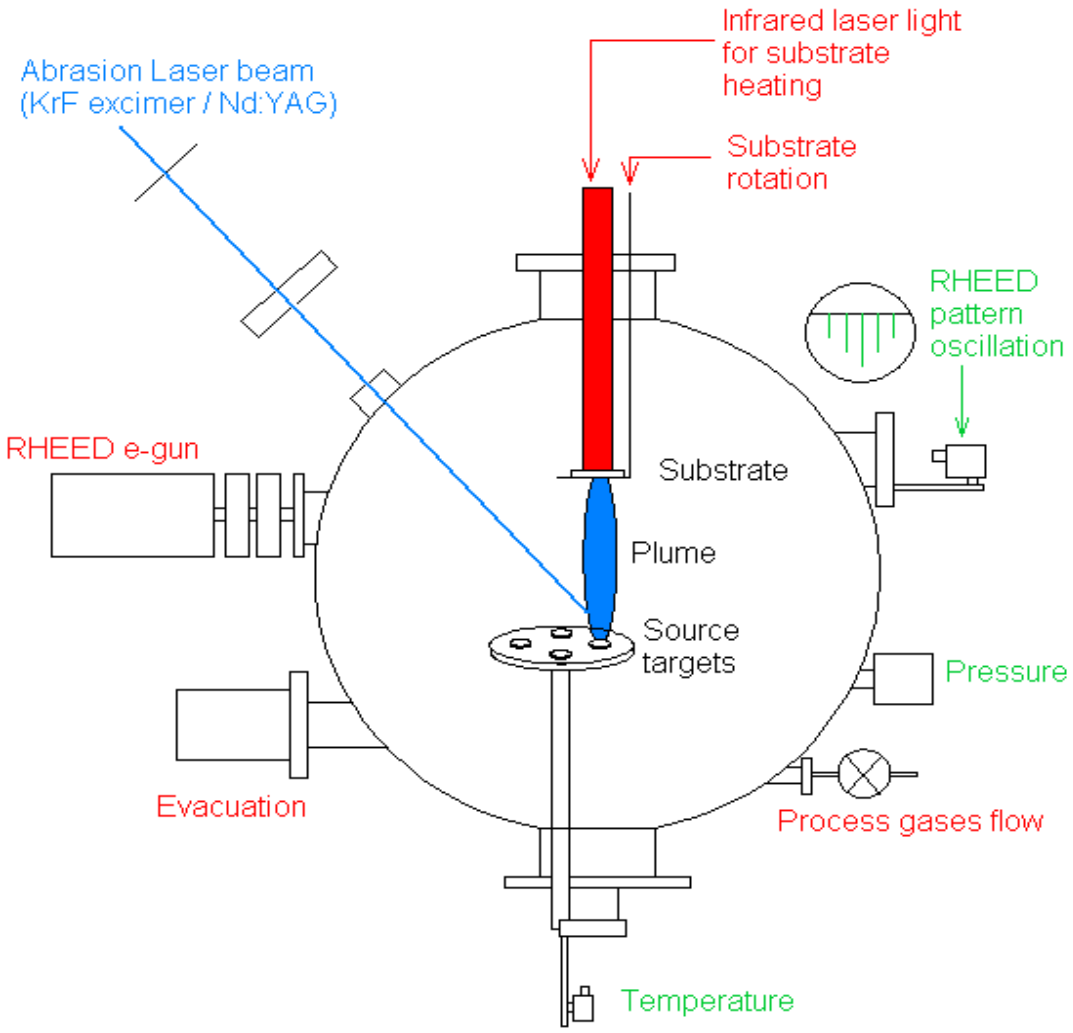

Fig.2-9: Schematic diagram of a laser deposition setup [61].

Each of these steps is crucial in determining crystallinity, uniformity, and stoichiometry of the film. The PLD system has a versatile range of materials. The resulting films are generally not uniform even cross areas as small as 1 cm^2. It is also not well suited for large scale production.

2.6 References

[1] J. Lloyd, J. Mitchinson, What's the Commonest Material in the World, the Book of General Ignorance, Faber & Faber, ISBN 0-571-23368-6.

[2] L.G. Tejuca, Properties and applications of perovskite-type oxides (1993) 382.

[3] R.H. Mitchell, Perovskites modern and ancient (2002) 318.

[4] C.D. Zuo, Doping and defects structure for mix-conducting ceramics for gas separation, Ph.D. dissertation (2006).

[5] R. Byer, Non-linear optical and solid state lasers: 200, IEEE Journal of Selected Topics in Quantum Electronics 2000, 6(6) 911-930.

[6] Y. Fainman, J. Ma, S. Lee, Molecular geometry and polarizability of small cadmium selenide clusters from all-electron ab initio and density functional theory calculations, Materials Science Reports 9 (1993) (2-3), 53.

[7] M. Moret, M. Devillers, K. Worhoff, P. Larsen, Optical properties of $PbTiO_3$, $PbZr_xTi_{1-x}O_3$, and $PbZrO_3$ films deposited by metalorganic chemical vapor on $SrTiO_3$ J. Appl. Phys. 2002, 92(1) 468.

[8] F. Jona, G. Shirane, R. Pepinsky, Optical study of $PbZrO_3$ and $NaNbO_3$ single crystals, Physical Review 97(6) (1995) 1584-1590.

[9] M.Weber, M. Bass, G. Demars, Multiphonon relaxation of rare-earth ions in yttrium orthoaluminate, J. Appl. Phys. 42(1) (1971) 301

[10] D. Dimos, C. Mueller, Perovskite thin films for high-frequency capacitor applications, Annual Review of Materials Science 28 (1998) 397-419.

[11] T. Shaw, S. Trolier-McKinstry, P. McIntyre, The properties of ferroelectric films at small dimension, Annual Review of Materials Science 30 (2000) 263-298.

[12] J. DeTeresa, M. Ibarra, P. Algarabel, C. Ritter, C. Marquina, J. Blasco, J. Garcia, A. delMoral, Z. Arnold, From magnetoelectronic to biomedical applications based on the nanoscale properties of advanced magnetic materials, Nature 386 (6622) (1997) 256-259.

[13] M. J. Gilleo, Metal-insulator transitions and weak ferromagnetism in the electron-correlated system $Nd_{1-x}Ca_xTiO_3$ ($0 \leq x \leq 1$), Chem. Phys. 24(6) (1956) 1239.

[14] H. Kishi, Y. Mizuno, H. Chazono, Ultrashort electromagnetic pulse radiation from YBCO thin films excited by femtosecond optical pulse, Japanese Journal of Applied Physics Part 1-Regular Papers Short Notes and Review Papers 42(1) (2003) 1.

[15] H. Iwahara, H. Uchida, K. Ono, K. Ogaki, High temperature C-1 gas fuel cells using proton conducting solid electrolyte, J. Electrochem. Soc. 135(2) (1988) 529-533.

[16] H. Iwahara, H. Uchida, J. Kondo, Galvanic cell-type humidity sensor using high temperature-type proton conductive solid electrolyte, J. Appl. Electrochem. 13(3) (1983) 365-370.

[17] K. Huang, M. Feng, J. Goodenough, C. Milliken, A solid oxide fuel cell based on Sr- and Mg-doped $LaGaO_3$ electrolyte: the role of a rare-earth oxide buffer, J. Electrochem. Soc. 144(10) (1997) 3620-3624.

[18] J. Mizusaki, J. Tabuchi, T. Matsuura, S. Yamauchi, K.J. Fueki, Electrical conductivity and Seebeck coefficient of nonstoichiometric $La_{1-x}Sr_xCoO_{3-\delta}$, J. Electrochem. Soc. 136(7) (1989) 2082-2088.

[19] T. Fukui, S. Ohara, S. Kawatsu, Conductivity of $BaPrO_3$ based perovskite oxides, J. Power Sources 71(1-2) (1998) 164-168.

[20] R. Mukundan, P. Davies, W. Worrell, Electrochemical characterization of mixed conducting $Ba(Ce_{0.82}yPryGd_{0.2})O_{2.9}$ cathodes, J. Electrochem. Soc. 148(1) (2001) A82-A86.

[21] J. Ihringer, J. Michael, W. Prandl, A. Hewat, T. Wroblewski, Crystal structure of the ceramic superconductor $BaPb_{0.75}Bi_{0.25}O_3$, Zeitschrift Fuer Physik B-Condensed Matter 82(2) (1991) 171-176.

[22] L. Lin, Ferroelectric/superconductor heterostructures, Materials Science and Engineering R-Reports 29(6) (2000) 153-181.

[23] T. Sampathkumar, S. Srinivasan, T. Nagarajan, U. Balachandran, Properties of $YBa_2Cu_3O_{7-\delta}-BaBiO_3$ composite superconductors, Applied Superconductivity 2(1) (1994) 29.

[24] R. Spinicci, A. Tofanari, A. Delmastro, D. Mazza, S. Ronchetti, Catalytic properties of stoichiometric and non-stoichiometric $LaFeO_3$ perovskite for total oxidation of methane, Mater. Chem. Phys. 76(1) (2000) 20-25.

[25] L. Forni, I. Rossetti, Catalytic combustion of hydrocarbons over perovskites, Applied Catalysis B-Environmental 38(1) (2000) 29-37.

[26] J. Ho, E. Heifets, B. Merinov, Ab initio simulation of the $BaZrO_3$ (001) surface structure, Surface Sci. 601 (2007) 490-497.

[27] I. Ahmed, S.G. Eriksson, E. Ahlberg, C.S. Knee, H. Goetlind, L.G. Johansson, M. Karlsson, A. Matic, L. Boerjesson, Structural study and proton conductivity in Yb-doped $BaZrO_3$, Solid State Ionics, vol. 178 (2007) 515-520.

[28] E. Heifets, J. Ho, B. Merinov, Density functional simulation of the $BaZrO_3$ (001) surface structure, Phys. Rev. B (2007) 75 155431-15.

[29] W. Wang, A.V. Virkar, Ionic and electron-hole conduction in $BaZr_{0.93}Y_{0.07}O_{3-\delta}$ by 4-probe dc measurements, J. Power Source 142 (2005) 1-9.

[30] K. Yajima, H. Koide, N. Takai, N. Fukatsu, H. Iwahara, Application of hydrogen sensor using proton conductive ceramics as a solid-electrolyte to aluminum casting industries, Solid State Ionics, vol. 79 (1995) 333-357.

[31] P.G. Sundell, M.E. Bjoerketun, G. Wahnstroem, Density-functional calculations of prefactors and activation energies for H diffusion in $BaZrO_3$, Phys. Rev. 76 (2007) 094301-7.

[32] K.A. Walsh, Beryllium chemistry and processing, (2009) 575, ISBN 13-978-0-87170-721-5.

[33] K. S. Knight, Structural phase transitions in $BaCeO_3$, Solid State Ionics, vol. 74 (1994) 109-117.

[34] S.E. Rogers, A.R. Ubbelohde, Proton mobility in solids, Trans. Faraday Soc., vol. 46 (1950) 1051.

[35] W. Wang, Transport in proton conducting perovskite oxides and solid-state electrochemical devices, Ph.D dissertation, 2004.

[36] W. Wang, A.V. Virkar, A conductimetric humidity sensor based on proton conducting perovskite oxides, J. Sens. Actuators, B Chem. 98 (2004) 282-290.

[37] M.S. Islam, R.A. Davies, J.D. Gale, Proton migration and defect interactions in the $CaZrO_3$ orthorhombic perovskite: a quantum mechanical study, Chem. Mater. 13 (2001) 2049-2055.

[38] G.C. Mather, M.S. Islam, Defect and dopant properties of the $SrCeO_3$-based proton conductor, Chem. Mater. 17 (2005) 1736-1744.

[39] R.A. Davies, M.S. Islam, A.V. Chadwick, G.E. Rush, Cation dopant sites in the $CaZrO_3$ proton conductor: a combined EXAFS and computer simulation study, Solid State Ionics, vol.130 (2000) 115-122.

[40] S. Mimuro, S. Shibako, Y. Oyama, K. Kobayashi, T. Higuchi, S. Shin, S. Yamaguchi, Proton incorporation and defect chemistry of Yb-doped $BaPrO_3$, Solid State Ionics, vol. 178 (2007) 641-647.

[41] C. Shi, M. Morinaga, Doping Effects on Proton Incorporation and Conduction in $SrZrO_3$, Wiley Interscience (2005).

[42] N. Bonanos, Transport properties and conduction mechanism in high-temperature protonic conductors, Solid State Ionics, vol. 967 (1992) 53-56.

[43] T. Norby, Solid state protonic conductors, present main applications and future prospects, Solid State Ionics, vol. 125 (1999) 1-4.

[44] J. B. Goodenough, Designing solid electrolytes III: proton conduction and composites, Solid State Microbatteries (1990).

[45] K.D. Kreuer, Th. Dippel, N.G. Hainovsky J. Maier, Proton conductors, Ber. Bunsenges. Phys. Chem. 96 (1992) 1736-1742.

[46] K.D. Kreuer, Proton conductivity: materials and applications, Chem. Mater. (1996) 610-641.

[47] K.D. Kreuer, Proton conducting oxides, Annu. Rev. Mater. Res. 33 (2003) 333-359.

[48] M.S. Islam, R.A. Davies, J.D. Gale, Hop, skip or jump? Proton transport in the CaZrO3 perovskite oxide, J. Chem. Comm. (2001) 661-662.

[49] M.S. Islam, Ionic transport in ABO_3 perovskite oxides: a computer modelling tour, J. Mater. Chem. 10 (2000) 1027-1038.

[50] K.D. Kreuer, On the complexity of proton conduction phenomena, Solid State Ionics, vol. 149 (2000) 136-137.

[51] R. Glockner, M.S. Islam, T. Norby, Protons and other defects in BaCeO: a computational study, Solid State Ionics, vol. 122 (1-4) (1999) 145-156.

[52] R.A. Davies, M.S. Islam, J. D. Gale, Dopant and proton incorporation in perovskite-type zirconates, Solid State Ionics, vol.126 (1999) 323-335.

[53] H. G. Bohn, T. Schober, Electrical conductivity of the high temperature proton conductor $BaZr_{0.9}Y_{0.1}O_{2.95}$, J. Am. Ceram. Soc. 83 [4] (2000)768-772.

[54] H. Iwahara, T. Yajima, T. Hibino, K. Ozaki, H. Suzuki, Study on current efficiency of steam electrolysis using a partial protonic conductor $SrZr_{0.9}Yb_{0.1}O_{3-\alpha}$, Solid State Ionics, vol. 61 (1993) 243-251.

[55] T. Yajima, H. Iwahara, Defect structure analysis of B-site doped perovskite-type proton conducting oxide $BaCeO_3$ Part 1: The defect concentration of $BaCe_{0.9}M_{0.1}O_{3-\delta}$ (M = Y and Yb), Solid State Ionics, vol. 53-56 (1992) 983-989.

[56] T. Scherban, A.S. Nowick, Protonic conduction in Fe-doped $KTaO_3$ crystal, Solid State Ionics, vol. 53-56 (1992) 1004-1008.

[57] Y. Larring, T. Norby, Protons in $LaErO_3$, Solid State Ionics, vol. 70/71 (1994) 305-310.

[58] H. G. Bohn, T. Schober, Electrical conductivity of the high temperature proton conductor $BaZr_{0.9}Y_{0.1}O_{2.95}$, J. Am. Ceram. Soc. 83 [4] (2000) 768-772.

[59] J. Janata, Principles of Chemical Sensors, Springer (1989), ISBN-13: 978-0306431838

[60] F. Solzbacher, Lecture notes: Sensors and Actuators (2006).

[61] H. U. Krebs, M. Weisheit, J. Faupel, E. Sueske, T. Scharf, C. Fuhse, M. Stoermer, K. Sturm, M. Seibt, H. Kijewski, D. Nelke, E. Panchenko, M. Buback, Pulsed laser deposition – a versatile thin film technique, Appl. Phys. A 75, 551 (2002).

[62] M.S. Shegde, Epitaxial oxide thin films by pulsed laser deposition: retrospect and prospect, Pro. Indian Acad. Sci, vol. 113, Nos 5 & 6 (2001) 445-458.

CHAPTER 3

HIGH TEMPERATURE HUMIDITY SENSORS BASED ON SPUTTERED Y-DOPED $BaZrO_3$ THIN FILMS

Sensors and Actuators B 137 (2009) 578-585

reprinted with permission

Sensors and Actuators B 137 (2009) 578–585

Contents lists available at ScienceDirect

Sensors and Actuators B: Chemical

journal homepage: www.elsevier.com/locate/snb

High temperature humidity sensors based on sputtered Y-doped $BaZrO_3$ thin films

XiaoXin Chen[a,*], Loren Rieth[a], Mark S. Miller[a,b], Florian Solzbacher[a,b,c]

[a] Department of Electrical Engineering, University of Utah, Salt Lake City, UT, USA
[b] Department of Material Sciences and Engineering, University of Utah, Salt Lake City, UT, USA
[c] Department of Bioengineering, University of Utah, Salt Lake City, UT, USA

ARTICLE INFO

Article history:
Received 17 September 2008
Received in revised form 12 January 2009
Accepted 12 January 2009
Available online 30 January 2009

Keywords:
Thin film
Microsensor
Humidity
High temperature
Y-doped $BaZrO_3$ material

ABSTRACT

Sputter deposited Y-doped $BaZrO_3$ thin films ($BaZr_xY_{1-x}O_{3-y/2}$, $x = 0.2$, $y > 0$), were investigated as to their viability for reliable, long-term stable humidity or water vapor microsensors operating at high operating temperatures ($T > 400\,^{\circ}C$). Reliable exhaust gas composition measurements at these temperatures could allow optimization of power plant efficiency and reduce emissions. Electrical conductivity and gas sensitivity tests on bulk Y-doped $BaZrO_3$ in environments with varying humidity suggest that this material could be suitable as a highly selective humidity sensor with sensitivities between 2 atm^{-1} and 26 atm^{-1} in the temperature range of 500–700 °C, based on an ionic proton conduction mechanism [W. Wang, A.V. Virkar, Ionic and electron–hole conduction in $BaZr_{0.93}Y_{0.07}O_{3-\delta}$ by 4-probe dc measurements, J. Power Sources 142 (2005) 1–9; W. Wang, A.V. Virkar, A conductimetric humidity sensor based on proton conducting perovskite oxides, J. Sens. Actuators, B, Chem. 98 (2004) 282–290]. Thin films of $BaZrO_3$:Y were investigated for their potential to significantly reduce sensor response time, increase sensitivity, and allow integration in microsensor platforms. Unlike other sensors that are based on adsorption, the sensing mechanism presented here at temperatures >400 °C should be based on absorption of H_2O, which dissolves into the $BaZrO_3$:Y lattice, "fills in" the oxygen vacancies, and releases protons. Since protons have a higher mobility than oxygen ions, they would dominate the electric conductivity.

XRD spectra from all as-deposited and annealed $BaZrO_3$:Y films show that the material changed from amorphous to crystalline at annealing temperatures >500 °C. After annealing, the samples exhibit an increasing particle size from 70 nm to 167 nm and an increase of root mean squared (RMS) roughness (from 1.3 nm to 4.2 nm) with increasing film thickness (200–500 nm).

The film conductivity increases as a function of temperature (from 100 °C to 400 °C) and upon exposure to a humid atmosphere, supporting our hypothesis of a proton conduction based conduction and sensing mechanism. The water vapor sensitivity was measured using 0.058 atm partial pressure of water at 400 °C. Sensitivity values ranging from 22 atm^{-1} to 62 atm^{-1} with a response time of $\tau_{60} \approx 6$ s were achieved. We have demonstrated Y-doped $BaZrO_3$ thin film humidity sensors that operate at high temperatures.

1. Introduction

Globally, restrictions on emissions from fossil fuel fired power plants and internal combustion engines are becoming more stringent [3,4]. Microscale (MEMS) gas sensing devices are being developed to help monitor emissions and provide feedback for advanced engine controls and emission control devices. The gas species of interest include CO, CO_2, hydrocarbons, H_2S, NO_x, H_2O, etc. Power plants operate at high temperatures and high pressures. Therefore, sensing devices have to be reliable in these conditions. Electro-ceramic material such as e.g. Yttrium Stabilized Zirconia (YSZ) has been used in gas sensors due to their high selectivity and reliable sensitivity at high temperatures [5–7]. Y-doped $BaZrO_3$ has been studied in various applications and has demonstrated high selectivity to humidity [1,2,8,25–27]. Literature reports focus on bulk or thick film material, not on thin films. This work studies Y-doped $BaZrO_3$ thin film sensors for measuring of relative humidity at high temperatures ($T > 400\,^{\circ}C$). The sensor response time may be reduced significantly compared to bulk sensors, while increasing sensitivity.

Many examples of humidity sensor based on chemisorption (surface adsorption) of H_2O or water vapor have been reported [8–11], but often lack selectivity towards to NO_x, and O_2 [12–15]. Surface/chemisorption based mechanisms respond to almost all species present in the gas atmosphere. An alternative sensing mechanism is based on absorption of H_2O into the lattice. This

* Corresponding author. Tel.: +1 8016714407.
E-mail address: Xiao_C@yahoo.com (X. Chen).

0925-4005/$ – see front matter © 2009 Elsevier B.V. All rights reserved.
doi:10.1016/j.snb.2009.01.024

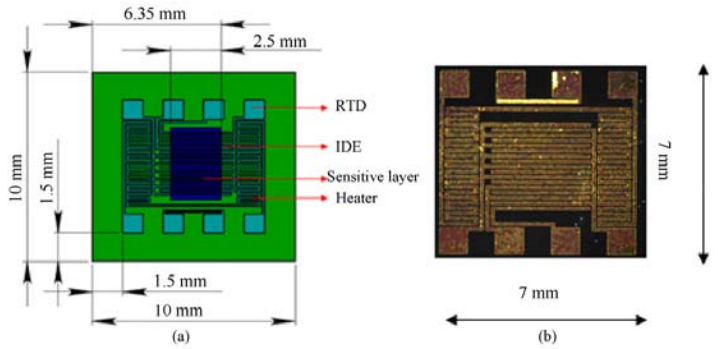

Fig. 1. (a) 2D design model of the interdigitated electrodes (IDE) sensor test structures, which including resistive temperature device (RTD), 10 pairs of interdigitated electrodes (IDE), heater, and deposited sensitive layer, and (b) the fabricated gas test structure sample with Cr and Au metallization.

mechanism ought to be more selective since not all species readily dissolve into a solid lattice. $BaZrO_3$ is a ceramic material with Perovskite structure that has been reported to have high chemical stability (i.e. it does not change its basic chemical composition and structure when exposed to other gaseous species, easily) and high proton conductivity when doped appropriately [16,17]. When doped with a lower valent ion on the Zr-site, the material contains oxygen vacancies and can exhibit oxygen ion conductivity. The material also can feature p-type electronic conductivity in atmospheres with high oxygen partial pressure. Literature reports that the conductivity of this material usually increases with an increase in humidity and temperature [1,2]. At temperatures $T > 400\,^{\circ}C$, H_2O dissolves into the lattice thus "filling in" the oxygen vacancies and releasing protons into the structure. It could therefore yield a stable, yet sensitive material that allows a repeatable and selective and sensitive sensing mechanism [18–22].

2. Experimental methods

Y-doped $BaZrO_3$ films were deposited by sputter deposition, and then characterized by X-ray photoelectron spectroscopy (XPS), X-ray diffraction (XRD), Atomic force microscopy (AFM), electrical conductivity and water vapor sensitivity measurements at 400 °C. The measurements determined the microstructure, surface morphology, composition, and gas sensitivity of these films. Electrical conductivity as function of temperature and water vapor humidity sensing characteristics of the films were measured using a custom-built gas sensor test station.

2.1. Device fabrication

Gas sensor test structures (Fig. 1) were fabricated in Silicon based microfabrication technique. Single-side polished, 2 in. n-type Si wafers were used as substrates. The wafers were wet oxidized at 1050 °C, 1 slm O_2 carries 1 slm water vapor, 50 min, yielding 250 nm of SiO_2 as electrical insulation between the active gas or humidity sensitive layer and the Si substrate. Gas and humidity sensitive films were deposited as blanket films on top of the SiO_2 layer and annealed as described below. A Cr (20 nm) and Au (180 nm) thin film metal layer was sputtered on top of the gas sensing films and patterned using liftoff. The deposition of the metal on top of the film allowed for higher temperature annealing of the sensing films and higher sensitivity.

2.2. Material studies

The electroceramic thin films were deposited from a 3 in. diameter, 99.9% pure ceramic $BaZr_{0.8}Y_{0.2}O_y$ sputtering target. The films were sputter deposited at room temperature using an UHP (99.999%) Ar sputtering ambient in a Denton Discovery 18 system. A deposition pressure of 1.3 mTorr was maintained using 5 sccm Ar flow and RF (13.56 MHz) power of 100 W, yielding an average deposition rate of 0.53 Å/s. Films with thicknesses of 200, 300, 400 and 500 nm were deposited. All films were annealed in air at 800 °C for 3 h. Film thickness and deposition rates were determined using a Tencor stylus profilometer and a Woolam V-Vase spectroscopic ellipsometer. X-ray photoelectron spectroscopy measurements were made using a Kratos Axis ULTRA^{DLD} system using monochromatic Al Kα radiation. Composition data was recorded for as received samples and after 4 min of Ar^+ ion beam etching. X-ray diffraction measurements were made using a Philips X'Pert system using Cu Kα radiation in the Bragg-Brentano geometry for 2θ angles from 10° to 90°. Atomic force microscopy micrographs were collected with a Veeco Dimension 3000 system using etched Si tapping mode tips with a nominal tip radius of ~5 nm.

2.3. Water vapor sensitivity measurements

The water vapor sensing characteristics for sputter deposited $BaZrO_3$:Y films were measured using a custom-built gas sensor test station. Sample chips were placed on a hotplate in a stainless steel chamber and contacted with probe needles attached to a PC/labview controlled Keithley digital multimeter in voltage measurement mode. N_2 carrier gas at 50 sccm was passed through a water bath at 80 °C, saturating the gas at 0.468 atm water vapor pressure. Before the water vapor reaches the test chamber, it diluted with 1380 sccm N_2. Once the saturated gas enters the test chamber it is heated to the current measurement temperature and the partial pressure and therefore relative humidity of the gas drops as a function of temperature. The partial pressure of water is calculated by the percentage of total gas flow in 1 atmosphere.

Sample resistance values were determined based on the voltage measurements using a 0.07 μA supply current that would not lead to self heating of the film. The temperature dependence of resistance was measured at 200, 300, and 400 °C. The response to water vapor was measured at 0.058 atm partial pressure of water at 400 °C. The film conductivity was determined using

$$\sigma = \frac{L}{RAn} \tag{2.3.1}$$

Table 1
Film composition quantified by XPS measurements for samples as function of thickness for (a) nominal composition, (b) 200, (c) 300, and (d) 400, (e) 500 nm, annealed at 800 °C in air.

Sample name	(a)	(b)		(c)		(d)		(e)	
	At conc (%)	At conc (%) as received	At conc (%) after 4 min Ar^+ etching	At conc (%) as received	At conc (%) after 4 min Ar^+ etching	At conc (%) as received	At conc (%) after 4 min Ar^+ etching	At conc (%) as received	At conc (%) after 4 min Ar^+ etching
Ba 3d	20	6	10	6	12	6	9	8	8
O 1s	60	54	59	58	55	49	59	56	59
Zr 3p	16	12	23	12	24	15	25	17	25
Y 3p	4	6	8	4	7	4	7	6	8
C 1s	0	22	0	20	2	26	0	13	0

where σ is the film conductivity ($[\sigma] = 1$ S/cm), R is the measured resistance ($[R] = 1$ MΩ), A is the cross sectional area of the sample ($[A] = 1$ cm^2), L is the distance between each interdigitated electrode ($[L] = 1$ cm), and n is the number of interdigital electrode pairs ($n = 10$). In order to check the selectivity of the material, the cross sensitivity of the samples was measured at 400 °C as a function of the test gas concentration (N_2, O_2, H_2, NH_3, NO_2, and H_2O).

3. Results and discussion

3.1. Film characterization

The chemical composition of the films was measured by XPS from as received samples, and after ion beam etching. The film compositions were quantified from the spectra and are presented in Table 1. XPS data indicates that the film composition is significantly different from the nominal target composition (column B) showing a clear Ba deficit. The significant carbon concentration present prior to etching is attributed to advantious carbon on the film surface. The presence of Si suggests that the films are discontinuous, such that the substrate can contribute to the photoelectron spectra.

The crystallinity of doped $BaZrO_3$ was investigated both before and after annealing. The materials changed from amorphous or weakly crystalline to polycrystalline structure after annealing at temperatures of 800 °C for 3 h in air. To date, polycrystalline films have only been achieved after annealing, XRD spectra from before and after annealing are presented in Fig. 2.

The XRD spectra indicate that unannealed films were amorphous and became polycrystalline after heat treatment. The dashed vertical lines on the plots represent the JCPDS values for (1 1 0) and (2 0 0) reflections for $BaZrO_3$. The reflections are shifted to higher 2θ values compared to the JCPDS database, which would be consistent with the films being under compressive stress in the out-of-plane direction. Mud flat cracking has been observed in films thicker than 300 nm, suggesting in-plane residual tensile stress in the film, which is consistent with out-of-plane compressive stress

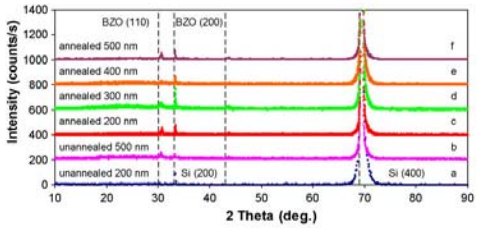

Fig. 2. X-ray diffraction spectra collected from as-deposited and annealed samples: (a) as deposited 200 nm sample, (b) as deposited 500 nm sample; the samples annealed at 800 °C in air for 3 h with film thickness of (c) 200, (d) 300, (e) 400, and (f) 500 nm.

through the Poisson's ratio. These results are also consistent with the presence of the (2 0 0) Si peak, a normally unallowed peak, which appears due to strain in the Si substrate. Another possible reason for the shift of the reflections is the Ba deficiency as indicated in Table 1.

Atomic force microscopy was used to characterize the surface morphology of as deposited and annealed films. Fig. 3 presents AFM micrographs of (a) 200, (b) 300, (c) 400, and (d) 500 nm of Y-doped $BaZrO_3$ samples, annealed at 800 °C in air. AFM micrographs for all films have a similar surface morphology consisting of nano-scale surface particles. The results in Fig. 4 indicate that the particle size increased from 70 nm to 167 nm and the RMS roughness increased from 1.3 nm to 4.2 nm with increased film thickness after annealing, which were generated based on the AFM measurements as depicted in Fig. 3.

According to Fig. 4, as deposited films have a roughness very similar to the Si substrate they were deposited on to. The film roughness and the particle size are increasing with an increased film thickness before and after annealing, however, the significant changes are occurred after the heat treatment.

3.2. Temperature dependence

The sensor conductivity as function of temperature was characterized in the range from 170 °C to 400 °C in order to determine the variation of base line resistance with temperature during humidity measurements and to gain information on potential electrical conduction mechanisms in the material.

The conductivity of the samples increases exponentially with increasing temperature (Fig. 5). This relation can be described as [23,24]:

$$\sigma_t = \sigma_0 \, e^{-E_a/kT} \tag{3.2.1}$$

where σ_t is the conductivity as function of temperature in S/cm, σ_0 is the initial conductivity at 443 K in S/cm, E_a is the activation energy in eV, and k is Boltzmann's constant. Using a first order linear approximation for the slope, a change in activation energy can be observed that could be divided into two distinct regions with different conduction mechanisms. Above ca. 350–370 °C (ca. $1.53\,10^{-3}$ K^{-1}), activation energies between 0.39 eV and 1.71 eV were determined, consistent with literature that suggest that between 400 °C and 650 °C, O^{2-} ion based conduction mechanisms (defect/vacancy hopping) dominate with activation energy values of between 0.3 eV and 1.2 eV [25–27]. Below 350 °C, activation energies of 0.26–0.39 eV were determined, consistent with electron/hole based conduction (0.18–0.39 eV) [28–30].

3.3. Water vapor response

Samples with a Ba-mass concentration above 6% and an O-mass concentration of less than 59% exhibited a strong humidity response. Most solid-state humidity sensors based on chemisorp-

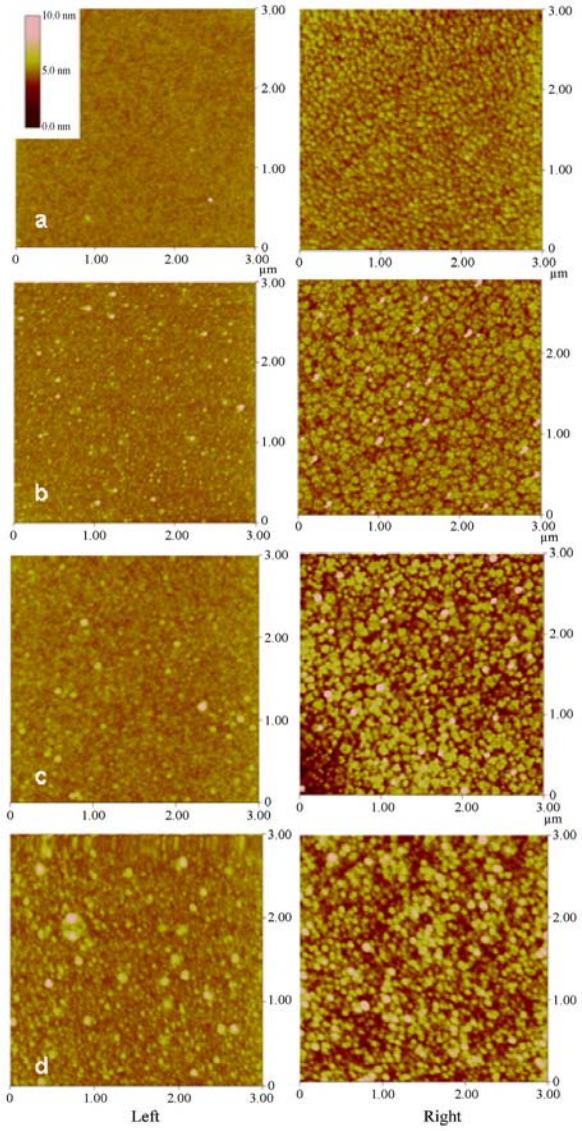

Fig. 3. AFM micrographs of as deposited (left) and annealed (right) samples (a) 200, (b) 300, (c) 400, and (d) 500 nm are annealed in air gas ambient at 800 °C for 3 h. Particle size and RMS roughness increase with increasing film thickness.

tion of H_2O lack selectivity and are not functional at high temperatures [31–34]. Y-doped $BaZrO_3$ can exhibit oxygen vacancies when doped with a lower valence ion e.g., Y^{3+} on the Zr^{4+}. In atmosphere, this material contains oxygen ions, protons, and electrons. The same material when heated in an environment containing H_2O allows the absorption of H_2O into the lattice lowers the oxygen vacancy concentration, and releases protons by the following reaction:

$$BaZr_{(1-x)}Y_xO_{(3-x/2)} + \frac{y}{z}H_2O \rightarrow BaZr_{(1-x)}Y_xH_yO_{(3-x/2+y/2)} \quad \text{where } y < x \tag{3.3.1}$$

With $x = 0.2$ (20% Y-doping; $x/2 = 0.1$ oxygen vacancy concentration), $y > 0$. H_2O molecules dissociate when the water vapor passes

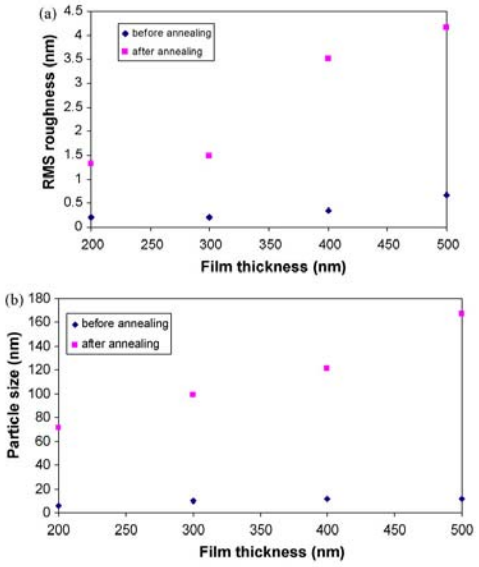

Fig. 4. (a) RMS roughness versus film thickness for Y-doped $BaZrO_3$ for as deposited films and after annealing; (b) particle size versus film thickness for Y-doped $BaZrO_3$ after annealing in air.

the Y-doped $BaZrO_3$ material at high temperature. H_2O molecules will fill in oxygen vacancies, and release protons and electrons each at the anode. H^+ diffuses through the material through reorientation and proton displacement (also called proton hopping) and combines with e^- at the cathode releasing H_2. In addition, O^{2-} ions "hop" through the material and combine with the positive charges at the anode releasing O_2. The mechanism is illustrated in Fig. 6.

Fig. 7(a)–(d) presents conductivity as function of time for 200, 300, 400 and 500 nm thick Y-doped $BaZrO_3$ thin films at 400 °C to a partial pressure of water of 0.058 atm in N_2 carrier gas. The samples are initially exposed to dry N_2 air with corresponding conductivities

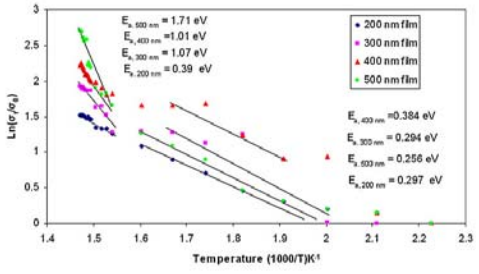

Fig. 5. $\ln(\sigma_t/\sigma_0)$ vs. 1000/T for 200, 300, 400, and 500 nm films between 170 °C and 400 °C in N_2 ambient gas at a flow of 1380 sccm. Activation energies were calculated based on approximate linear fits in the log-plot. Two distinct regions of activation energies are apparent. At temperatures above ca. 350–370 °C (ca. $1.53 \times 10^{-3}\,K^{-1}$) activation energies between 0.39 eV and 1.71 eV were observed. This would be consistent with literature values for O^{2-} ion based conduction mechanisms (vacancy hopping). At temperatures below ca. 350–370 °C activation energies between 0.26 eV and 0.39 eV were observed, consistent with literature values for electron/hole conduction in perovskites.

around 1×10^{-5} S/cm. Then, water vapor is introduced into the test chamber. Once the conductivity has stabilized, the atmosphere was changed back to dry air. As expected, the conductivity increases when exposed to water vapor [35–39].

Film sensitivity is calculated based on:

$$S = \frac{\sigma_t - \sigma_0}{\sigma_0\,\Delta C} \tag{3.3.2}$$

where S is the sensitivity in atm^{-1}, σ_t is the conductivity at different temperature, σ_0 is the initial conductivity, and ΔC is the changing partial pressure of water in atmosphere. Sensitivities are 62 atm^{-1}, 35 atm^{-1}, 27 atm^{-1}, and 22 atm^{-1} with corresponding film thicknesses of 200 nm, 300 nm, 400 nm, and 500 nm.

Sensitivity and conductivity decrease with increasing film thickness (Fig. 8).

The results in Figs. 7 and 8 indicate that absorption of H_2O into the lattice occurs primarily in the surface layers. The base resistance remains unchanged with film thickness while the change of resistance when exposed to humidity decreases with increasing film thickness. This could be modeled by two parallel effective resistors: one for a changing top layer and one for a constant base layer. The sensitivity would thus decrease with increasing film thickness, once the film increases beyond a specific thickness defined by the diffusion depth of the measured gas species. It would stay relatively constant for film thicknesses below the diffusion depth. The protons apparently did not diffuse through the whole film thickness within the given exposure time. Therefore, absorption and ionic surface exchange likely both occurred in this reaction.

3.4. Sensor response time

According to our hypothesis, the dissolution of H_2O into the lattice would lower the oxygen vacancy concentration and release protons into the structure when humidity is applied. The desorption process should follow the reverse of the absorption in response to a decrease of the relative humidity. The response time will depend on the reaction and desorption rates and the residual humidity in the test chamber. We thus anticipate potentially two distinct overlapping processes with individual time constants as can be described as 2nd order time delay response functions (3.4.1) and (3.4.2):

$$\sigma(t) = \sigma_0 + A_1\,e^{-\Delta t/\tau_{1,\mathrm{rise}}} + A_2\,e^{-\Delta t/\tau_{2,\mathrm{rise}}} \tag{3.4.1}$$

$$\sigma(t) = \sigma_0 + A_3\,e^{-\Delta t/\tau_{1,\mathrm{fall}}} + A_4\,e^{-\Delta t/\tau_{2,\mathrm{fall}}} \tag{3.4.2}$$

where σ_0 is the offset, A_1, A_2, A_3, A_4 are coefficients, Δt is the time interval between t_0 (exposure to water vapor or gas) and t_m (time of measurement). $\tau_{1\text{-rise}}$ and $\tau_{2\text{-rise}}$ are the time constants for the absorption of humidity, $\tau_{1\text{-fall}}$ and $\tau_{2\text{-fall}}$ are the time constants for desorption of humidity. Fig. 9 shows the time constants assuming

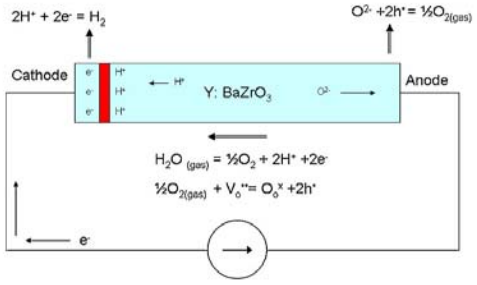

Fig. 6. Conduction mechanism of Y-doped $BaZrO_3$ for humidity sensors.

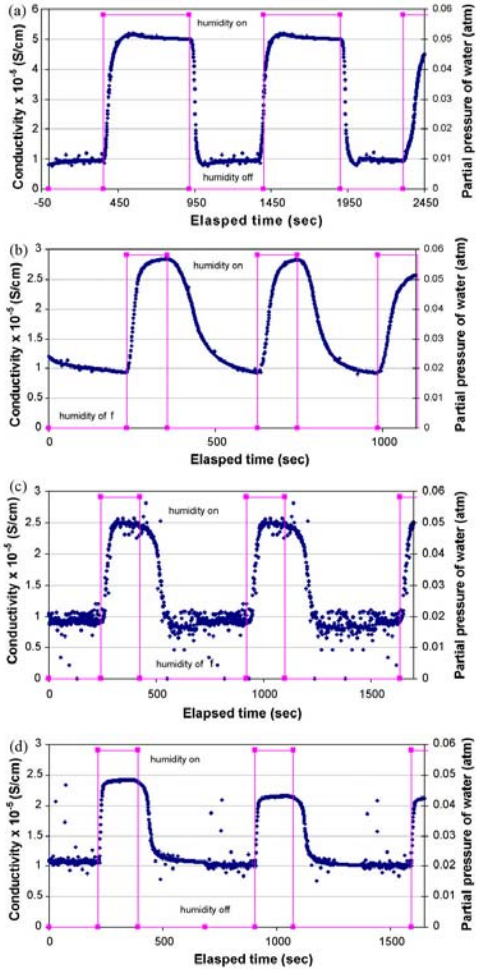

Fig. 7. Humidity response and hysteresis of Y-doped $BaZrO_3$ at partial pressure of water at 0.058 atm (a) 200 nm, (b) 300 nm, (c) 400 nm, and (d) 500 nm at 400 °C.

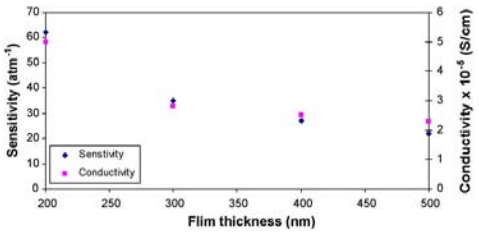

Fig. 8. Humidity sensitivity as function of film thickness for 200, 300, 400, and 500 nm of Y-doped $BaZrO_3$ thin films at 400 °C.

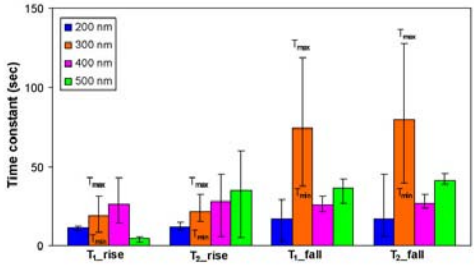

Fig. 9. Second-order model time constant for absorption and desorption process humidity response with maximum, median, and minimum values.

a 2nd order model as described in (3.4.1) and (3.4.2). The figure includes the median, maximum, and minimum time constant in seconds for all samples.

The experimental data shows a clear difference in the time constants for exposure to and removal of humidity from the sensor, i.e. of the absorption and desorption processes. There appears to be a trend towards slower response with increasing layer thickness. A possible explanation for the faster absorption time for 500 nm films is the discontinuity of the film tested in this work, which was caused by mud flat cracking during the annealing process.

3.5. Selectivity

In order to test cross sensitivity or selectivity, the sensitive films were exposed to various test gases that would be present in typical high temperature humidity sensing applications. Fig. 10 presents the response of 400 nm thick Y-doped $BaZrO_3$ to different test gases at 400 °C. N_2 and air were used as carrier gases. NH_3, NO_2, H_2, O_2 and humidity were used as test gases.

No response was observed towards NO_2, NH_3, O_2, and combinations thereof. According to literature, the total film conductivity could increase or decrease depending on ratio of O^{2-} and H^+ conductivity in the sample as a result of the test gases [1,2,40]. In fact, a slight conductivity drop was observed when the combination of H_2 and O_2 was used as tested gas. O^{2-} has lower mobility than H^+. Thus, adding O_2 will potentially fill some of the vacancies and thus reduce the O^{2-} conductivity. Since the O^{2-} conductivity only plays a minor role in determining the total film conductivity below 550 °C, we only expect a small drop in conductivity.

A significant change of conductivity only occurred while water vapor was introduced into the test chamber simultaneously with or without other mixed test gases (NO_2, NH_3, and H_2), indicating that the water vapor response dominates the conductivity change.

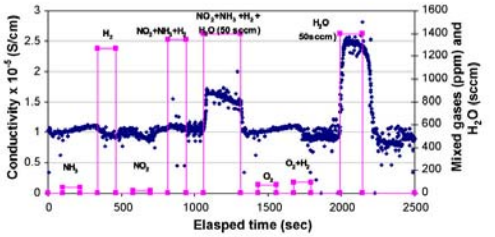

Fig. 10. Cross sensitivity or selectivity measurements for 400 nm Y-doped $BaZrO_3$ towards various test gases, typically present in high temperature humidity sensing applications (NH_3, NO_2, H_2, O_2 and humidity) at 400 °C. Tested gases are: NH_3 (51 ppm), H_2 (1270 ppm), NO_2 (20 ppm), O_2 (75 ppm), and H_2O (50 sccm).

Table 2
Hysteresis of Y-doped $BaZrO_3$ thin film humidity sensors, the maximum hysteresis of the output signal and the baseline signal are with corresponding film thickness of (a) 200, (b) 300, (c) 400, and (d) 500 nm.

	(a)	(b)	(c)	(d)
Max. hysteresis of the baseline signal (%)	3.8	4.1	3.9	7.9
Max. hysteresis of the output signal (%)	5.2	6.1	5.4	7.1

3.6. Hysteresis and stability

The recovery behavior of the sensor is described by the hysteresis, i.e. the change in sensor offset upon continued cycling between zero input and a pre-defined (typically) maximum value. For hysteresis testing, the sensor was cycled between 0 atm and 0.058 atm of partial pressure of water. Table 2 presents the hysteresis of the offset and the maximum output value of the humidity sensors for 6 cycles.

The maximum hysteresis of the maximum output signal for film thicknesses of 200, 300, 400, and 500 nm is in the range of 5–7%, and the offset or baseline maximum hysteresis is between 4% and 8%. The samples principally appear to exhibit stability. A possible explanation for the higher hysteresis value for 500 nm films is the mud flat cracking which caused during the annealing process.

4. Conclusion

Y-doped $BaZrO_3$ thin films were produced using sputtering and evaluated concerning their suitability as thin film sensing materials. The humidity tests indicate satisfactory sensory response and appear to support the originally anticipated, highly selective proton conduction based sensing mechanism. XPS measurements found that the film composition had significantly less Ba content than the nominal target composition, which likely results from a re-sputtering effect. The samples with a Ba-mass concentration above 6% and an O-mass concentration of less than 59% exhibited a strong humidity response. I.e. the sensor response drops the more the stoichiometry varies from $BaZrO_3$ and approaches yttrium zirconia oxide. The results suggest that sputtering has a small process window for use in the fabrication of Y-doped $BaZrO_3$ thin film as a sensing material. The amorphous as deposited films became polycrystalline after annealing at temperatures of 800 °C, but no strong crystallographic texturing was observed. AFM measurements indicate that as deposited films have a roughness very similar to the Si substrate they were deposited on. The RMS roughness (1.3–4.2 nm) and particle size (70–167 nm) increased with increasing film thickness (200–500 nm). The electrical conductivity was characterized using an interdigitated electrode test structure as a function of the partial pressure of water. Partial electrical conductivity due to oxygen ions, holes, and electrons was presented over a temperature range of 170–400 °C. The activation energies were between 0.39 eV and 1.71 eV at high temperatures indicating a possible oxygen ion conduction mechanism, and between 0.26 eV and 0.39 eV at lower temperatures, indicating a possible electron/hole conduction mechanism. This observation appears to be in accordance with data found in literature. Second-order time constants appear to increase with increasing film thickness for both absorption and desorption processes with the exception of 500 nm films. A possible reason for such an exception could be mud flat cracking that may change the rate of diffusion of water into the film, and which may also have an impact on the hysteresis of the humidity sensors.

Acknowledgments

We gratefully acknowledge support through the Department of Energy National Energy Technologies Laboratory NETL through contract no. DE-FC26-05NT42440.

References

[1] W. Wang, A.V. Virkar, Ionic and electron-hole conduction in $BaZr_{0.93}Y_{0.07}O_{3-\delta}$ by 4-probe dc measurements, J. Power Sources 142 (2005) 1–9.
[2] W. Wang, A.V. Virkar, A conductimetric humidity sensor based on proton conducting perovskite oxides, J. Sens. Actuators, B Chem. 98 (2004) 282–290.
[3] H. Schroeder, Make Sense of Sensor Network, Sensor Markets 2008, Intechno Consulting CH (2001).
[4] F. Solzbacher, S. Krueger, Microsystems where are we heading, lead article, Msrnews (2003) 6–10.
[5] N.F. Szabo, H.B. Du, S.A. Akbar, A. Soliman, P.K. Dutta, Microporous zeolite modified yttria stabilized zirconia (YSZ) sensors for nitric oxide (NO) determination in harsh environments, Sens. Actuators, B Chem. 82 (2002) 142–149.
[6] T. Matsui, T. Kosaka, M. Inaba, A. Mineshige, Z. Ogumi, Effects of mixed conduction on the open-circuit voltage of intermediate-temperature SOFCs based on Sm-doped ceria electrolytes, Solid State Ionics 176 (2005) 663–668.
[7] E.D. Bartolomeo, N. Kaabbuathong, A.D. Epifanio, M.L. Grilli, E. Traversa, H. Aono, Y. Sadaoka, Nano-structured perovskite oxide electrodes for planar electrochemical sensors using tape casted YSZ layers, J. Eur. Ceram. Soc. 24 (2004) 1187–1190.
[8] N. Yamazoe, Y. Shimizu, Humidity sensors: principles and applications, Sens. Actuators, B Chem. 10 (1986) 379–398.
[9] B.M. Kulwicki, Humidity sensors, J. Am. Ceram. Soc. 74 (1991) 697–708.
[10] E. Traversa, Ceramic sensors for humidity detection: the state-of-the art and future development, Sens. Actuators, B Chem. 23 (1995) 135–136.
[11] P. Shuk, M. Greenblatt, Solid-state electrolyte film humidity sensor, Solid State Ionics 113–115 (1998) 229–233.
[12] X. Shi, Q. Chen, J. Fang, K. Varahramyan, H. Ji, Al_2O_3-coated microcantilevers for detection of moisture at ppm level, Sens. Actuators, B Chem. 129 (2008) 225–241.
[13] G. Di Francia, A. Castaldo, E. Masserra, I. Nasti, L. Quercia, I. Rea, A very sensitive porous silicon based humidity sensor, Sens. Actuators, B Chem. 111–112 (2005) 135–139.
[14] K. Arshaka, K. Twomey, D. Egan, A ceramic thick film humidity sensor based on MnZn ferrite, Sensors 2 (2002) 50–61.
[15] Y. Sakai, Y. Sadaoka, M. Matsuguchi, Humidity sensors based on polymer thin films, Sens. Actuators, B Chem. 35–36 (1996) 85–90.
[16] H. Iwahara, H. Uchida, S. Tanaka, High temperature type proton conductor based on strontium cerium trioxide and its application to solid electrolyte fuel cells, Solid state Ionics 9–10 (Pt. 2) (1983) 1021–1025.
[17] H. Iwahara, H. Uchida, K. Ogaki, Proton conduction in sintered oxides based on barium cerate, J. Electrochem. Soc. 135 (1988) 529.
[18] H. Iwahara, Proton conduction in sintered oxides and it's application to steam electrolysis for hydrogen production, Solid State Ionics 3–4 (1981) 359.
[19] B. Merinov, C.O. Dorso, W.A. Goddard III, J. Wu, S. Haile, Enhanced power stability for proton conducting solid oxides fuel cells Semi-Annual Progress Report, CIT (2003).
[20] T. Schnellr, T. Schober, Chemical solution deposition prepared dense proton conducting Y-doped $BaZrO_3$ thin films for SOFC sensor devices, Solid State Ionics 164 (2003) 131–136.
[21] X. Chen, M. Sorenson, C. Butler, L. Rieth, M.S. Miller, F. Solzbacher, $BaZrO_3$ thin film for humidity gas sensor, Mater. Res. Soc. Symp. Proc. 1010 (2007).
[22] J. Ho, E. Heifets, B. Merinov, Ab initio simulation of the $BaZrO_3$ (001) surface structure, Surf. Sci. (2006).
[23] T. Ishihara, H. Matsuda, Y. Takita, Doped $LaGaO_3$ perovskite type oxide as a new oxide ionic conductor, J. Am. Chem. Soc. 116 (1994) 3801–3803.
[24] X.Y. Yu, G. Chen, Temperature dependence of thermophysical properties of GaAs/AlAs periodic structure, Appl. Phys. Lett. 67 (1995) 3554.
[25] C.D. Zuo, Doping and defects structure for mix-conducting ceramics for gas separation, Ph.D. dissertation (2006).
[26] J. Wu, Defect chemistry and proton conductivity for Ba-based pervoskites, Ph.D dissertation (2005).
[27] A.S. Nowick, Y. Du, High-temperature protonic conductors with perovskite-related structures, Solid State Ionics 77 (1995) 137.
[28] T. Hibino, A. Hashimoto, M. Suzuki, M. Sano, A soild oxide fuel cell using Y-doped $BaCeO_3$ with with Pd-loaded FeO anode and $Ba_{0.5}Pr_{0.5}CoO_3$ cathod at low temperature, J. Electrochem. Soc. 149 (11) (2002) A 1503–A 1508.
[29] C.W. Tanner, A.V. Virkar, Instability of $BaCeO_3$ in H_2O containing atmospheres, J. Electrochem. Soc. 143 (1996) 1386–1389.
[30] W. Wang, A.V. Virkar, Determination of ionic and electronic conductivities of $Ba_3Ca_{1.18}Nb_{1.82}O_{9-\delta}$ (BCN 18) in dry and wet atmospheres, J. Electrochem. Soc. 151 (10) (2004) 1565–1571.
[31] M. Pecht, A model for moisture induced corrosion failure in microelectronic package IEEE trans, Components Hybrids Manuf. Tech. 13 (2) (1990) 383–389.
[32] N. Tanaka, M. Kitano, T. Kumazawa, A. Nishimura, Evaluating IC-package interface delamination by considering moisture-induced molding-compound swelling, IEEE Trans. Components Package Tech. 22 (3) (1999) 426–432.
[33] T.R. Conrad, R.L. Shook, Impact of moisture/reflow induced delaminations on integrated circuit thermal performance, in: Proceeding of the IEEE Electronic Components and Tech. Conference, New York, NY, USA, 1994, pp. 527–531.
[34] D.U. Kim, M.S. Gong, Thick films of copper-titanate resistive humidity sensor, Sens. Actuators, B Chem. 110 (2005) 321–326.
[35] P.G. Sundell, M.E. Bjoerketurn, G. Wahnstroem, Thermodynamics of doping and vacancy formation in $BaZrO_3$ perovskite oxide form density functional calculations, PRB 73, 104112 (2006).

[36] W. Goepel, Chemical and charge transfer at ionic semiconductor surfaces: implications in designing gas sensor, Prog. Surf. Sci. 20 (1985) 9–103.
[37] K. Kathira, Y. Kohchi, T. Shimura, H. Iwahara, Protonic conduction in Zr-substituted $BaCeO_3$, Solid State Ionics 138 (2000) 91–98.
[38] T. Tsuji, T. Suzuki, H. Iwahara, Electrical conduction in $BaTh_3$ doped with Nd_2O_3, Solid State Ionics 70–71 (1994) 291.
[39] S.C. Roy, G.L. Sharma, M.C. Bhatnagar, S.B. Samanta, Novel ammonia-sensing phenomena in sol-gel derived $Ba_{0.5}Sr_{0.5}TiO_3$ thin films, Sens. Actuators, B Chem. 110 (2005) 299–303.
[40] V. Anil, Virkar, Theoretical analysis of the role of interfaces in transport through oxygen ion and electron conducting membranes, J. Power Sources (2005).

Biographies

Xiaoxin Chen received the BS and ME degrees in the Department of Electrical and Computer Engineering from University of Utah, Salt Lake City, Utah, in 2002 and 2004. She worked as a teaching assistant in University of Utah from 2002 to 2004, and as a research assistant in Chemical Engineering Department at the University of Utah from Jan. 2003 to Aug. 2003. From 2006-current, she is pursuing PhD in ECE Department at the University of Utah. Her research interests include a high temperature humidity microsensors that based on the thin films of electrochemical materials (Y-doped $BaZrO_3$) and system integration.

Loren Rieth received his BS degree in Materials Science from The Johns-Hopkins University, Baltimore, MD, in 1994. He received his PhD in materials science and engineering from the University of Florida, Gainesville, FL, in 2001. From 2001 to 2003, he was a postdoctoral research associate at the University of Utah, Salt Lake City, UT, and continued on at the University of Utah as a research assistant professor in materials science (2003–2005), and electrical and computer engineering (2004-present). His research is focused on deposition and characterization of thin film materials for sensors (chemical, physical, and biological), MEMS, BioMEMS, and energy production.

Mark S. Miller received the BS, in electrical engineering and chemistry from Colorado State University, Fort Collin, CO, in 1985. He received his MS degree in electrical engineering from the Colorado State University. He worked in NCR Microelectronics as an analog integrated Circuit Engineer in 1987, Fort Collins, Colorado. And he received his PhD at the University of California in Santa Barbara in 1993. Then he joined as a postdoctoral research associate in the department of Solid State Physics at the Lund University from 1993 to 1997. From 1997 to 2000, he worked as an assistant professor in the ECE Department at the University of Virginia and started Terahertz Device Corporation. In 2001, he worked as the Director of the Microfabrication Laboratories and an assistant professor in both department of ECE and MSE at the University of Utah. Currently, he is a research associated professor at the University of Utah. His research work is mainly focused on investigating new optical and electrical devices that range from increasing the capacity or function of information technology systems to detecting biochemical molecules to producing new power sources.

Florian Solzbacher received his MSc in electrical engineering from the Technical University Berlin in 1997 and his PhD from the Technical University Ilmenau in 2003. He is Director of the Microsystems Laboratory at the University of Utah and a faculty member in the Departments of Electrical and Computer Engineering, Materials Science and Bioengineering. He is responsible for the Utah branch office of the Fraunhofer IZM, Germany. Dr. Solzbacher is co-founder of First Sensor Technology GmbH, an established supplier to the automotive and process control industry in the USA, Europe and Asia. He is Chairman of the German Association for Sensor Technology AMA. His work focuses on harsh environment microsystems, sensors and materials. He is author of over 60 scientific and engineering publications and book chapters on MEMS devices, technologies and markets for Harsh Environments. Since 2004 he has been Chairman of Sensor + Test, the world's largest international trade fair and ensemble of conferences for sensors, metrology and testing.

CHAPTER 4

PULSED LASER DEPOSITED Y-DOPED $BaZrO_3$ THIN FILMS FOR HIGH TEMPERATURE HUMIDITY SENSORS

Sensors and Actuators B 142 (2009) 166-174

Sensors and Actuators B 142 (2009) 166–174

Contents lists available at ScienceDirect

Sensors and Actuators B: Chemical

journal homepage: www.elsevier.com/locate/snb

Pulsed laser deposited Y-doped $BaZrO_3$ thin films for high temperature humidity sensors

XiaoXin Chen[a,*], Loren Rieth[a], Mark S. Miller[a], Florian Solzbacher[a,b,c]

[a] Department of Electrical Engineering, University of Utah, Salt Lake City, UT, USA
[b] Department of Material Sciences and Engineering, University of Utah, Salt Lake City, UT, USA
[c] Department of Bioengineering, University of Utah, Salt Lake City, UT, USA

ARTICLE INFO

Article history:
Received 17 April 2009
Received in revised form 30 June 2009
Accepted 27 July 2009
Available online 3 August 2009

Keywords:
Thin film
Microsensor
Humidity
High temperature
Y-doped $BaZrO_3$ material
Physical vapor deposition (PVD)
Ionic conductor

ABSTRACT

Pulsed laser deposited (PLD) Y-doped $BaZrO_3$ thin films ($BaZr_{1-x}Y_xO_{3-y/2}$, $x = 0.2$, $y > 0$), were investigated as to their viability for reliable humidity microsensors with long-term stability at high operating temperatures ($T > 500\,^{\circ}C$) as required for in situ point of source emissions control as used in power plant combustion processes. Defect chemistry based models and initial experimental results in recent humidity sensor literature [1,2], indicate that bulk Y-doped $BaZrO_3$ could be suitable for use in highly selective, high temperature compatible humidity sensors. In order to accomplish faster response and leverage low cost batch microfabrication technologies we have developed thin film deposition processes, characterized layer properties, fabricated and tested high temperature humidity micro sensors using these thin films. Previously published results on sputtering Y-doped $BaZrO_3$ thin films have confirmed the principle validity of our approach [3]. However, the difficulty in controlling the stoichiometry of the films and their electrical properties as well as mud flat cracking of the films occurring either at films thicker than 400 nm or at annealing temperature above 800 °C have rendered sputtering a difficult process for the fabrication of reproducible and reliable thin film high temperature humidity microsensors, leading to the evaluation of PLD as alternative deposition method for these films.

X-ray Photoelectron Spectroscopy (XPS) data was collected from as deposited samples at the sample surface as well as after 4 min of Ar^+ etching. PLD samples were close to the desired stoichiometry. X-ray diffraction (XRD) spectra from all as deposited $BaZrO_3$:Y films show that the material is polycrystalline when deposited at substrate temperatures of 800 °C. AFM results revealed that PLD samples have a particle size between 32 nm and 72 nm and root mean square (RMS) roughness between 0.2 nm and 1.2 nm. The film conductivity increases as a function of temperature (from 200 °C to 650 °C) and upon exposure to a humid atmosphere, supporting our hypothesis of a proton conduction based conduction and sensing mechanism. Humidity measurements are presented for 200–500 nm thick films from 500 °C to 650 °C at vapor pressures of between 0.05 and 0.5 atm, with 0.03–2% error in repeatability and 1.2–15.7% error in hysteresis during cycling for over 2 h. Sensitivities of up to 7.5 atm^{-1} for 200 nm thick PLD samples at 0.058 atm partial pressure of water were measured.

1. Introduction

Power generation using fossil fuels generally involves high temperature and high pressure. Associated with any type of power generation using fossil fuels is formation of some gaseous species, such as H_2O, CO, CO_2, NH_3, H_2, etc. Today, there is no single mechanism, material, or operating mode will be fit to provide the requirements of the restrictions on emissions from fossil fuel fired power plants and internal combustion engines [4]. Microscale (MEMS) gas sensing devices are being developed to help monitor emissions and provide feedback for advanced engine controls and emission control devices. In order to help accurately measure the concentrations of all gaseous species present in the exhaust gas, the reliable measurement of water vapor partial pressure that is produced in the combustion process is necessary. In addition, water vapor can influence the measurement of Combustion exhaust gas when using, e.g. metal oxide sensors such as In_2O_3 at a high operating temperatures ($T > 200\,^{\circ}C$), [5].

Several humidity sensors based on surface adsorption of water vapor (H_2O) have been reported [6–9]. These humidity sensors lack selectivity towards NO_x and O_2, as well as typically featuring low operating temperature ranges of between 20 °C and 95 °C making them unsuitable for the use in exhaust gas streams [10–13]. An alternative sensing mechanism based on absorption of H_2O into

* Corresponding author. Tel.: +1 8016714407.
E-mail address: Xiao_C@yahoo.com (X. Chen).

0925-4005/$ – see front matter © 2009 Elsevier B.V. All rights reserved.
doi:10.1016/j.snb.2009.07.041

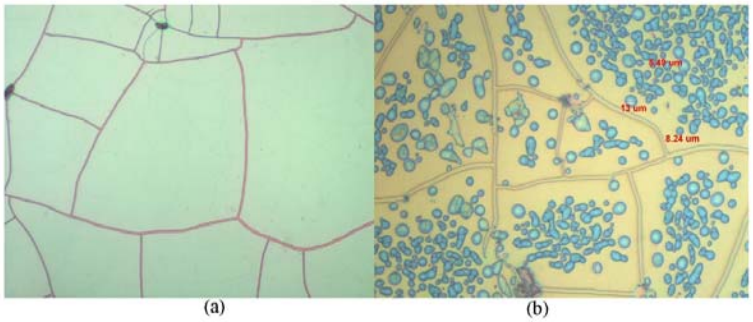

Fig. 1. Microscopy 6× pictures of cracked sputtered thin film with a film thickness of 400 nm (a) annealed at 800 °C in air for 3 h and (b) annealed at 1000 °C in air for 3 h.

the lattice, provides better selectivity since only selected species present in the combustion gas readily dissolve into the solid lattice [3]. $BaZrO_3$ is a ceramic material with Perovskite structure that has been reported to have high chemical stability at high operating temperatures (i.e. it does not (permanently) change its basic chemical composition and structure, when exposed to other gaseous species) and high proton conductivity when doped appropriately [14–15]. When doped with a lower valent ion on the Zr-site, the material contains oxygen vacancies and can exhibit oxygen ion conductivity [1]. The material can also feature *p*-type electronic conductivity in atmospheres with high oxygen partial pressure [1]. At temperatures $T > 500\,^{\circ}C$, H_2O dissolves into the lattice thus "filling in" the oxygen vacancies and releasing protons into the structure. Such defect chemistry allows a repeatable, selective, and sensitive sensing mechanism [16–20]. By fabricating and testing high temperature humidity micro sensors using thin films we could not only significantly reduce response time, but also allow for low cost fabrication, which would allow transfer of the technology into higher volume markets, such as, e.g. automotive and combustion engine management.

Previously published results on sputtered Y-doped $BaZrO_3$ thin films have confirmed the principle validity of our approach [3]. However (1) the difficulty in controlling the stoichiometry of the films and their electrical properties as well as (2) mud flat cracking of the films (Fig. 1) occurring at films thicker than 400 nm or when annealing at temperatures above 800 °C have rendered sputtering a difficult process for the use in reproducible and reliable fabrication of thin film humidity microsensors for operating temperatures above 500 °C.

This work presents pulsed laser deposition (PLD) as alternative high temperature deposition method for Y-doped $BaZrO_3$ thin films, allowing the potential mitigation of the above stated drawbacks of sputtered films problems while maintaining the advantageous humidity sensing characteristics of the films.

2. Experimental methods

Y-doped $BaZrO_3$ of 200, 300, 400, and 500 nm thin films were deposited onto oxidized 2″ *n*-type (1 0 0) silicon substrates using PLD at substrate temperatures of 800 °C in a vacuum ambient with base pressure at 8.5×10^{-7} Torr. Films were characterized using X-Ray Photoelectron Spectroscopy (XPS), X-Ray Diffraction (XRD), and Atomic Force Microscopy (AFM), to determine film composition, microstructure, and surface morphology. Electrical conductivity as function of temperature and water vapor humidity sensing characteristics of the films were measured using a custom-built gas sensor test station that up to 650 °C. Silicon based gas sensor test structures with Cr (20 nm) and Au (180 nm) thin film metallization deposited on top of the sensing material were fabricated for humidity tests as previously published [3]. The size of each sensor is $7 \times 7\,mm^2$. It uses 10 pairs of interdigitated electrodes (IDE) spaced 100 μm apart and includes a resistive thin film heater, a resistive temperature device (RTD), and the sensitive layer.

2.1. Characterization of film composition and structure

The electroceramic thin films were deposited by pulsed-laser deposition from a 1″ diameter, 99.9% pure ceramic $BaZr_{0.8}Y_{0.2}O_{2.9}$ pure ceramic target purchased from Process Materials Inc. The chemical composition of the target was studied with X-ray fluorescence (XRF) by Evans Analytical Group (EAG) exhibiting a larger Y concentration (7%) than expected (4%). The films were deposited on oxidized 2″ *n*-type (1 0 0) silicon substrates at 800 °C substrate temperature and a base pressure of 8.5×10^{-7} Torr in a PVD products Inc system. The films were grown at 50 Hz, 250 mJ/pulse laser energy with average energy flux of $1\,J/cm^2$, yielding a film thickness uniformity of ±10%. Films with a center thickness of 200, 300, 400, and 500 nm were deposited. Since the PLD process only allows for limited area of uniform thickness, the center thickness constitutes the target film thickness. Towards the edge of the substrate the film thickness can drop by 16–22%. Thicknesses were verified using a Woolam V-Vase spectroscopic ellipsometer. X-ray photoelectron spectroscopy (XPS) measurements were made using a Kratos Axis ULTRA^{DLD} system using monochromatic Al Kα radiation. Composition data was recorded for as received samples and after 4 min of Ar^+ ion beam etching. X-ray diffraction (XRD) measurements were made using a Philips X'Pert system using Cu Kα radiation in the Bragg-Brentano geometry for 2θ angles from 10–90°. Atomic force microscopy (AFM) micrographs were collected with a Veeco Dimension 3000 system using etched Si tapping mode tips with a nominal tip radius of ~5 nm.

2.2. Water vapor sensitivity measurements

The water vapor sensing characteristics for PLD $BaZrO_3$:Y thin films were measured using a custom-built gas sensor test station. Sample chips were placed on a hotplate in a stainless steel chamber and contacted with probe needles attached to a PC/labview controlled Keithley digital multimeter in voltage measurement mode. N_2 carrier gas at 200 sccm was passed through a water bubbler at 80 °C, saturating the gas at 0.468 atm water vapor pressure. N_2 as opposed to compressed air was chosen as carrier gas for this initial set of experiments, in order to (1) establish the baseline characteristics for the sensitive layer without impact from potential chemical

Table 1
Film composition quantified by XPS measurements for samples as function of thickness for (a) nominal composition, and deposited at 800 °C with film thickness of (b) 200 nm (c) 300 nm (d) 400 nm, and (e) 500 nm.

Sample name	a	b		c		d		e	
	AT conc (%)	AT conc (%) as received	AT conc (%) after 4 min Ar^+ etching	AT conc (%) as received	AT conc (%) after 4 min Ar^+ etching	AT conc (%) as received	AT conc (%) after 4 min Ar^+ etching	AT conc (%) as received	AT conc (%) after 4 min Ar^+ etching
Ba 3d	20	10	14	9	13	8	14	11	14
O 1s	60	52	58	52	60	54	61	47	58
Zr 3p	16	9	18	13	19	16	19	12	19
Y 3p	4	6	9	7	6	4	4	4	8
C 1s	0	23	1	19	2	18	2	26	1

reactions with air oxygen, (2) to allow comparability with previous measurements using sputtered $BaZrO_3$:Y thin films and (3) for cost considerations during the initial screening. A more realistic scenario going forward is the measurement using compressed air. Before the saturated water vapor reaches the test chamber, it is diluted with N_2 gas (0 sccm, 203 sccm, 606 sccm, and 1380 sccm, allowing variation of humidity/water vapor partial pressure). Once the test gas enters the test chamber it is heated to the sensor operating temperature (leading to a reduced relative humidity). The partial pressures of water vapor are calculated by the percentage of total gas flow in 1 atmosphere.

Sample resistance values were determined based on the voltage measurements using a 0.07 μA supply current that would not lead to self heating of the film. The temperature dependence of resistance was measured at 200–650 °C. The response to water vapor was measured at 0.058 atm, 0.116 atm, 0.232 atm, and 0.468 atm partial pressure of water at 500 °C to 650 °C. The film conductivity was determined using:

$$\sigma = \frac{L}{RAn} \quad (1)$$

where σ is the film conductivity ($[\sigma] = 1$ S/cm), R is the measured resistance ($[R] = 1$ MΩ), A is the cross sectional area of the sample ($[A] = 1$ cm^2), L is the distance between each interdigitated electrode ($[L] = 1$ cm), and n is the number of interdigital electrode pairs ($n = 10$).

3. Results and discussion

3.1. Film characterization

The chemical composition of the films was measured by XPS from as received samples, and after ion beam etching. The film compositions were quantified from the spectra and are summarized in Table 1. XPS data indicates that the film composition is close to the nominal target composition in the bulk of the film (i.e. after etching). We are only providing data after 4 min of Ar^+ etching, since no significant changes in film composition were observed in any of the films for longer etch times. The films were however found to be Ba deficient in all cases, and were also often richer in Y which correlates with the XRF data from the target.

XRD spectra were collected to investigate the microstructure of the deposited films, and are presented in Fig. 2. The spectra are for as deposited PLD samples with substrate temperature of 800 °C. The film thickness is (a) 200, (b) 300, (c) 400, and (d) 500 nm. The $BaZrO_3$ reflections were present in the spectra (a) to (d) indicating the films were polycrystalline in character. The dashed vertical lines on the plots represent the JCPDS values for $BaZrO_3$ with strong reflections for both (1 1 0) and (2 1 1) $BaZrO_3$. These reflections are shifted to higher 2θ values compared to the JCPDS database, which would be consistent with the films being under tensile stress. These results are also consistent with the presence of the (2 0 0) Si peak, a normally unallowed peak, which appears due to strain in the Si substrate.

The peak heights of BZO (1 1 0) and BZO (2 1 1) reflections were increased with increasing film thickness. A Philips X'Pert data col-

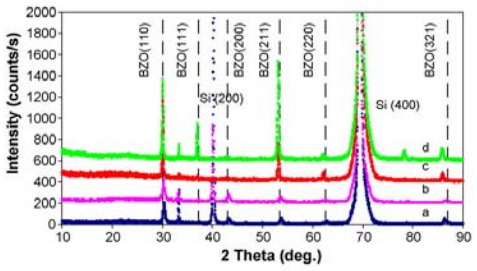

Fig. 2. X-ray diffraction spectra collected from as deposited PLD samples at a base pressure of 8.5×10^{-7} Torr with substrate temperatures at 800 °C and thicknesses of: (a) 200, (b) 300, (c) 400, (d) 500 nm.

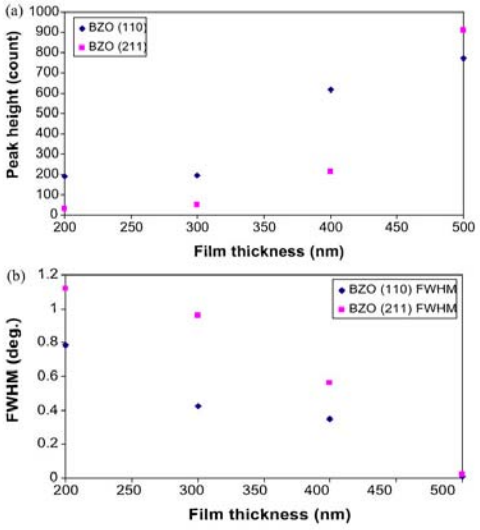

Fig. 3. (a) Peak height versus film thickness for Y-doped $BaZrO_3$ PLD films with substrate temperature of 800 °C, and (b) full width at half maximum (FWHM) versus film thickness for PLD films with substrate temperature of 800 °C.

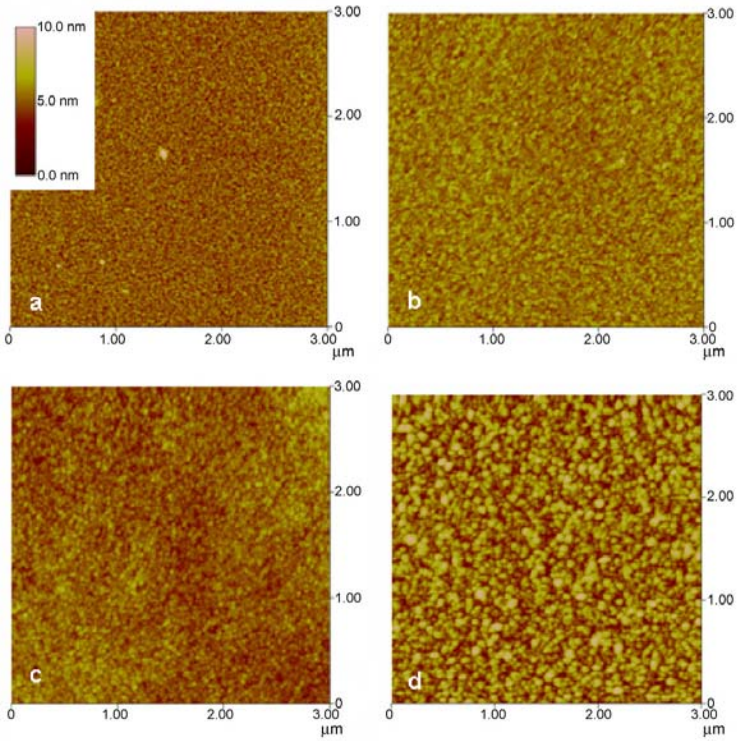

Fig. 4. AFM micrographs of as deposited PLD samples with substrate temperature of 800 °C. (a) 200, (b) 300, (c) 400, and (d) 500 nm. Particle size and root mean square (RMS) roughness increase with increasing film thickness.

lector was used to measure the full width half max (FWHM) values of these reflections which are decreasing with increasing film thickness (Fig. 3). This is consistent with both a thinner film and a decrease in crystal quality of the film, which the decrease could also caused by damage in the crystal, e.g. because of expanding grain size. The relative contributions of each mechanism could however not be distinguished.

AFM was used to characterize the surface morphology of as deposited PLD films. Fig. 4 presents AFM micrographs of (a) 200, (b) 300, (c) 400, and d. 500 nm of Y-doped $BaZrO_3$ PLD samples with substrate temperature of 800 °C in vacuum. AFM micrographs for all samples have a similar surface morphology consisting of nano-scale surface particles. For each film thickness, 6 individual measurements were made and averaged. The results in Fig. 5 indicate that RMS roughness increased from 0.2 nm to 1.2 nm with increased film thickness and particle size increased from 32 nm to 72 nm, using a stereological technique.

The data presented in Fig. 5 indicates the PLD films have a very fine particle size and smooth surface. The film roughness and the particle size are increasing with increased film thickness.

3.2. Temperature dependence

The sensor conductivity as function of temperature was characterized from 200 to 650 °C to determine the variation of base line resistance with temperature during humidity measurements and to gain information on potential electrical conduction mechanisms in the material.

The conductivity of the samples increases exponentially with increasing temperature (Fig. 6). This relation can be described as [21–22]:

$$\sigma_t = \sigma_0 e^{-E_a/kT} \quad (2)$$

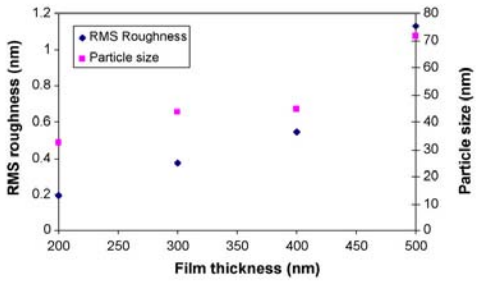

Fig. 5. RMS roughness and particle size versus film thickness for Y-doped $BaZrO_3$ for as deposited PLD films with substrate temperature of 800 °C.

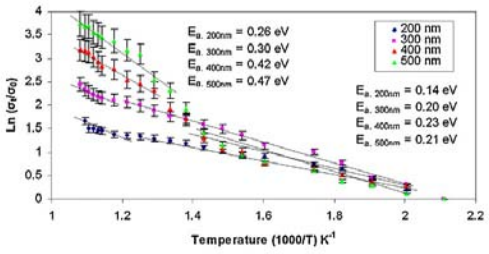

Fig. 6. $\ln(\sigma_t/\sigma_0)$ versus $1000/T$ for 200, 300, 400, and 500 nm films between 200 °C and 650 °C in N_2 ambient gas at a flow of 1380 sccm. Activation energies were calculated based on approximate linear fits in the log-plot. Two distinct regions of activation energies are apparent. At temperatures above ca. 500–650 °C (ca. $1.29\,10^{-3}\,K^{-1}$) activation energies between 0.26 and 0.47 eV were observed. This would be consistent with literature values for O^{2-} ion based conduction mechanisms (vacancy hopping). At temperatures below ca. 500 °C activation energies between 0.14 and 0.23 eV were observed, consistent with literature values for hole conduction in perovskites.

where σ_t is the conductivity as function of temperature in S/cm, σ_0 is the initial conductivity at 473.15 K in S/cm, E_a is the activation energy in eV, and k is Boltzmann's constant at 8.617385×10^{-5} eV/K. Using a first order linear approximation for the slope, a change in activation energy can be observed that could be divided into two distinct regions with different conduction mechanisms with an error bar of between 3.2% and 7.6%. Above ca. 500–650 °C (ca. $1.29\,10^{-3}\,K^{-1}$), activation energies between 0.26 and 0.47 eV were determined, consistent with literature that suggest that between 500 °C and 650 °C, O^{2-} ion based conduction mechanisms (defect/vacancy hopping) dominate with activation energy values of between 0.3 and 1.2 eV [23]. Below 500 °C, activation energies of 0.14–0.23 eV were determined, consistent with electron/hole based conduction (0.18–0.39 eV) [24].

After 2 h of stabilizing, the baseline resistances settled at approximately 13.7 MΩ, 8.9 MΩ, 6.8 MΩ, and 5.6 MΩ (corresponding film thicknesses: 200, 300, 400, and 500 nm) at an operation temperature of 500 °C. Resistances of 4.1 MΩ, 2.5 MΩ, 1.9 MΩ, and 1.2 MΩ (corresponding film thickness of 200, 300, 400, and 500 nm) were measured at 650 °C operation temperature (Fig. 7) indicating that the specific resistance remained unaffected by the layer thickness. The slight nonlinearity of the film resistance as function of thickness towards thinner films could potentially be explained by the Fuchs–Sondheimer theory of conduction in thin films that described an increase in specific resistance with decreasing film thickness due to increasing impact of charge carrier scattering on

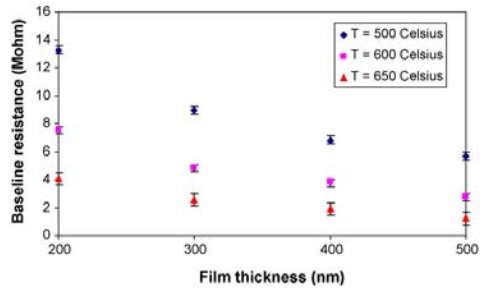

Fig. 7. The baseline resistances of 200, 300, 400, and 500 nm PLD film at 500 °C, 600 °C, and 650 °C.

surface/interfaces of the film in relation to bulk film conduction. The corresponding temperature coefficients of resistance (TCRs) are slightly increasing with thickness ($1.9 \times 10^{-3}\,K^{-1}$, $2.03 \times 10^{-3}\,K^{-1}$, $2.06 \times 10^{-3}\,K^{-1}$, and $2.14 \times 10^{-3}\,K^{-1}$).

3.3. Water vapor response

As discussed in a previous publication [3], Y-doped $BaZrO_3$ can exhibit oxygen vacancies when doped with a lower valence ion, e.g. Y^{3+} on the Zr^{4+} sites. In atmosphere, this material contains oxygen ions, and holes. The same material when heated in an environment containing H_2O allows the absorption of H_2O into the lattice which lowers the oxygen vacancy concentration, and releases protons. A possible reaction path for this process would be:

$$H_2O_{(gas)} + V_o^{\bullet\bullet} \leftrightarrow O_o^{x} + 2H^{\bullet} \quad (3)$$

H_2O molecules dissociate when the water vapor passes the Y-doped $BaZrO_3$ material at high temperature. H_2O molecules will fill in oxygen vacancies, and release protons and electrons. Protons diffuse through the material through reorientation and proton displacement (also called proton hopping) and combine with electrons releasing H_2. In addition, oxygen ions can "hop" through the material and combine with holes releasing O_2.

All samples are initially exposed to dry N_2. Then, water vapor is introduced into the test chamber. Once the electrical conductivity has stabilized, the atmosphere is changed back to dry N_2. As expected, based on the model and reaction described above the conductivity increases when exposed to water vapor [1–3]. The samples were measured at various partial pressures of water (0.058 atm, 0.116 atm, 0.232 atm, and 0.464 atm) at the temperature of 500 °C, 600 °C, and 650 °C.

Film sensitivity as stated below is calculated based on:

$$S = \frac{(\sigma_t - \sigma_0)}{(\sigma_0 * \Delta C)} \quad (4)$$

where S is the sensitivity in atm^{-1}, σ_t is the conductivity upon exposure to humidity atoperating temperature, σ_0 is the initial offset or baseline conductivity in dry N_2 at the same operating temperature. ΔC is the change in partial pressure of water in atmospheres. Fig. 8(a) and (b) illustrate the sensor response, i.e. the conductivity as function of time for a 200 nm film at 500 °C and 650 °C to 0.058 atm partial pressure of water vapor in N_2 carrier gas. Sensitivities up to 7.5 atm^{-1} were measured at 500 °C. The data presented in Fig. 9 shows that sensitivity decreases with increasing film thickness and increasing partial pressure of water at 500 °C, 600 °C, and 650 °C.

The reduction in sensitivity with increasing film thickness (Fig. 9) indicates that absorption of H_2O into the lattice occurs primarily in the surface layers. This could be modeled by two parallel effective resistors: one for a changing top layer and one for a constant base layer. The sensitivity would thus decrease with increasing film thickness, once the film increases beyond a specific thickness defined by the diffusion depth of the measured gas species. It would stay relatively constant for film thicknesses below the diffusion depth. The protons apparently did not diffuse through the whole film thickness within the given exposure time. Therefore, both absorption and ionic surface exchange likely both occurred in this reaction.

3.4. Sensor response time

According to our hypothesis, the dissolution of H_2O into the lattice would lower the oxygen vacancy concentration and release protons into the structure when humidity is applied. The desorption process upon decrease of water vapor pressure or relative humidity should follow the inverse of the absorption. The response

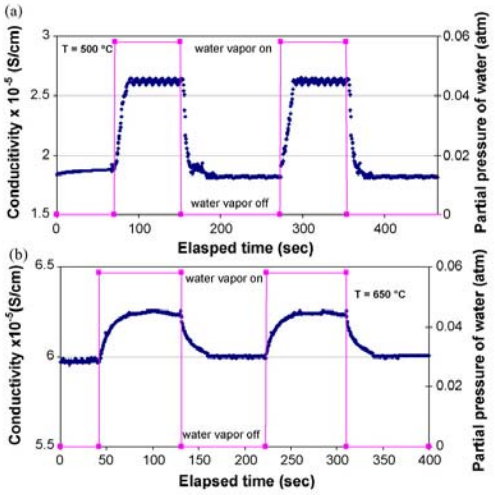

Fig. 8. Water vapor response of Y-doped $BaZrO_3$ PLD thin films at a partial pressure of water at 0.058 atm (a) 200 nm at 500 °C, and (b) 200 nm at 650 °C.

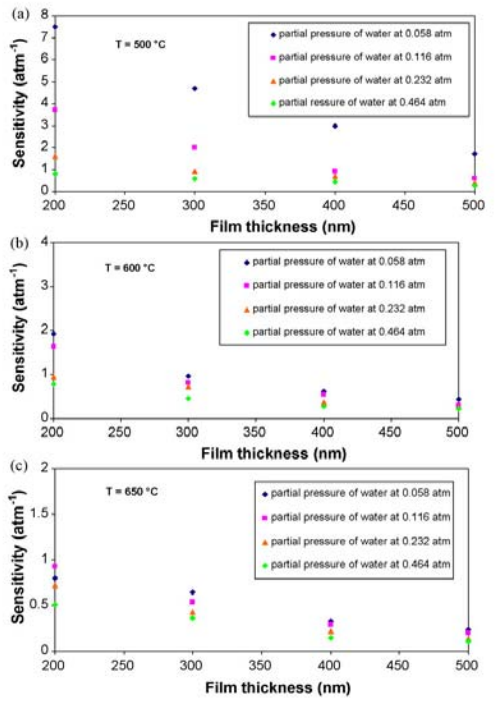

Fig. 9. Water vapor sensitivity as function of film thickness for 200, 300, 400, and 500 nm of Y-doped $BaZrO_3$ PLD thin films in various partial pressure of water at (a) 500 °C, (b) 600 °C, and (c) 650 °C.

time will depend on the reaction and desorption rates and the residual humidity in the test chamber. The time constants for gas exchange t_e and adsorption or desorption of humidity in the test chamber $t_{a,d}$ are of the order of 2.4 s, which clearly below the response times of the layers and can be ignored in this experiment. We thus anticipate potentially two distinct overlapping processes with individual time constants as can be described as 2nd order time delay response functions (5) and (6) below:

$$\sigma(t) = \sigma_0 + A_1 e^{-\Delta t/\tau_{1,\text{rise}}} + A_2 e^{-\Delta t/\tau_{2,\text{rise}}} \quad (5)$$

$$\sigma(t) = \sigma_0 + A_3 e^{-\Delta t/\tau_{1,\text{fall}}} + A_4 e^{-\Delta t/\tau_{2,\text{fall}}} \quad (6)$$

where σ_0 is the offset, A_1, A_2, A_3, A_4 are coefficients, Δt is the time interval between t_0 (exposure to water vapor or gas) and t_m (time of measurement), $\tau_{1,\text{rise}}$ and $\tau_{2,\text{rise}}$ are the time constants for the absorption of humidity, $\tau_{1,\text{fall}}$ and $\tau_{2,\text{fall}}$ are the time constants for desorption of humidity. Fig. 8 shows the time constants assuming a 2nd order model as described in (5) and (6) above. The figure includes the median, maximum, and minimum time constant in seconds for 200 nm samples at 500 °C, 600 °C, and 650 °C (Fig. 10).

The experimental data shows an increase in time constant with increase in water vapor pressure and an overall decrease in time constants across the entire measured temperature range. Fall times

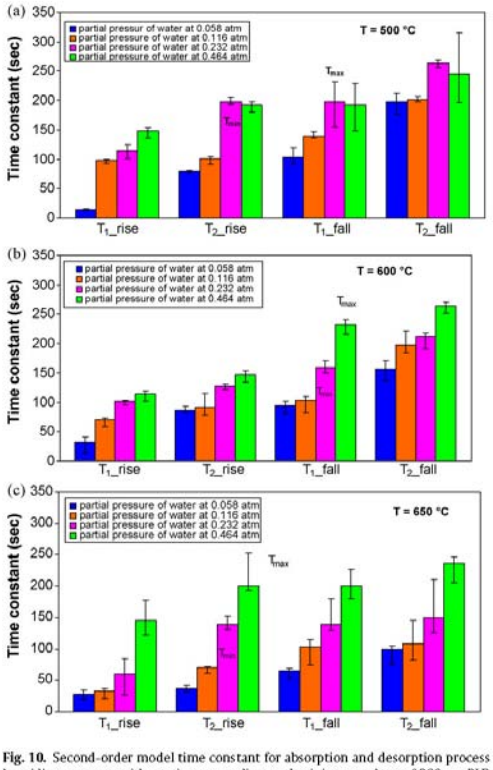

Fig. 10. Second-order model time constant for absorption and desorption process humidity response with maximum, median, and minimum values of 200 nm PLD film at partial pressure of water of 0.058 atm, 0.116 atm, 0.232 atm, and 0.464 atm at operating temperatures of (a) 500 °C, (b) 600 °C, and (c) 650 °C.

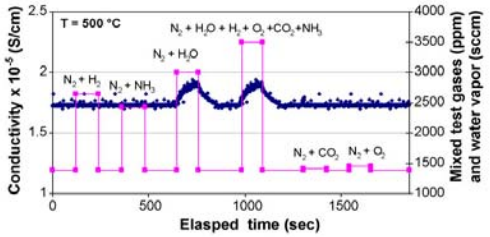

Fig. 11. Cross sensitivity or selectivity measurements of 500 nm Y-doped $BaZrO_3$ PLD film towards various test gases (NH_3, H_2, O_2, CO_2, and water vapor) at 500 °C. The gases concentrations are: NH_3 (50 ppm), H_2 (1270 ppm), O_2 (75 ppm), CO_2 (25 ppm), and water vapor (200 sccm).

are larger than rise times, indication a slower removal than absorption of water vapor. At 500 °C and high concentrations of water vapor, desorbtion times are again decreasing, while the distribution of time constants increases. A possible explanation for this response may be that the sensor is running into saturation at these comparably lower temperatures. The faster response with increasing of temperature could be correlated with the higher activation energy provided by the increase in temperature. There appears a trend towards slower response with increasing film thickness. Further investigations will be required to determine the correlation between partial pressure of water and time constant, and the relation between the film thickness and sensor response time.

3.5. Selectivity

All PLD samples were exposed to various test gases to test cross sensitivity or selectivity of Y-doped $BaZrO_3$ thin films in typical combustion exhaust gas environments. Fig. 11 presents the gas response of 500 nm PLD film to different gas speices at 500 °C. N_2 gas were used as carrier gas in all measurements. NH_3, H_2, O_2, CO_2, and water vapor were used as test gases that typical appear in high temperature sensing applications.

Sample appear very stable in each tested gas as well as test gas combinations. There is no significant change of conductivity (1% drop) while water vapor was introduced into the test chamber simultaneously with or without mixed tested gases, which indicating that the sensitivity response was dominated by water vapor. The small amount of conductivity change could simply cause by the stability of the sensor itself.

3.6. Hysteresis and stability

Hysteresis is defined as the change in sensor offset upon continued cycling between zero and a target or maximum input and subsequently a corresponding minimum (=offset) and target or maximum output value. For hysteresis testing, the sensor was cycled between 0 and of the four target partial pressures of water at 500 °C. Table 2 below presents the hysteresis of the offset and the maximum output value of the humidity sensors for 6 cycles at the initial test for 200 nm thicker film.

The maximum hysteresis of the maximum output signal for film thicknesses of 200 nm is in the range of 1.6–7.9%, and the offset or baseline maximum hysteresis is between 1.2 and 15.7%. The samples principally appear to exhibit stability. A possible explanation for the higher hysteresis value at 650 °C could be that these measurements are closer to the original film and substrate deposition temperature (800 °C) leading to the onset of permanent material changes due to temperature. At higher temperatures, we are anticipating a predominant oxygen ion based conductivity mechanism that leads to temperature and oxygen partial pressure dependent changes in composition (i.e. oxygen vacancy concentration). Since at higher temperatures, the film conductivity is largely determined by this conduction mechanism a change in oxygen vacancy concentration will likely have a larger effect on the base or offset resistance upon removal of the water vapor than at lower temperatures, where (a) we are less likely to see permanent changes in the material and b) conductivity relies more heavily on hole conductivity. Hence changes in the contribution of oxygen vacancy hopping to the overall conductivity would affect the overall resistivity less than at higher temperatures.

The shelf-time of the sensors is correlated with the stability of the sensors. After testing the PLD humidity sensors, we placed all samples into a gel-pac box at room temperature in the microfabrication clean room. While this test does not truly represent real life conditions, in which the sensor will likely be stored in a regular storage closet or open shelf, this kind of storage still represents a reasonable approximation to typical ensured that the samples could be locked away in a controlled and reproducible environment in between measurements, which simplifies comparison of results. For stability testing, the sensors were re-tested under identical experimental conditions each time. First, we placed the sensors into the test chamber while exposing them to dry N_2 gas at 1380 sccm until 500 °C for 2 h to stabilize the initial offset conductivity. Then water vapor is introduced into the test chamber at between 0 and 0.058 atm of partial pressure of water. Once the conductivity has stabilized, the atmosphere is changed back to dry N_2. Fig. 9 below presents the stability of the 200 nm PLD humidity sensor over a period of 52 weeks with the corresponding film base (or offset) resistivity.

The stability data clearly shows that the humidity sensor ages over time (Fig. 12). The small (2.3%) change (from 56.4 to 54.9 kΩ cm) in base resistance compared to the 35% drop (from 7.5 to 4.8 atm^{-1}) in sensitivity could be attributed to a point defect density change in the material over time that does not impact the overall conductivity of the material, but impacts the sensing mechanism. No settling of the drop in sensitivity can be observed (i.e. burn in) indicating that the sensitivity will eventually reach zero at which point the sensor would be useless. We will continue to monitor the sensor performance. Future measurements of the film composition at the end of the long term test may yield information about the potential extent of the change in defect con-

Table 2
Hysteresis of 200 nm PLD Y-doped $BaZrO_3$ thin film humidity sensors, the maximum hysteresis of the output signal and the baseline signal are with corresponding temperature 500 °C, 600 °C, and 650 °C at partial pressure of water at 0.058 atm, 0.116 atm, 0.232 atm, and 0.464 atm.

Partial pressure of water (atm)	T = 500 °C		T = 600 °C		T = 650 °C	
	Max. hysteresis of the baseline signal (%)	Max. hysteresis of the output signal (%)	Max. hysteresis of the baseline signal (%)	Max. hysteresis of the output signal (%)	Max. hysteresis of the baseline signal (%)	Max. hysteresis of the output signal (%)
0.058	2.8	4.3	3	1.3	15.7	6
0.116	1.8	1.6	1.6	2.2	3.1	5.1
0.232	1.2	3.1	2.4	3.2	2.5	4.1
0.464	2	5.3	1.7	2.1	4.1	7.9

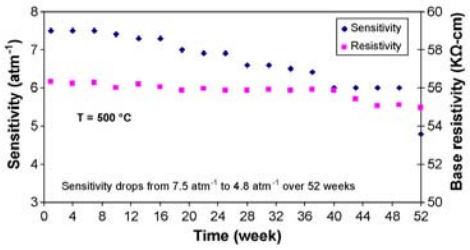

Fig. 12. The stability test of the PLD humidity sensors of 200 nm film during 52 weeks, the sensitivity range drops from 7.5 atm^{-1} to 4.8 atm^{-1} with the corresponding base resistivity at 500 °C when partial pressure of water at 0.058 atm. The base resistivity (i.e. at 0 atm water vapor) of the sample drops, but remains comparably stable.

centration or film composition which could explain the sensitivity drop.

A single sample would not provide a reliable data point. In fact, we have measured a number of samples at different temperatures, partial pressures and varying cycles. We have just started generating a growing body of long term data and wanted to show an example of preliminary stability data that provides evidence that the sensors can last very long and outperform other devices presented in literature. From a review of our existing data from several devices, sensors developed with this process could be categorized into two categories: either they fail immediately (no signal at all or failure after one or two cycles) or they behave stable as presented above. More extensive long term stability data will be presented in a new publication comparing PLD and sputtered films that is currently in preparation.

Considering the harsh testing conditions and high temperatures for this sensor, more than one year time of operation with very stable base resistance can however be considered a major milestone for a sensor developed in a university setting. Using regular re-calibration routines, the sensor could be used in an industrial setting.

4. Conclusion

Y-doped $BaZrO_3$ thin films were produced using pulsed laser deposition and tested as to their suitability as thin film humidity sensing materials. XPS measurements found that the film composition was Ba deficient and Y rich compared to the target composition. As deposited films (800 °C deposition temperature) were polycrystalline. Strong crystallographic texturing at the BZO (1 1 0) and BZO (2 1 1) peaks was observed in all samples. Both peak heights were increased with increasing film thickness, and the FWHM decreased with decreasing film thickness which is commonly observed in thin films. AFM measurements show that as deposited films have low surface roughness, similar to the Si substrate the films were deposited on. The RMS roughness (0.2–1.2 nm) and particle size (32–72 nm) increases with increasing film thickness (200–500 nm). The electrical conductivity was characterized as a function of the partial pressure of water using an interdigitated electrode test structure. The electrical conductivity was characterized over a temperature range of 200–650 °C and could be attributed to oxygen ions, holes, and electrons. The calculated activation energies were between 0.26–0.47 eV at high temperatures indicating a possible oxygen ion conduction mechanism, and between 0.14–0.23 eV at lower temperatures, indicating a possible electron/hole conduction mechanism. This observation appeared to be in accordance with data found in literature. Second-order time constants appeared to depend on temperature, partial pressure of water, and film thickness. An increase in time constants with increase in water vapor pressure, film thickness in both absorption and desorption of water vapor was observed. All samples exhibit an overall decrease in time constants with increasing temperature. Desorption times are larger than absorption times indicating a slower removal process of humidity. Hysteresis of the films is lowest at lower operating temperatures (500–600 °C) and appears to be increasing above 650 °C. The films have principally shown strong stability over a one year time period of intermittent testing (only 2.3% change in base resistance), but a clear drop in sensitivity (35%) that may be due to changes in point defect density. These results present an outstanding basis for future applications in industrial sensors. The reasons for the drop in sensitivity may lie in changes in defect concentration. Upon completion of the test or failure of the sensor, we will carry out a detailed analysis of the film composition in order to gain information about the origin of the sensitivity drop or sensor poisoning.

A detailed comparison and analysis of the characteristics of PLD deposited Y-doped $BaZrO_3$ thin films versus sputter deposited films as presented in an earlier publication as well as preliminary models explaining the behavior of the films are currently under way and will be submitted for publication later this year. Preliminary results suggest that PLD films tend to exhibit a composition, closer to the desired stoichiometry, work better at higher temperatures and have a better lifetime. All other characteristics such as, e.g. time constants and hysteresis appear similar.

Acknowledgments

We gratefully acknowledge support through the Department of Energy National Energy Technologies Laboratory NETL through contract no. DE-FC26-05NT42440. We would also like to express our sincere gratitude to Mr. Jim Greer at PVD products for processing the PLD samples. We would also like to thank Dr. Anil Virkar for valuable discussions on the behavior of sintered bulk BZO material in high temperature humidity environments.

References

[1] W. Wang, A.V. Virkar, Ionic and electron-hole conduction in $BaZr_{0.93}Y_{0.07}O_{3-\delta}$ by 4-probe dc measurements, J. Power Sources 142 (2005) 1–9.
[2] W. Wang, A.V. Virkar, A conductimetric humidity sensor based on proton conducting perovskite oxides, Sens. Actuators, B Chem. 98 (2004) 282–290.
[3] X.X. Chen, L. Rieth, M.S. Miller, F. Solzbacher, High temperature humidity sensors based on Y-doped $BaZrO_3$ thin films, Sens. Actuators, B Chem. 137 (2009) 578–585.
[4] F. Solzbacher, S. Krueger, Microsystems where are we heading, lead article, msrnews (2003) 6–10.
[5] G. Korotcenkov, One-electrode semiconductor gas sensors, in: D.K. Aswal, S.K. Knipe (Eds.), Science and Technology of Chemiresistor Gas Sensors, Nova Sci. Publishers, 2007, pp. 95–145
[6] T. Seiyama, S. Kagawa, Study on a detector for gaseous components using semiconductive thin films, Anal. Chem. 38 (1966) 1069–1073.
[7] G. Neri, A. Bonavita, S. Galvagno, P. Siciliano, S. Capone, CO and NO_2 Sensing properties of doped-Fe_2O_3 thin films prepared by LPD, Sens. Actuators. B Chem. 82 (2002) 40–47.
[8] G. Neri, A. Bonavita, C. Milone, A. Pistone, S. Galvagno, Gold promoted Li-Fe_2O_3 thin films for humidity sensors, Sens. Actuators. B Chem. 92 (2003) 326–330.
[9] R.M. Geatches, A.V. Chadwick, J.D. Wright, Single crystal metal oxide gas sensors, Sens. Actuators, B Chem. 4 (1991) 467–472.
[10] X. Shi, Q. Chen, J. Fang, K. Varahramyan, H. Ji, Al_2O_3-coated microcantilevers for detection of moisture at ppm level, Sens. Actuators, B Chem. 129 (2008) 241–245.
[11] G. Di Francia, A. Castaldo, E. Masserra, I. Nasti, L. Quercia, I. Rea, A very sensitive porous silicon based humidity sensor, Sens. Actuators, B Chem. 111–112 (2005) 135–139.
[12] K. Arshaka, K. Twomey, D. Egan, A ceramic thick film humidity sensor based on MnZn ferrite, Sensors 2 (2002) 50–61.
[13] Y. Sakai, Y. Sadaoka, M. Matsuguchi, Humidity sensors based on polymer thin films, Sens. Actuators, B Chem. 35–36 (1996) 85–90.
[14] H. Iwahara, H. Uchida, S. Tanaka, High temperature type proton conductor based on strontium cerium trioxide and its application to solid electrolyte fuel cells, Solid State Ionics 9–10 (Pt. 2) (1983) 1021–1025.

[15] H. Iwahara, H. Uchida, K. Ogaki, Proton conduction in sintered oxides based on barium cerate, J. Electrochem. Soc. 135 (1988) 529.
[16] H. Iwahara, Proton conduction in sintered oxides and it's application to steam electrolysis for hydrogen production, Solid State Ionics 3–4 (1981) 359.
[17] B. Merinov, C.O. Dorso, W.A. Goddard III, J. Wu, and S. Haile, Enhanced power stability for proton conducting solid oxides fuel cells, Semi-Annual Progress Report, CIT (2003).
[18] T. Schnellr, T. Schober, Chemical solution deposition prepared dense proton conducting Y-doped $BaZrO_3$ thin films for SOFC sensor devices, Solid State Ionics 164 (2003) 131–136.
[19] X.X. Chen, M. Sorenson, C. Butler, L. Rieth, M.S. Miller, F. Solzbacher, $BaZrO_3$ thin film for humidity gas sensor, Mater. Res. Soc. Symp. Proc. 1010 (2007).
[20] J. Ho, E. Heifets, B. Merinov, Ab initio simulation of the $BaZrO_3$ (001) surface structure, Surface Sci. 601 (2) (2007) 491–497.
[21] T. Ishihara, H. Matsuda, Y. Takita, Doped $LaGaO_3$ perovskite type oxide as a new oxide ionic conductor, J. Am. Chem. Soc. 116 (1994) 3801–3803.
[22] X.Y. Yu, G. Chen, Temperature dependence of thermophysical properties of GaAs/AlAs periodic structure, Appl. Phys. Lett. 67 (1995) 3554.
[23] A.S. Nowick, Y. Du, High-temperature protonic conductors with perovskite-related structures, Solid State Ionics 77 (1995) 137.
[24] W. Wang, A.V. Virkar, Determination of ionic and electronic conductivities of $Ba_3Ca_{1.18}Nb_{1.82}O_{9-\delta}$ (BCN 18) in dry and wet atmospheres, J. Electrochem. Soc. 151 (10) (2004) 1565–1571.

Biographies

Xiaoxin Chen received the BS and ME degrees in the Department of Electrical and Computer Engineering from the University of Utah, Salt Lake City, Utah, in 2002 and 2004. She worked as a teaching assistant in University of Utah from 2002 to 2004, and as a research assistant in Chemical Engineering Department at the University of Utah from January 2003 to August 2003. From 2006 to present, she is pursuing PhD in ECE Department at the University of Utah. Her research interests include a high temperature humidity microsensors that based on the thin films of electrochemical materials (Y-doped $BaZrO_3$) and system integration.

Loren Rieth received his BS degree in materials science from The Johns-Hopkins University, Baltimore, MD, in 1994. He received his PhD in materials science and engineering from the University of Florida, Gainesville, FL, in 2001. From 2001 to 2003, he was a postdoctoral research associate at the University of Utah, Salt Lake City, UT, and continued on at the University of Utah as a research assistant professor in materials science (2003–2005), and electrical and computer engineering (2004–present). His research is focused on deposition and characterization of thin film materials for sensors (chemical, physical, and biological), MEMS, BioMEMS, and energy production.

Mark S. Miller received his BS in electrical engineering and chemistry from Colorado State University, Fort Collin, CO, in 1985. He received his MS degree in electrical engineering from the Colorado State University. He worked in NCR Microelectronics as an analog integrated circuit engineer in 1987, Fort Collins, Colorado. And he received his PhD at the University of California in Santa Barbara in 1993. Then he joined as a postdoctoral research associate in the Department of Solid State Physics at the Lund University from 1993 to 1997. From 1997 to 2000, he worked as an assistant professor in the ECE Department at the University of Virginia and started Terahertz Device Corporation. In 2001, he worked as the director of the Microfabrication Laboratories and an assistant professor in both department of ECE and MSE at the University of Utah. Currently, he is a research associated professor at the University of Utah. His research work is mainly focused on investigating new optical and electrical devices that range from increasing the capacity or function of information technology systems to detecting biochemical molecules to producing new power sources.

Florian Solzbacher received his MSc in electrical engineering from the Technical University, Berlin in 1997 and his PhD from the Technical University, Ilmenau in 2003. He is the director of the Microsystems Laboratory at the University of Utah and a faculty member in the Departments of Electrical and Computer Engineering, Materials Science and Bioengineering and is responsible for the Utah branch office of the Fraunhofer IZM, Germany. Dr. Solzbacher is co-founder of First Sensor Technology GmbH, an established supplier to the automotive and process control industry in the USA, Europe and Asia. He is Chairman of the German Association for Sensor Technology AMA. His work focuses on harsh environment microsystems, sensors and materials. He is author of over 60 scientific and engineering publications and book chapters on MEMS devices, technologies and markets for Harsh Environments. Since 2004 he has been Chairman of Sensor + Test, the world's largest international trade fair and ensemble of conferences for sensors, metrology and testing.

CHAPTER 5

COMPARISON OF Y-DOPED $BaZrO_3$ THIN FILMS FOR HIGH TEMPERATURE HUMIDITY SENSORS BY RF SPUTTERING AND PULSED LASER DEPOSITION

Sensors and Actuators B 148 (2010) 173–180

reprinted with permission

Sensors and Actuators B 148 (2010) 173–180

Contents lists available at ScienceDirect

Sensors and Actuators B: Chemical

journal homepage: www.elsevier.com/locate/snb

Comparison of Y-doped $Bazro_3$ thin films for high temperature humidity sensors by RF sputtering and pulsed laser deposition

XiaoXin Chen[a,*], Loren Rieth[a], Mark S. Miller[a], Florian Solzbacher[a,b,c]

[a] Department of Electrical Engineering, University of Utah, Salt Lake City, UT, USA
[b] Department of Material Sciences and Engineering, University of Utah, Salt Lake City, UT, USA
[c] Department of Bioengineering, University of Utah, Salt Lake City, UT, USA

ARTICLE INFO

Article history:
Received 29 December 2009
Received in revised form 15 March 2010
Accepted 23 March 2010
Available online 1 April 2010

Keywords:
Thin film
Humidity
High temperature
Y-doped $BaZrO_3$
Sputtering
PLD

ABSTRACT

This paper presents a comprehensive comparison of the fabrication processing parameters and the electrical, mechanical, chemical, and sensing properties of sputtered and pulsed laser deposited (PLD) Y-doped $BaZrO_3$ thin films for the use in high temperature (400–650 °C) water vapor partial pressure measurements.

RF sputtered thin films with thicknesses of between 200 and 750 nm, at pressures between 0.45 and 50 mTorr and deposition powers between 50 and 300 W were deposited and annealed at 800 °C or 1000 °C for 3 h in air. Correlations between mechanical film stress, X-ray photoelectron spectroscopy (XPS), X-ray diffraction (XRD), and atomic force microscopy (AFM) stoichiometry data, crystallographic, surface morphology and process and film parameters are presented. Furthermore, the baseline resistivity was characterized as function of film thickness and temperature.

PLD samples with thicknesses between 200 and 500 nm were deposited at room temperature to 800 °C. All samples were characterized as deposited. 200 and 500 nm thick samples were also annealed at 1000 °C for 3 h in air and characterized post-anneal. The Ba concentration vs. substrate temperature remained stable within 12–16%, correlating with those Ba concentrations that yield good sensitivity (0.25–8 atm^{-1}). The low dependence of the Ba concentration on the deposition parameters indicates that the PLD deposition process allows larger process windows for the deposition of good sensitivity thin film material compared to sputtering.

Water vapor partial pressure sensitivity indicated a decrease in sensitivity with decrease in Ba concentration in the films. Partial transition of the Y-doped $BaZrO_3$ to ZrO_2 and subsequent decrease in oxygen vacancy sites could explain the loss in sensitivity. PLD samples were on average more stable and repeatable and less process dependent, but had lower sensitivity towards humidity. This could be explained by the higher, more stoichiometric and less process dependent Ba concentration of these samples compared to the sputtered samples. At high temperatures (>550 °C) only the PLD samples exhibit stable sensitivity towards humidity.

The resulting activation energies for the sputtered samples are only slightly larger than those of the PLD samples at lower temperatures (hole conduction) and much larger at high temperatures (oxygen ion conduction). Annealing of the PLD samples at 1000 °C increases the sensor response time by 10 times and the relaxation time by a factor of 8. Sputtered samples do not survive annealing at 1000 °C. PLD samples also by far outlast sputtered samples in terms of lifetime.

1. Introduction

Increasing emission and efficiency requirements call for reliable, selective, and high temperature (T > 400 °C) compatible sensor devices to monitor and control the concentration of exhaust gases in combustion processes [1]. Target gas species include CO, CO_2, H_2S, NO_x, and humidity (water vapor). Y-doped $BaZrO_3$ ($BaZr_{0.8}Y_{0.2}O_{3-\delta}$) bulk material has demonstrated high response and selectivity towards humidity [2,3]. Recent publications have presented that thin films of Y-doped $BaZrO_3$ can be fabricated, which would potentially significantly reduce sensor response time, increase sensitivity, and allow integration into micro gas sensor elements [4,5].

Some solid state humidity sensors today are based on chemisorption of H_2O, lack selectivity towards NO_x and O_2 and are not functional at high temperatures for the use in exhaust gas

* Corresponding author. Tel.: +1 8016714407.
E-mail address: Xiao_C@yahoo.com (X. Chen).

0925-4005/$ – see front matter © 2010 Elsevier B.V. All rights reserved.
doi:10.1016/j.snb.2010.03.074

streams [6–9]. Y-doped $BaZrO_3$ can exhibit oxygen vacancies when doped with a trivalent cation (e.g., Y^{3+} on a Zr^{4+} site). In atmosphere, this material contains oxygen ions and holes. The same material when heated in an environment containing H_2O allows the absorption of H_2O into the lattice lowering the oxygen vacancy concentration, and releasing protons [10–15].

RF sputtering and pulsed laser deposition (PLD) techniques can be used to deposit thin films of $BaZrO_3$. This work presents a comprehensive comparative study of Y-doped $BaZrO_3$ thin films as high temperature humidity sensors deposited by RF sputtering and PLD.

2. Experimental methods

Y-doped $BaZrO_3$ of 200, 300, 400, 500, and 750 nm thin films were deposited onto 2 in. n-type (100) silicon substrates with 250 nm thick oxide layers. RF sputtering at room temperature (RT) was used in a vacuum ambient with base pressures of 0.45–50 mTorr at various deposition powers (50–250 W). PLD films were deposited onto identical substrates at substrate temperatures between RT and 800 °C in a vacuum ambient with base pressure at ~10^{-6} Torr. Film thicknesses range from 200 to 500 nm. All films were characterized using X-ray photoelectron spectroscopy (XPS), X-ray diffraction (XRD), and atomic force microscopy (AFM), to determine film composition, microstructure, and surface morphology. Electrical conductivity as function of temperature and water vapor humidity sensing characteristics of the films were measured using a custom-built gas sensor test station at temperatures of up to 650 °C. Interdigitated electrode (IDE) structures were fabricated using a Cr (20 nm) and Au (180 nm) thin film metallization on oxidized Silicon wafers as previously published [4,5].

2.1. Characterization of film composition and structure

RF sputtered films of Y-doped $BaZrO_3$ were deposited from a 3 in. diameter, 99.9% pure ceramic $BaZr_{0.8}Y_{0.2}O_{2.9}$ sputtering target purchased from Process Materials Inc. The films were sputter deposited at room temperature on oxidized (250 nm SiO_2) 2 in. n-type (100) silicon substrates using an UHP (99.999%) Ar sputtering ambient in a Denton Discovery 18 system. Deposition pressures of between 0.45 and 2.5 mTorr were maintained using an Ar flow of 1.5–10 standard cubic centimeter per minute (sccm) and an RF (13.56 MHz) power of 50, 75, 100, 150, 225, and 250 W. In addition, samples at deposition pressures of 25 and 50 mTorr were deposited using the same target in a sputtered film incorporated (SFI) system with RF (13.56 MHz) power of 100 W. This system allowed stable deposition even at high process pressures. Films with thicknesses of 200, 300, 400, 500, and 750 nm were deposited. All films were annealed in air at 800 °C for 3 h. Film stress was characterized by measuring change in wafer bow with a Tencor stylus profilometer before and after annealing and confirmed by analysis of XRD data.

PLD films were deposited in two runs in two different systems. Initial PLD samples were deposited on identical substrates from a 1 in. diameter, 99.9% pure ceramic $BaZr_{0.8}Y_{0.2}O_{2.9}$ pure ceramic target purchased from Process Materials Inc. Samples were deposited onto 1 cm^2 substrates at a base pressure of 10^{-6} Torr between RT and 700 °C and were annealed in air at 800 °C for 3 h for an initial investigation. The films were grown at 350 mJ/pulse laser energy with average energy flux of 2–3 J/cm^2. There is no water vapor response from this set of PLD films.

The second set of PLD samples were deposited on 2 in. n-type (100) silicon substrates with 250 nm of SiO_2 from the same 1 in. diameter, 99.9% pure ceramic $BaZr_{0.8}Y_{0.2}O_{2.9}$ pure ceramic target at PVD products Inc (Wilmington, MA). The films were grown at 250 mJ/pulse laser energy with average energy flux of 1 J/cm^2 at 800 °C. Film with center thickness of 200, 300, 400, and 500 nm were deposited. Selected PLD films were annealed in air at 1000 °C for 3 h to analyze the impact on the humidity response.

Thicknesses of all films were determined using a Tencor stylus profilometer and a Woolam V-Vase spectroscopic ellipsometer. XPS measurements were made using a Kratos Axis ULTRA^{DLD} system using monochromatic Al Kα radiation. Composition data was recorded for as received samples and after 4 min of Ar^+ ion beam etching. XRD measurements were made using a Philips X'Pert system using Cu Kα radiation in the Bragg–Brentano geometry for 2θ angles from 10° to 90°. AFM micrographs were collected with a Veeco Dimension 3000 system using etched Si tapping mode tips with a nominal tip radius of ~5 nm.

2.2. Water vapor sensitivity measurements

The water vapor sensing characteristics for $BaZrO_3$:Y thin films were measured using a custom-built gas sensor test station. Sample chips were placed on a hotplate in a stainless steel chamber and contacted with probe needles attached to a PC/labview controlled Keithley digital multimeter in voltage measurement mode. N_2 carrier gas at 200 sccm was passed through a water bath at 80 °C, saturating the gas at 0.468 atm water vapor pressure. Before the water vapor reaches the test chamber, it is diluted with 1380 sccm N_2 gas. Once the saturated gas enters the test chamber it is heated to the sensor operating temperature and the partial pressure and therefore relative humidity of the gas drops as a function of temperature. The partial pressures of water are calculated by the percentage of total gas flow in one atmosphere.

Sample resistance values were determined based on the voltage measurements using a 0.7 μA supply current that would not lead to self heating of the film. The response to water vapor was measured at 0.058 atm partial pressure of water at 400–650 °C. The film conductivity was determined using

$$\sigma = \frac{L}{RAn} \tag{2.2.1}$$

where σ is the film conductivity ($[\sigma] = 1$ S/cm), R is the measured resistance ($[R] = 1$ MΩ), A is the cross sectional area of the sample ($[A] = 1$ cm^2), L is the distance between each interdigitated electrode ($[L] = 1$ cm), and n is the number of interdigital electrode pairs ($n = 10$).

3. Results and discussion

A set of experimental parameters was presented in this investigation for physical vapor deposition (PVD) of Y-doped $BaZrO_3$ thin films. Table 1 shows the deposition parameters of sputtered Y-doped $BaZrO_3$ thin films. All sputtered films were annealed in air at 800 °C for 3 h. Deposition rate of the films appeared to increase with increasing deposition power and deposition pressure. The deposition rate exhibits a significant increase at deposition powers above 225 W for all deposition pressures. Mud flat cracking of the films is occurring for films (a) thicker than 400 nm (b) deposited at above 150 W of power, and (c) deposition pressures above 1.5 mTorr. Cracking is likely caused by tensile stress accumulated during deposition and annealing.

The deposition conditions for PLD thin films are shown in Table 2. Deposition rates are increasing with increasing substrate temperature. Deposition rates are ranging between 3.3 and 5.2 Å/s, which are close to one order of magnitude higher than most deposition rates obtained by sputtering. Samples gg, hh, ii, and jj were deposited at the University of Utah. Samples kk, ll, mm, nn, oo, and pp were deposited at PVD Products Inc. All annealed PLD films exhibit cracks.

Table 1
Deposition parameters of Y-doped $BaZrO_3$ thin films by RF sputtering. All samples are annealed in air at 800°C for 3 h.

Sample name	Deposition pressure (mTorr)	Deposition power (W)	Film thickness (nm)	Deposition rate (Å/s)	Mud flat cracking after annealing
a	0.45	50	200	0.18	No
b		75		0.24	
c		100		0.33	
d		150		0.47	
e		225		0.70	
f		250		0.92	
g	0.9	50	300	0.26	
h		75		0.39	
i		100		0.46	
j		150		0.62	
k		225		0.81	
l		250		1.01	
m	1.3	50	400	0.35	
n		75		0.41	
o		100		0.53	
p		150		0.76	
q		225		1.36	
r		250		1.47	
s	1.5	50	500	0.42	Yes
t		75		0.64	
u		100		0.69	
v		150		1.42	
w		225		2.01	
x		250		2.33	
y	2.5	50	750	0.46	
z		75		0.76	
aa		100		1.16	
bb		150		1.74	
cc		225		2.99	
dd		250		3.14	
ee	25	100	200	0.34	
ff	50	100	200	0.51	

3.1. Film characterization

Annealing processes are generally used to cause microstructure changes in the material that may yield more stable and reproducible sensor measurements at high temperatures. In our samples, mud flat cracking was observed in more than 60% of sputtered samples and in all annealed PLD samples, indicating potentially high tensile stress. Stress data for sputtered films were determined based on measurements of changes in wafer/sample bow with a Tencor stylus profilometer before and after annealing (Fig. 1) and using the following equation

$$\sigma_{\text{stress}} = \frac{1}{6}\left(\frac{1}{R_{\text{post}}} - \frac{1}{R_{\text{pre}}}\right)\frac{E}{(1-\nu)}\frac{t_s^2}{t_f} \tag{3.1.1}$$

σ_{stress} is stress in the film after the deposition ($[\sigma_{\text{stress}}] = 1$ MPa), R_{pre} is the substrate radius of curvature before deposition, R_{post} is substrate radius of curvature after deposition, E is Young's modulus ($[E] = 129$ GPa), ν is Possion's ratio of substrate ($[\nu] = 0.28$), t_s is substrate thickness ($[t_s] = 1$ μm), and t_f is film thickness ($[t_f] = 1$ μm). Film stress was not determined for PLD samples due to the small substrate size, which renders the determination of the stress using changes in wafer or sample bow too inaccurate to allow comparison with data generated with larger samples.

Based on Fig. 1, while the overall range of stress observed cover compressive and tensile stresses from −80 to +110 MPa, the majority of sputtered samples exhibits tensile stress. Some samples appear to very low stress (±10 MPa). This drop in stress may be caused by the cracking of the films allowing for a partial relaxation of the film.

The chemical composition of the films was measured by XPS from as received samples, and after 4 min ion beam etching. The film compositions were quantified from the spectra. The Ba atomic concentration in the films was studied and compared as shown in Figs. 2 and 3.

Deposition power and deposition pressure both influence the Ba atomic concentration in the film. The deposition pressure has a stronger effect on the Ba atomic concentration than deposition power. The Ba content of the films increases with increasing deposition pressure between 0.45 and 2.5 mTorr and appears to stabilize around 6% at higher deposition pressure (25 and 50 mTorr). Fig. 2(a) shows a shifted normalized Gaussian function with the maximum

Table 2
Deposition parameters of Y-doped $BaZrO_3$ thin films by pulsed laser deposition with substrate-target distance of 40 mm.

Sample name	Laser energy (mJ)	Pulse energy density (J/cm²)	Substrate temperature (°C)	Film thickness (nm)	Deposition pressure (10^{-6} Torr)	Deposition rate (Å/s)	Annealing condition
gg	350	2	21	200	1	3.3	Air, 3 h 800°C
hh			400			3.6	
ii		3	600			4.2	
jj			700			4.7	
kk	250	1	800	200	0.85	5.1	Not annealed
ll				300			
mm				400			
nn				500			
oo				200			Air, 3 h 1000°C
pp				500			

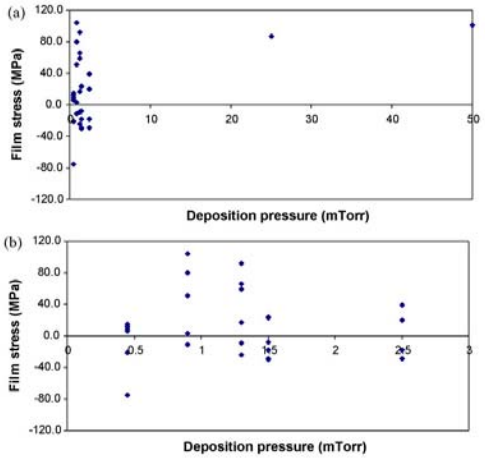

Fig. 1. Film stress as a function of deposition pressure for RF sputtering samples (a) deposition pressure between 0.45 and 50 mTorr, and (b) deposition pressure between 0.45 and 2.5 mTorr.

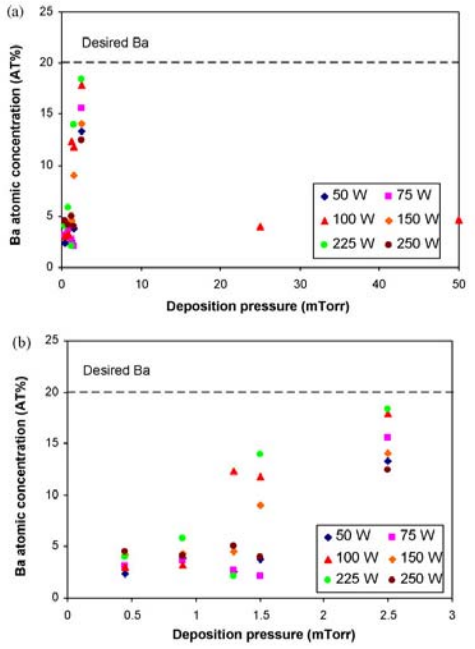

Fig. 2. Ba atomic concentration (AT%) as a function of deposition pressure after 4 min ion beam etching, quantified by XPS measurements a) for sputtered samples (a–ff) as function of deposition pressure; (b) for samples (a–dd). Ba AT% ranges between 2% and 18%, showing a clear Ba deficit to the 20% desired Ba content.

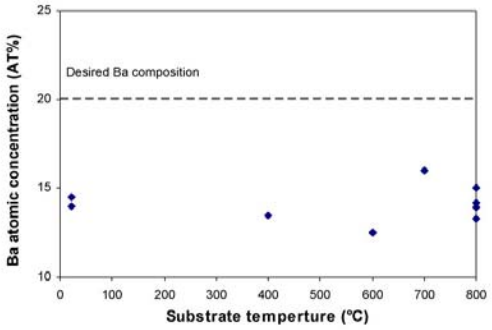

Fig. 3. Ba atomic concentration (AT%) quantified by XPS measurements for PLD samples (gg–pp) as function of substrate temperature. Ba AT% is between 13% and 16%. Data indicate that the Ba content is close to the nominal target composition and appears to have good reproducibility and stabilization in all substrate temperatures.

Ba content of 18% at of 225 W deposition power and 2.5 mTorr deposition pressure. Fig. 2(b) also exhibits a large shift in Ba content with deposition power in the range of 0.45 to 2.5 mTorr.

Data indicate that the Ba content is close to the nominal target composition and appears to have good reproducibility and stabilization in all substrate temperatures.

Ba compositions of the PLD films were quantified from the spectra and are summarized in Fig. 3. XPS data indicate that the film composition is comparably closer to the nominal target composition with good reproducibility and stable film compositions. The films were however still Ba deficient in all cases.

The much more significant Ba deficiency in the sputtered samples likely results from a re-sputtering affect and may also be the reason for the cracking of the films. The PLD film compositions are closer to the nominal target composition with stable Ba content at all substrate temperatures. The results suggest that sputtering has a smaller process window for fabricating controlled stoichiometry of Y-doped $BaZrO_3$ thin films compared to PLD.

XRD reflections were collected to investigate the microstructure of the sputtered and PLD films, and are presented in Fig. 4. Sputtered samples c, i, o, u, and aa and PLD samples kk, ll, mm, nn, and oo were selected. For details of deposition parameters and annealing conditions of all samples, please refer to Tables 1 and 2. The reflections indicate that as deposited sputtered films were amorphous and became polycrystalline after heat treatment. As deposited PLD samples with substrate temperature of 800 °C were polycrystalline in character. The dashed vertical lines on the plots represent the JCPDS values for (1 1 0), (1 1 1), (2 0 0), (2 1 1), (2 2 0), and (3 2 1) reflections for $BaZrO_3$. The reflections are shifted to higher 2θ values compared to the JCPDS database, which would be consistent with the films being under compressive stress in the out-of-plane direction. These results are also consistent with the presence of the (2 0 0) Si peak, a normally unallowed peak, which appears due to strain in the Si substrate. Another possible reason for the shift of the reflections is the Ba deficiency as indicated in Figs. 2 and 3. The reflection heights of BZO (1 1 0) and BZO (2 1 1) reflections were increased with increasing film thickness for both sputtered and PLD deposition (Fig. 5a). The reflections also show that PLD samples have a more pronounced reflection than sputtered samples in all cases. The FWHM value appears to decrease with increasing film thickness for both sputtered and PLD films (Fig. 5b). This is consistent with both a thinner film and a decrease in crystal quality of the film, which could be caused by damage in the crystal, e.g., expanding of grain sizes.

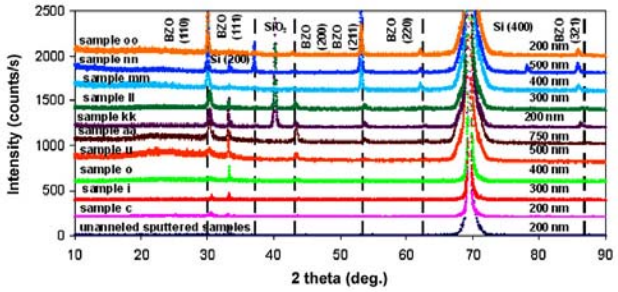

Fig. 4. X-ray diffraction reflections collected from as deposited and annealed sputtered samples c, i, o, u, and aa (details of deposition and annealing conditions in Table 1). As deposited PLD samples kk, ll, mm, nn, and annealed sample oo (details of deposition and annealing conditions in Table 2).

AFM was used to characterize the surface morphology of all samples before and after annealing. Selected sputtered films (c, i, o, and u) and PLD films (ll, mm, nn, and oo) are presented to illustrate AFM results. AFM micrographs for all films have a similar surface morphology consisting of nano-scale surface particles. Particle size and RMS roughness increased with increasing film thickness. The particle sizes increased from 70 to 170 nm for sputtered samples and 32–72 nm for PLD samples. Root mean squared (RMS) roughness increased from 1.3 nm to 4.2 nm for sputtered samples and 0.2–1.2 nm for PLD samples. Fig. 6 presents AFM micrographs of particle sizes and RMS roughness for both sputtered and PLD method, using a stereological technique.

According to Fig. 6, films from both deposition methods have a very fine particle size and smooth surface. The film roughness and the particle size are increasing with increasing film thickness. AFM results revealed that PLD samples have a smaller particle size and less than 10 times smaller RMS roughness than sputter deposited samples.

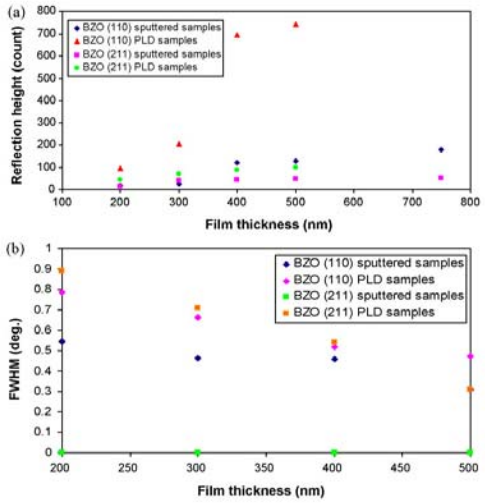

Fig. 5. (a) XRD reflection height vs. film thickness for Y-doped $BaZrO_3$ sputtered films c, i, o, u, and aa and PLD samples kk, ll, mm, and nn. The peak height is increasing with increasing film thickness in all samples. (b) Full width at half maximum (FWHM) vs. film thickness for Y-doped $BaZrO_3$ sputtered films c, j, o, and u and PLD samples kk, ll, mm, and nn. The FWHM is decreasing with increasing film thickness.

3.2. Temperature dependence

The film electrical conductivity as function of temperature was characterized in the range from 200 to 650 °C in order to determine the variation of base line resistance with temperature during humidity measurements and to gain information on potential electrical conduction mechanisms in the material.

The conductivity of the samples increases exponentially with increasing temperature (Fig. 7). This relation can be described as [16,17]:

$$\sigma_t = \sigma_0 e^{-\frac{E_a}{kT}} \quad (3.2.1)$$

where σ_t is the conductivity as function of temperature in S/cm, σ_0 is the initial conductivity at 473 K in S/cm, E_a is the activation energy in eV, and k is Boltzmann's constant (8.62×10^{-5} eV/K). Activation energy was generated based on approximate linear fits in the log-plot of film conductivity vs. temperature (200–650 °C) in N_2 ambient gas at a flow of 1380 sccm. Using a first order linear approximation for the slope, a change in activation energy can be observed that could be divided into two distinct regions with different conduction mechanisms.

Based on Fig. 7, the activation energy is increasing with increasing film thickness for both sputtered and PLD samples. PLD films require less activation energy at all temperature range. This may be caused by a difference in point defect density on the film surface or different formation of the crystal structure for the different deposition methods.

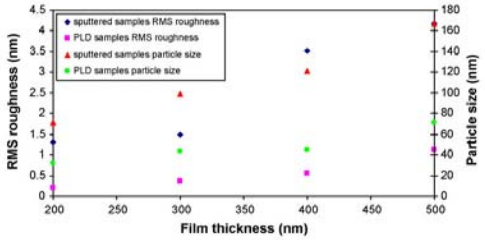

Fig. 6. RMS roughness and particle size vs. film thickness for Y-doped $BaZrO_3$ for annealed sputtered films (c, i, o, and u), and as deposited PLD films (kk, ll, mm, and nn). Both particle sizes and RMS roughness increase with increasing film thickness for both deposition methods.

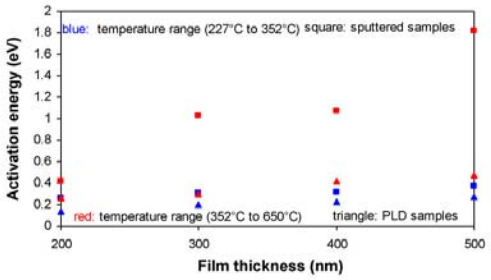

Fig. 7. Activation energy (E_A) vs. film thickness for both annealed sputtered samples (c, i, o, and u), and as deposited PLD films (kk, ll, mm, and nn). Two distinct regions of activation energies are apparent in original data. Activation energy was generated based on approximate linear fits in the log-plot of film conductivity vs. temperature (200–650 °C) in N_2 ambient gas at a flow of 1380 sccm. This is consistent with the conduction mechanism of Y-doped $BaZrO_3$ (O^{2-} and electron-hole conductions) presented in literature [18–24]. The activation energy is increasing with increased film thickness for both sputtered and PLD samples. PLD films require less activation energy at all temperatures.

3.3. Water vapor response

Y-doped $BaZrO_3$ can exhibit oxygen vacancies when doped with a lower valence ion, e.g., Y^{3+} on the Zr^{4+} sites. In air atmosphere, this material contains oxygen ions, and holes. The same material when heated in an environment containing H_2O allows the absorption of H_2O into the lattice lowering the oxygen vacancy concentration, and releasing protons. H_2O molecules dissociate when the water vapor passes the Y-doped $BaZrO_3$ material at high temperature. H_2O molecules will fill in oxygen vacancies, and release protons and electrons. Protons diffuse through the material through reorientation and proton displacement (also called proton hopping) and combine with electrons releasing H_2. In addition, oxygen ions can "hop" through the material and combine with holes releasing O_2.

All samples are initially exposed to dry N_2 gas. Then, water vapor is introduced into the test chamber. Once the electrical conductivity has stabilized, the atmosphere is changed back to dry air. As expected, the conductivity increases when exposed to water vapor [2,3]. The samples were measured at partial pressures of water of 0.058 atm at temperatures of 400, 500, and 650 °C.

Film sensitivity as stated below is calculated based on:

$$S = \frac{(\sigma t - \sigma 0)}{(\sigma 0 \times \Delta C)} \quad (3.3.1)$$

where S is the sensitivity in atm^{-1}, σ_t is the conductivity upon exposure to humidity at a given temperature T, σ_0 is the initial conductivity without humidity exposure. ΔC is the changing partial pressure of water in atmosphere. Sensitivities up to 27 atm^{-1} were measured for sputtered films and 8 atm^{-1} were measured for PLD films both at a water partial pressure of 0.058 atm.

Sputtered sample o has the highest humidity sensitivity of 27 atm^{-1} at 400 °C with 12% Ba atomic concentration. Previously published results showed sensitivities for sputtered samples of up to 62 atm^{-1} at 400 °C [4]. However, no humidity response could be observed for these films at 500 °C and above. Potential reasons for the lack of stable electrical and sensing properties could lie in the comparably low annealing temperatures for these samples. Sputtered samples could not operate functionally after annealing at 1000 °C in air for 3 h due to the significant cracks as a consequence of high tensile stress caused by annealing. Therefore, the operating temperature of sputtered samples is limited. Sensitivities above 5 atm^{-1} could be found in the sputtered films with at least 8% Ba atomic concentration. Further investigations are required in high deposition pressure range (>50 mTorr), which could reduce the film stress during sputtering, and which may hence reduce the possibility of cracking.

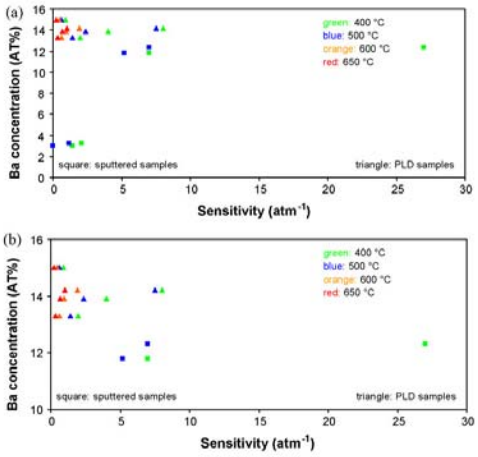

Fig. 8. Humidity sensitivity as function of Ba AT% (a) for all samples and (b) for Ba AT% above 10%. Sputtered (c, i, o, and u) and PLD (kk, ll, mm, and nn) thin films were tested at water partial pressure of 0.058 atm at temperatures of 400, 500, 600, and 650 °C. Maximum sensitivities were measured at 27 atm^{-1} for sputtered and 8 atm^{-1} for PLD films at 400 °C.

PLD films showed humidity sensitivity between 400 and 650 °C, but the sensitivity is one order of magnitude smaller than that for sputtered films. The sensitivity difference may be caused by differences in oxygen vacancies density. Another possible reason may be the different film surface roughness. Based on AFM data (Fig. 6), the surface roughness of the sputtered samples is at least one order of magnitude higher than that of the PLD samples. This creates a larger surface area for adsorption or desorption of water molecules. Since the number of available adsorption sites depends on the free surface area of the film, sputtered samples should therefore have a higher sensitivity towards to humidity than PLD samples. Future work will include high frequency impedance spectrometry measurements during absorption and desorption, which may help unveil the differences in response (Fig. 8).

3.4. Time constant

In previous publications [4,5], we had discussed that H_2O molecules dissolving into the lattice would lower the oxygen vacancy concentration and release protons into the material in the presence of water vapor at high temperatures. We have characterized and correlated the response and the recovery times of the sensors and the film thickness at operating temperature of 400, 500, 600, and 650 °C at partial pressures of water of 0.058 atm as deposited and post-anneal (Fig. 9). The response time and recovery time are defined as the time required for the conductivity of the sensor element to reach 90% of the equilibrium value following a step increasing in water vapor concentration and the time required for the conductivity of the sensor to drop 90% of the base conductivity [25].

The sensors response time and recovery time appear to increase with increasing film thickness with the exception of 500 nm thick sputtered films operated at 400 °C. This particular data point may have to be used with caution, since this set of samples showed

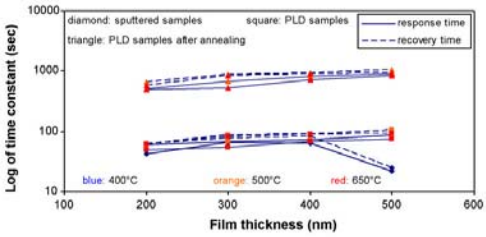

Fig. 9. Required response time and recovery time of the sensor element to reach or drop by 90% of the conductivity.

significant variations in observed sensitivity and time constants [4]. None of the sputtered samples survived annealing at 1000 °C. Annealing of the PLD samples at 1000 °C increases the sensor response time by approximately 10 times and the recovery time by 8 times. The sensor conductivity has increased by a factor of 2–3 while the sensitivity has dropped by a factor of 1–2. A possible explanation for the tremendous slowing of the sensor response could lie in changes in the microstructure that lead an increase in oxygen vacancies but more compact layers to a slowing of the exchange of the water molecules with the sensor material surface.

3.5. Stability

Shelf- and lifetime of the sensors is a key factor in evaluating the stability of the films and sensors. In an attempt to replicate typical user scenarios, we stored both sputtered and PLD humidity sensors in gel-pac boxes at room temperature in the microfabrication clean room upon completion of the initial test run. The sensors were then retested under identical conditions at regular intervals. For each test cycle, the sensors were first placed into the test chamber while exposing them to dry N_2 gas at 1380 sccm ramping up to 500 °C for 2 h to stabilize the initial electrical conductivity of the material. Then water vapor was introduced into the test chamber with between 0 and 0.058 atm of partial pressure of water. Once the electrical conductivity values have stabilized, the atmosphere is changed back to dry N_2. Fig. 10 illustrates the change in sensitivity and base resistivity of the 400 nm sputtered and PLD humidity sensors over a period of 52 weeks with the corresponding film base resistivity as an indicator of sensor stability.

The sensitivity of the sputtered films dropped from 12 to 0 atm^{-1} in 12 weeks. The resistivity however remained stable until the 12th week. PLD films retain stable sensitivity and resistivity throughout an entire 1 year time period. The shift in sensitivity observed in the PLD film may be caused by a change in film composition or

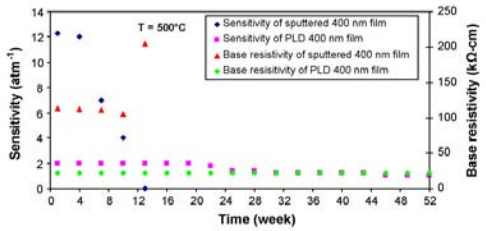

Fig. 10. Humidity sensor stability test for 400 nm thick sputtered (sample o) and PLD films (sample mm) over a 52-week period.

structure, which however does not affect the baseline resistivity. A potential explanation may be that the sensing mechanism takes place in the surface layers of the film, only, dominating the electrical conductivity at high temperatures and during humidity exposure. Without water vapor, the "bulk" of the film dominates the electrical properties. This hypothesis is supported by other literature on bulk Y-doped BZO that suggests surface or surface layer effects to be responsible for changes in electrical conductivity [2]. Upon complete failure of the device, we will analyze the chemical composition, structure and texture of the films again and compare with the initial measurements prior to the long-term test in order to test for changes due to humidity exposure that can explain the drop in resistance.

The stability results in Fig. 10 clearly show an aging effect of the humidity sensors over time. The humidity sensitivity and base resistance of the PLD film remain comparably stable under the harsh testing conditions and high temperatures for more than one year. Sputtered samples produce a high sensitivity towards humidity during the first 8 weeks. The sensor however ages faster than the PLD sample. No significant change in the sputtered film composition after sensor failure could be observed. Regular re-calibration or high temperature cleaning routines of the sputtered film did not recover the film sensitivity.

4. Conclusion

Y-doped $BaZrO_3$ thin films were produced using sputtered and pulsed laser deposition, characterized and tested as to their suitability as thin film humidity sensing materials. PLD films allow for a larger process window leading to more reliable reproduction of films, a composition closer to the stoichiometric ratio and better long-term stability. PLD film sensitivity is lower than that of sputtered films, but remains comparably high over a larger temperature range and is more long-term stable.

Sputtered films were deposited and characterized at multiple pressures and powers and annealed at two temperatures. Mechanical stress, XRD, AFM and XPS data were generated. PLD films ranging from 200–500 nm were deposited and fully characterized as deposited and annealed at 800 and 1000 °C. The Ba concentration vs. substrate temperature correlation yields stable and repeatable film composition between 10% and 16% Ba. In this composition range, films always exhibit good sensitivity towards water vapor. Below a minimum Ba concentration, films do not respond to humidity. Above this threshold, sensitivity is not much affected by the Ba concentration. A potential explanation for this behavior could be that the Ba deficiency leads to the film converting to ZrO_2 below a certain Ba threshold. Activation energy: the comparison of sputtered and PLD films shows that the activation energy measured in sputtered films is larger than that in PLD films. A potential explanation could be that at lower energies hole conduction dominates in which case the activation energies are similar for both types of films (in PLD slightly smaller than sputtered films). At higher activation energies/temperatures oxygen ion conduction will dominate with the activation energy for PLD films $\ll$ sputtered films. This could be caused by a higher concentration of oxygen vacancies in sputtered films. This could explain the initially higher sensitivity, but also account for a more drastic and permanent chemical change during exposure to water vapor, which eliminates the sensitivity. Another possible reason to explain the difference between sputtered and PLD samples could be the different film surface roughness. XRD and XPS data from sputtered and PLD samples were compared pre and post anneal. It was observed that saturation times increased by a factor of 10 and relaxation times increased by a factor of 8, i.e., films become slower due to annealing. The lifetime of PLD and sputtered films (sensitivity and base resistance) was compared with PLD films and was exceeding 1 year of operation.

Acknowledgments

We gratefully acknowledge support through the Department of Energy National Energy Technologies Laboratory NETL through contract no. DE-FC26-05NT42440. We would also like to express our sincere gratitude to Mr. Jim Greer at PVD products for processing the PLD samples and to Dr. Ashutosh Tiwari for first generation PLD initial samples. We would also like to thank Dr. Anil Virkar for valuable discussions on the behavior of sintered bulk BZO material in high temperature humidity environments.

References

[1] F. Solzbacher, S. Krueger, Microsystems where are we heading, lead article, Msrnews (2003) 6–10.
[2] W. Wang, A.V. Virkar, Ionic and electron-hole conduction in $BaZr_{0.93}Y_{0.07}O_{3-\delta}$ by 4-probe dc measurements, J. Power Sources 142 (2005) 1–9.
[3] W. Wang, A.V. Virkar, A conductimetric humidity sensor based on proton conducting perovskite oxides, Sens. Actuators, B Chem. 98 (2004) 282–290.
[4] X.X. Chen, L. Rieth, M.S. Miller, F. Solzbacher, High temperature humidity sensors based on Y-doped $BaZrO_3$ thin films, Sens. Actuators, B Chem. 137 (2009) 578–585.
[5] X.X. Chen, L. Rieth, M.S. Miller, F. Solzbacher, Pulsed laser deposited Y-doped $BaZrO_3$ thin films for high temperature humidity sensors, Sens. Actuators, B Chem. 142 (2009) 166–174.
[6] T. Seiyama, S. Kagawa, Study on a detector for gaseous components using semiconductive thin films, Anal. Chem. 38 (1966) 1069–1073.
[7] G. Neri, A. Bonavita, S. Galvagno, P. Siciliano, S. Capone, CO and NO_2 Sensing properties of doped-Fe_2O_3 thin films prepared by LPD, Sens. Actuators, B Chem. 82 (2002) 40–47.
[8] G. Neri, A. Bonavita, C. Milone, A. Pistone, S. Galvagno, Gold promoted Li-Fe_2O_3 thin films for humidity sensors, Sens. Actuators, B Chem. 92 (2003) 326–330.
[9] R.M. Geatches, A.V. Chadwick, J.D. Wright, Single crystal metal oxide gas sensors, Sens. Actuators, B Chem. 4 (1991) 467–472.
[10] H.G. Bohn, T. Schober, Electrical conductivity of the high temperature proton conductor $BaZr_{0.9}Y_{0.1}O_{2.95}$, J. Am. Ceram. Soc. 83 (2000) 768–772.
[11] K.D. Kreuer, Proton conducting oxides, Ann. Rev. Mater. Res. 33 (2003) 333–359.
[12] C.D. Savaniu, J. Canales-Vazquez, J.T.S. Irvine, Investigation of proton conducting $BaZr_{0.9}Y_{0.1}O_{2.95}$: $BaCe_{0.9}Y_{0.1}O_{2.95}$ core shell structure, J. Mater. Chem. 15 (2005) 598–604.
[13] M. Laidoudi, I.A. Talib, R. Omar, Investigation of the bulk conductivity of $BaZr_{0.95}M_{0.05}O_3$ (M = Al, Er, Ho, Tm, Yb, and Y) under wet N_2, J. Phys. D Appl. Phys. 35 (2002) 397–401.
[14] F.M.M. Snijkers, A. Buekenhoudt, J. Cooymans, J.J. Luyten, Proton conductivity and phase composition in $BaZr_{0.9}Y_{0.1}O_{3-delta}$, Scripta Mater. 50 (2004) 655–659.
[15] F. Iguchi, T. Yamada, N. Sata, T. Tsurui, H. Yugami, The influence of grain structures on the electrical conductivity of a $BaZr_{0.95}Y_{0.05}O_3$ proton conductor, Solid State Ionics 177 (2006) 2281–2284.
[16] T. Ishihara, H. Matsuda, Y. Takita, Doped $LaGaO_3$ perovskite type oxide as a new oxide ionic conductor, J. Am. Chem. Soc. 116 (1994) 3801–3803.
[17] X.Y. Yu, G. Chen, Temperature dependence of thermophysical properties of GaAs/AlAs periodic structure, Appl. Phys. Lett. 67 (1995) 3554–3556.
[18] K.D. Kreuer, On the complexity of proton conduction phenomena, Solid State Ionics 149 (2000) 136–137.
[19] R. Glockner, M.S. Islam, T. Norby, Protons and other defects in BaCeO: a computational study, Solid State Ionics 122 (1–4) (1999) 145–156.
[20] R.A. Davies, M.S. Islam, J.D. Gale, Dopant and proton incorporation in perovskite-type zirconates, Solid State Ionics 126 (1999) 323–335.
[21] H. Iwahara, T. Yajima, T. Hibino, K. Ozaki, H. Suzuki, Study on current efficiency of steam electrolysis using a partial protonic conductor $SrZr_{0.9}Yb_{0.1}O_{3-\alpha}$, Solid State Ionics 61 (1993) 65–69.
[22] T. Yajima, H. Iwahara, Defect structure analysis of B-site doped perovskite-type proton conducting oxide $BaCeO_3$ Part 1: The defect concentration of $BaCe_{0.9}M_{0.1}O_{3-\delta}$ (M = Y and Yb), Solid State Ionics 53–56 (1992) 983–988.
[23] T. Scherban, A.S. Nowick, Protonic conduction in Fe-doped $KTaO_3$ crystal, Solid State Ionics 53–56 (1992) 1004–1008.
[24] Y. Larring, T. Norby, Protons in $LaErO_3$, Solid State Ionics 70/71 (1994) 305–310.
[25] C. Imawan, F. Solzbacher, H. Steffes, E. Obermeier, TiO_x modified NiO thin films for H_2 gas sensors: effects on TiO_x overlayer sputtering parameters, Sens. Actuators, B Chem. 68 (2000) 184–188.

Biographies

Xiaoxin Chen received the BS and ME degrees in the Department of Electrical and Computer Engineering from University of Utah, Salt Lake City, UT, in 2002 and 2004. She worked as a Teaching Assistant in University of Utah from 2002 to 2004, and as a Research Assistant in Chemical Engineering Department at the University of Utah from January 2003 to August 2003. From 2006, she has pursuing PhD in the Department of Electrical and Computer Engineering at the University of Utah. Her research interests include a high temperature humidity microsensors that based on the thin films of electrochemical materials (Y-doped $BaZrO_3$) and system integration.

Loren Rieth received his BS degree in Materials Science from The Johns-Hopkins University, Baltimore, MD, in 1994. He received his PhD in Materials Science and Engineering from the University of Florida, Gainesville, FL in 2001. From 2001 to 2003, he was a Postdoctoral Research Associate at the University of Utah, Salt Lake City, UT, and continued on at the University of Utah as a Research Assistant Professor in Materials Science (2003–2005), and Electrical and Computer Engineering (2004–present). His research is focused on deposition and characterization of thin film materials for sensors (chemical, physical, and biological), MEMS, BioMEMS, and energy production.

Mark S. Miller received the BS, in Electrical Engineering and Chemistry from Colorado State University, Fort Collin, CO in 1985. He received his MS degree in Electrical engineering from the Colorado State University. He worked in NCR Microelectronics as an analog integrated Circuit Engineer in 1987, Fort Collins, CO. And he received his PhD at the University of California in Santa Barbara in 1993. Then he joined as a Postdoctoral Research Associate in the department of Solid State Physics at the Lund University from 1993–1997. From 1997 to 2000, he worked as an Assistant Professor in the ECE Department at the University of Virginia and started Terahertz Device Corporation. In 2001, he worked as the Director of the Microfabrication Laboratories and an Assistant Professor in both department of ECE and MSE at the University of Utah. Currently, he is a Research Associate Professor at the University of Utah. His research work is mainly focused on investigating new optical and electrical devices that range from increasing the capacity or function of information technology systems to detecting biochemical molecules to producing new power sources.

Florian Solzbacher received his MSc in electrical engineering from the Technical University Berlin in 1997 and his PhD from the Technical University Ilmenau in 2003. He is Director of the Utah Nanofabrication Laboratory, Co-Director of the Utah Nanotechnology Institute, Director of the Microsystems Laboratory at the University of Utah and a faculty member in the Departments of Electrical and Computer Engineering, Materials Science and Bioengineering. He is also responsible for the Utah branch office of the Fraunhofer IZM, Germany. Dr. Solzbacher is co-founder of several companies such as First Sensor Technology, an established supplier to the automotive and process control industry and Blackrock Microsystems (www.blackrockmicro.com). He was Chairman of the German Association for Sensor Technology AMA from 2001 to 2009. His work focuses on harsh environment microsystems, sensors and materials. He is author of over 60 scientific and engineering publications and book chapters on MEMS devices, technologies and markets for Harsh Environments. Since 2004 he has been Chairman of Sensor + Test, the world's largest international trade fair and ensemble of conferences for sensors, metrology and testing.

CHAPTER 6

FAST HIGH TEMPERATURE HUMIDITY SENSORS BASED ON Y-DOPED $BaZrO_3$ THIN FILMS BY PULSED LASER DEPOSITION

6.1 Abstract

Y-doped $BaZrO_3$ ($BaZr_{1-x}Y_xO_{3-y/2}$, x = 0.2, y > 0) or YBZO 30 nm and 50 nm films were deposited by pulsed laser deposition (PLD) to investigate their reliability for long term humidity microsensors at high temperature (T ≥ 600°C) as required for power generation emissions controls. Previously published results on PLD 200 – 500 nm thin film samples indicated that this material was suitable for high temperature humidity measurements with fast and highly selectivity due to defect chemistry [1]. Humidity sensitivity and response time improved with reducing film thickness. To test this hypotheis, 30 nm and 50 nm thin film samples were deposited and characterized to allow extrapolation [1].

X-ray photoelectron spectroscopy (XPS) data were collected from as deposited samples at the surface as well as after 1 min and 4 min of Ar^+ etching. Both samples were Ba deficient but otherwise close to the desired stoichiometry. X-ray diffraction (XRD) reflections from as-deposited films show that the material is polycrystalline when deposited at substrate temperatures of 800°C. Atomic Force Microscopy (AFM) results revealed that both samples have a particle size of 19 to 25 nm and a surface roughness close to the material lattice constant of 4.2 Å. Transmission electron microscopy (TEM) data confirmed the particle sizes within 4 - 9% variation of the AFM data. The film conductivity increases as a function of temperature and upon exposure to a humid atmosphere, supporting our hypothesis of protons dominating conduction from 200 to 650°C. Humidity measurements were presented for both 30 nm and 50 nm films from 600 to 650°C at vapor pressure of 0.116 atm. Sensitivities up to 29 atm^{-1} and 18 atm^{-1} for 50 nm films at 0.116 atm partial pressure of water were measured at 600 and 650°C,

respectively. The sensor response time (τ_{90}) of both samples is reduced by a factor of 2-5 times compared to 200 – 500 nm thick PLD films [1].

KEYWORDS: Thin films, humidity, high temperature, Y-doped $BaZrO_3$ material, PLD, ionic conductor.

6.2 Introduction

Fossil fuel power plants are major emitters of greenhouse gases, which may have been one of the causes for global warming over the last 50 years [2]. With global power demands anticipated to rise more than 60% by 2030 and the number of active coal plants worldwide exceeding 50,000 current estimates predict that fossil fuels will account for 85% of the energy market by 2030 [3]. Power generation using fossil fuels generally requires a high temperature ($T \geq 500°C$) combustion process and result in the release of byproducts (including CO, CO_2, H_2O, H_2S, N_2, H_2S, and SO_2) whose discharge to the atmosphere is undesirable. Micro gas sensors are being developed to help monitor and control emissionsin advanced combustion process and engine management. In order to accurately measure a large variety of gaseous species and concentrations, the reliable measurement of water vapor is essential since the water vapor can have a huge impact on the accuracy of other gas measurements at high temperature [4].

Y-doped $BaZrO_3$ has demonstrated high selectivity to humidity in both bulk and thin films [1, 5-7]. However, the maximum humidity sensitivity of 7.5 atm^{-1} was measured for pulsed laser deposited (PLD) thin films at 400°C, which is one order of magnitude lower than that of sputtered Y-doped $BaZrO_3$ thin films [5]. Also, the sensor response time is slower compared to the sputtered samples [8]. Literature has reported that water vapor diffusion into bulk samples (with thicknesses t in the mm range) is about

two orders of magnitude slower than the surface exchange mechanisms that occur in the surface sensitive layers for thinner films ($t \leq 150$ μm) [6]. Considering these data and the observed increase in sensitivity and reduction in response time with reduced film thickness in both PLD and sputtered films a further reduction of the PLD film thickness should lead to improved sensor performance [1, 5].

This work presents 30 and 50 nm thick PLD Y-doped $BaZrO_3$ thin films for fast and high temperature humidity sensor applications, allowing the potential mitigation of the above stated drawbacks of thicker PLD films while maintaining the advantageous long term stability and humidity sensing characteristics of the films.

6.3 Theoretical basis

High temperature proton conductor exhibit appreciable protons when exposed to H_2O or $H_2 + H_2O$ containing atmospheres at elevated temperature (typically $T \geq 500°C$) [5-7]. Y-doped $BaZrO_3$ can exhibit oxygen ions or oxygen vacancies when doped with a lower valence ion e.g., Y^{3+} on the Zr^{4+} sites. The defect reaction for oxygen incorporation into the lattice in a dry atmosphere using the Kröger-Vink notation is

$$½\ O_2\ (g) + V_o^{\bullet\bullet} \leftrightarrow O_o^x + 2h^{\bullet}, \tag{6.3.1}$$

where $V_o^{\bullet\bullet}$ denotes an oxygen vacancy, O_o^x denotes an oxygen ion on its own sublattice and $h^{\bullet}$ denotes an electron-hole. When exposing to water vapor containing atmosphere at high temperature, it can absorb water into the lattice structure and become a proton conductor. The relevant defect reaction is

$$H_2O\ (g) + V_o^{\bullet\bullet} + O_o^x \leftrightarrow 2\ (OH)^{\bullet}_O. \tag{6.3.2}$$

Oxygen ions, protons, electrons, and electron-holes contribute the total conductivity of YBZO when expose to humidity. A thorough characterization of partial conductivity of the various transporting species has been studied and can be fitted to a reasonable defect model [9-13]. Based on the defect chemistry, the total conductivity is

$$\sigma_{total} = \sigma_{ionic} + fp_{O2}^{1/4} \tag{6.3.3}$$

where σ_{total} is total conductivity, σ_{ionic} is contributed from oxygen ions and protons. σ_{total} as a function of $p_{O2}^{1/4}$ at a fixed temperature should provide a linear reaction [6]. However, the results from Y-doped $BaZrO_3$ bulk materials indicated the underestimate of proton conduction [6].

6.4 Experimental methods

Y-doped $BaZrO_3$ of 30 and 50 nm films were deposited onto oxidized 2 inch n-type (100) silicon substrates using PLD at substrate temperatures of 800°C in a vacuum ambient with base pressure at 6 x 10^{-7} Torr. Films were characterized using X-Ray Photoelectron Spectroscopy (XPS), X-Ray Diffraction (XRD), Atomic Force Microscopy (AFM), and Transmission electron microscopy (TEM) to determine film composition, microstructure, surface morphology, and particle size. Electrical conductivity as a function of temperature and water vapor humidity sensing characteristics of the films were measured up to 650°C. Silicon based gas sensor test structures with Cr (20 nm) and Au (180 nm) thin film metallization deposited on top of the sensing material were fabricated for humidity tests as previously published [5]. The size of each sensor is 7x7 mm^2. It uses 10 pairs of interdigitated electrodes (IDE) spaced 100 μm apart and includes a resistive thin film heater, a resistive temperature device (RTD), and the sensitive layer.

6.4.1 Characterization of film composition and structure

The electroceramic thin films were deposited by PLD from a 1 inch diameter, 99.9% pure ceramic $BaZr_{0.8}Y_{0.2}O_{2.9}$ pure ceramic target (Process Materials Inc). The films were grown at 50 Hz, 250 mJ/pulse laser energy with average energy flux of 1 J/cm^2, yielding a film thickness uniformity of ± 25%. Films with a center thickness of 30 nm and 50 nm were deposited. Thicknesses were verified using a Woolam V-Vase spectroscopic ellipsometer. X-ray photoelectron spectroscopy (XPS) measurements were made using a Kratos Axis ULTRA^{DLD} system using monochromatic Al Kα radiation. Composition data was recorded for as received samples and after 1 min and 4 min of Ar^+ ion beam etching. X-ray diffraction (XRD) measurements were made using a Philips X'Pert system using Cu Kα radiation in the Bragg-Brentano geometry for 2θ angles from 10 - 90 °. Atomic force microscopy (AFM) micrographs were collected with a Veeco Dimension 3000 system using etched Si tapping mode tips with a nominal tip radius of ~ 5 nm. Transmission electron microscopy images (TEM) were collected with a Tecnai F 30 to confirm the particle sizes.

6.4.2 Water vapor sensitivity measurements

The water vapor sensing characteristics for PLD $BaZrO_3$:Y thin films were measured using a custom-built gas sensor test station. Sample chips were placed on a heater in a stainless steel chamber and contacted with probe needles attached to a PC/labview controlled Keithley digital multimeter in voltage measurement mode. N_2 carrier gas at 200 sccm was passed through a water bath at 80°C, saturating the gas at 0.468 atm water vapor pressure. Before the saturated water vapor reaches the test chamber, it is diluted with about 610 sccm N_2 gas, which gives 0.116 atm partial pressure

of water. Once the test gas enters the test chamber it is heated to the sensor operating temperature. The partial pressure of water vapor is calculated by the percentage of total gas flow at 1 atm.

Sample resistance values were determined based on the voltage measurements using a 0.7 μA supply current that would not lead to self heating of the film. The temperature dependence of resistance was measured at 200 to 650°C. The responses to water vapor were measured at 0.116 atm partial pressure of water at 600 and 650°C. The film conductivity was determined using

$$\sigma = \frac{L}{RAn} \tag{6.4.1}$$

where σ is the film conductivity ([σ] = 1 S/cm), R is the measured resistance ([R]=1 MΩ), A is the cross sectional area of the sample ([A]=1 cm^2), L is the distance between each interdigitated electrode ([L]=1 cm), and n is the number of interdigital electrode structure (IDE) pairs (n=10).

6.5 Results and discussion

6.5.1 Film characterization

The chemical composition of the films was measured by XPS from as received samples, and after ion beam etching. The film compositions were quantified from the spectra and are summarized in Table 6-1. XPS data indicate that PLD samples are closer to nominal composition than sputtered samples. However Ba is still deficient in both cases. We are providing data after 1 min and 4 min of Ar^+ etching. After 1 min etching, there is still a

Table 6-1: Film composition quantified by XPS measurements for samples as function of thickness for (a) nominal composition, and deposited at 800˚C with film thickness of (b) 30 nm, and (c) 50 nm.

	AT concentration (%)								
Sample name		Ba 3d	O 1s	Sn 3d	Zr 3p	Y 3p	C 1s	Ar 2p	Si 2p
a		20	60	0	16	4	0	0	0
b	As received	3	34.3	0.3	10.5	5.4	46.6	0	0
	1 min Ar^+ etching	10.8	55.5	0	10.2	5.1	18.4	0	0
	4 mins Ar^+ etching	1.6	44	0	6.6	2.8	0	3.7	41.3
c	As received	4	39	0.4	12.8	5.5	38.3	0	0
	1 min Ar^+ etching	13.1	50.6	0	12.4	5.4	13.9	4.6	0
	4 mins Ar^+ etching	1.8	42.2	0	12.2	5.3	0	3.7	34.8

significant amount of carbon incorporated into the films. The substrate layer can be observed after 4 min of Ar^+ etching.

XRD reflections were collected to investigate the microstructure of the deposited films, and are presented in Fig. 6-1. The reflections are for as–deposited PLD samples with substrate temperature of 800°C with film thickness from 30 to 500 nm. The $BaZrO_3$ reflections were present indicating the films were polycrystalline in character. The dashed vertical lines on the plots represent the JCPDS values for $BaZrO_3$ with one weak reflection for (110) $BaZrO_3$ for 50 nm thick samples, but not on 30 nm films.

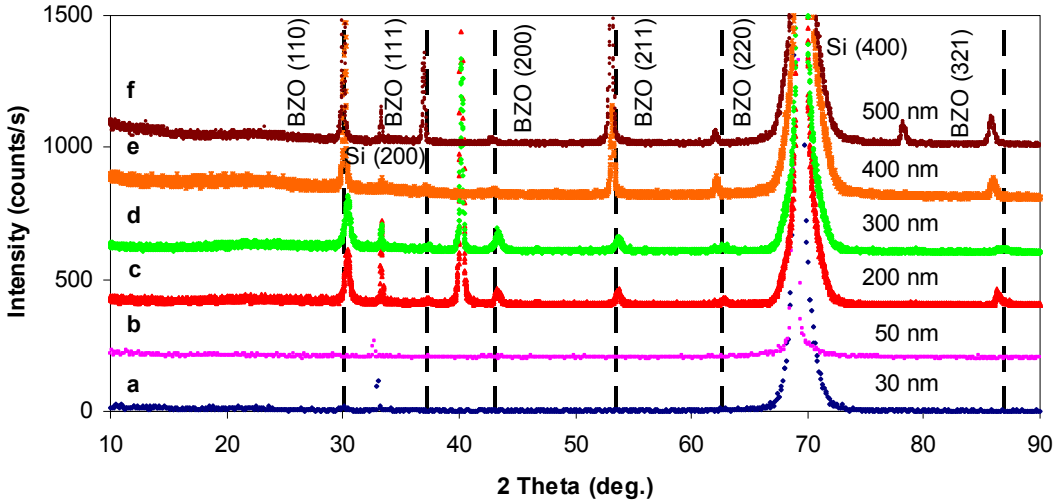

Fig. 6-1: X-ray diffraction reflections collected from as-deposited PLD samples at a base pressure of 6 x 10^{-7} Torr with substrate temperatures at 800°C with film thickness: a. 30 nm, b. 50 nm, c. 200 nm, d. 300 nm, e. 400 nm, and f. 500 nm [c-f from Ref 1].

The reflection intensity appears to increase with increasing film thickness. These reflections are shifted to higher 2θ values compared to the JCPDS database, which would be consistent with the films being under tensile stress. These results are also consistent with the presence of the (200) Si peak, a normally unallowed peak, which appears due to strain in the Si substrate. A Philips X'Pert data collector was used to measure the full width half max (FWHM) values of these reflections which were decreasing with increased film thickness. The results are in agreement with trends observed in previous data for thicker films (Fig. 6-2).

AFM was used to characterize the surface morphology of as deposited PLD films. AFM micrographs for both samples have a similar surface morphology consisting of nano-scale surface particles. For each film thickness, 6 individual measurements were made using a stereological technique and averaged.

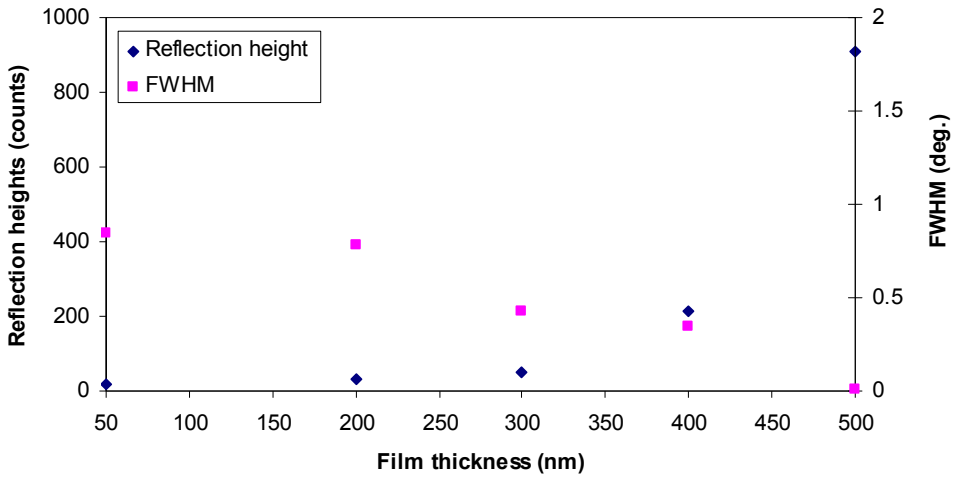

Fig. 6-2: Reflection heights versus film thickness for Y-doped $BaZrO_3$ PLD films with substrate temperature of 800°C, and full width at half maximum (FWHM) versus film thicknesses for PLD films with substrate temperature of 800°C.

The results in Fig. 6-3 show that RMS roughness increased from 0.4 nm to 1.2 nm and particle size increased from 19 nm to 72 nm with film thickness from 30 nm to 500 nm [1]. The AFM data presented in Fig.6-3 indicate that all PLD samples have a surface roughness close to the $BaZrO_3$ lattice constant of about 4.2 Å. The observed particle size is 19 nm and 25 nm for 30 nm and 50 nm thick samples, respectively.

The particle size increases with increasing film thickness, which is consistent with previous results from 200 – 500 nm thick films [1]. TEM data were collected to confirm the particle size of Y-doped $BaZrO_3$ thin films. Fig. 6-4 presents TEM images of a) 30 nm and b) 50 nm PLD films deposited at a substrate temperature of 800°C in vacuum.

TEM data indicate a particle size of between 17 nm and 25 nm for 30 nm films, and between 20 nm and 26 nm for 50 nm films. This constitutes a difference of 4% to 9% compared to the AFM measurements and confirms that the stereological technique gives a reasonable approximation of the particle size.

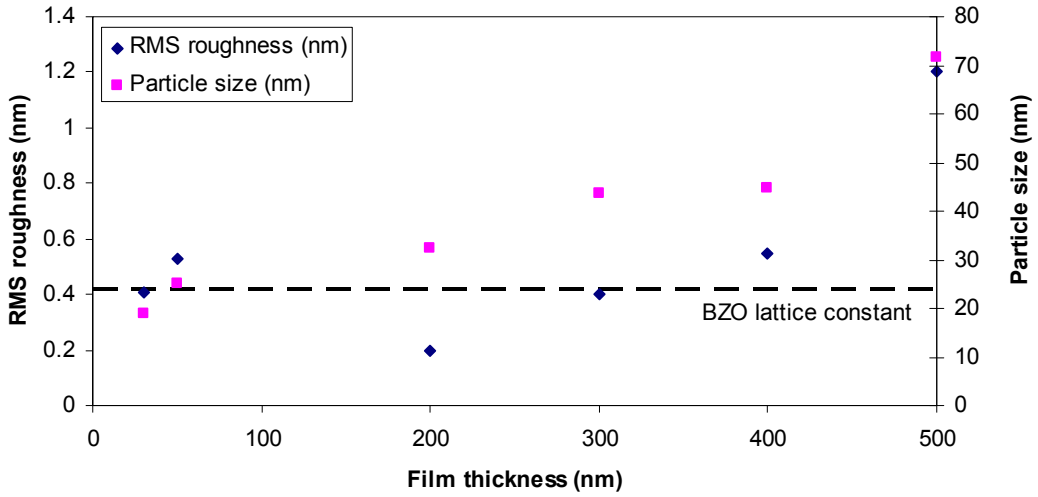

Fig. 6-3: RMS roughness and particle size versus film thickness for Y-doped $BaZrO_3$ for as deposited PLD films with substrate temperature of 800°C.

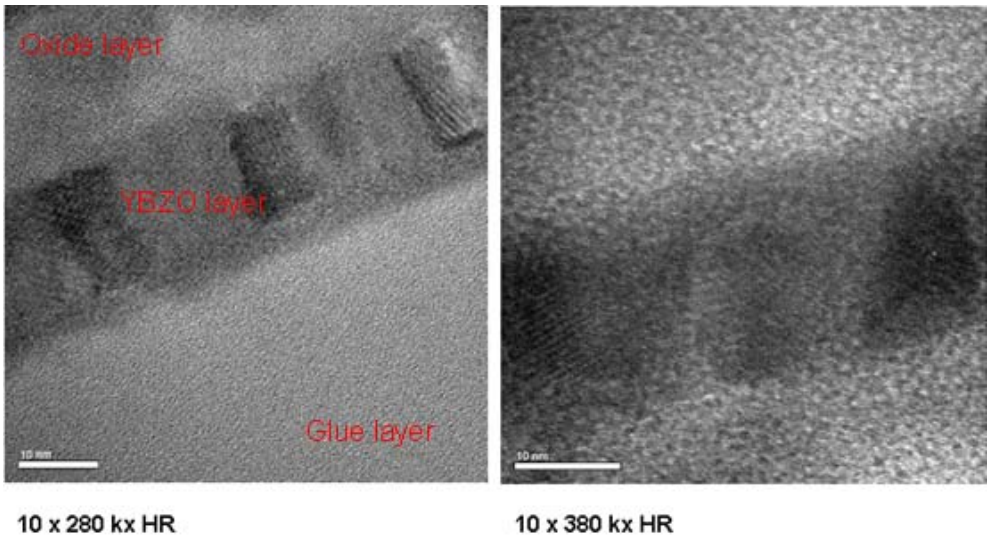

(a) (b)

Fig. 6-4: TEM images for PLD films at substrate temperature of 800°C in vacuum with thickness of (a) 30 nm and (b) 50 nm.

6.5.2 Temperature dependence

The sensor conductivity as function of temperature was characterized from 200 to 650 °C to determine the variation of base line resistance with temperature during humidity measurements and to gain information on potential electrical conduction mechanisms in the material.

The conductivity of the samples increases exponentially with increasing temperature (Fig. 6-5). This relation can be described as [14-15]:

$$\sigma_t = \sigma_0 e^{-\frac{E_a}{kT}} \tag{6.4.1}$$

where σ_t is the conductivity as function of temperature in S/cm, σ_0 is the conductivity at 473 K (i.e. the lowest temperature at which we were able to get measurable conductivity values) in S/cm, E_a is the activation energy in eV, and k is Boltzmann's constant (8.617385×10^{-5} eV/K). The activation energy was calculated based on approximate linear fits in the log-plot of film conductivity versus temperature (200 - 650°C) in N_2 ambient gas at a flow of 1380 sccm. Using a linear approximation for the slope, two distinct temperature regions can be identified with different slope. This change in activation energy can be interpreted as a change in electrical conduction mechanism. Based on the activation energy presented in Fig. 6-5, all PLD samples exhibit an activation energy that is increasing with increased film thickness for both temperature and conduction mechanism ranges. Above ca. 350 - 650° C, activation energies of between 0.2 and 0.47 eV were observed, consistent with literature that suggest a predominantly O^{2-} ion based conduction mechanism (defect/vacancy hopping) with activation energy values of between 0.3 and 1.2 eV [23].

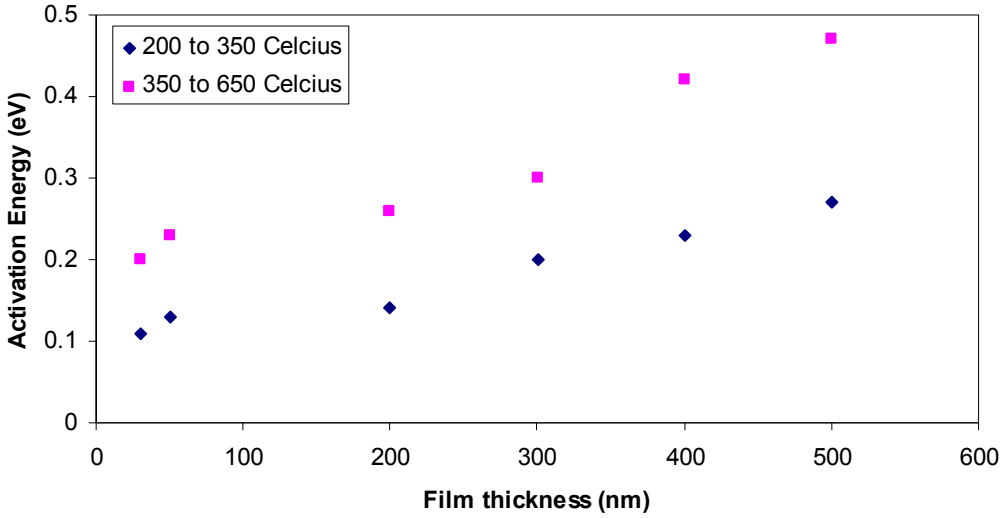

Fig. 6-5: Activation energy (E_a) versus film thickness from 30 nm to 500 nm PLD films [8]. Two distinct regions of activation energies are apparent in original data. Activation energy was generated based on approximate linear fits in the log-plot of film conductivity versus temperature (200°C - 650°C) in N_2 ambient gas at a flow of 1380 sccm. This is consistent with the conduction mechanism of Y-doped $BaZrO_3$ (electron-hole and O^{2-} conductions) presented in literature [16-22]. Below 350° C, activation energies of 0.11 – 0.27 eV were determined, consistent with electron/hole based conduction (0.18 to 0.39 eV) [24].

6.5.3 Water vapor response

All samples are initially exposed to dry N_2 gas. Then, water vapor is introduced into the test chamber. Once the electrical conductivity has stabilized, the atmosphere is changed back to dry air. As expected, the conductivity increases when exposed to water vapor [1, 5-7]. The samples were measured at partial pressures of water of 0.116 atm at temperatures of 600°C and 650°C (Fig. 6-6). Film sensitivity as stated below is calculated based on:

$$S = \frac{(\sigma_g - \sigma_0)}{(\sigma_0 \times \Delta C)} \qquad (6.4.2)$$

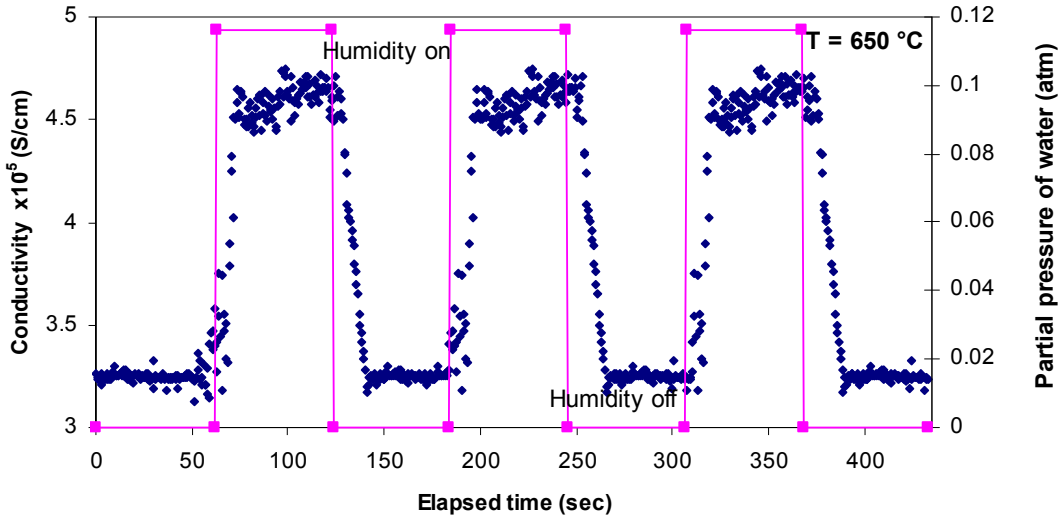

(a)

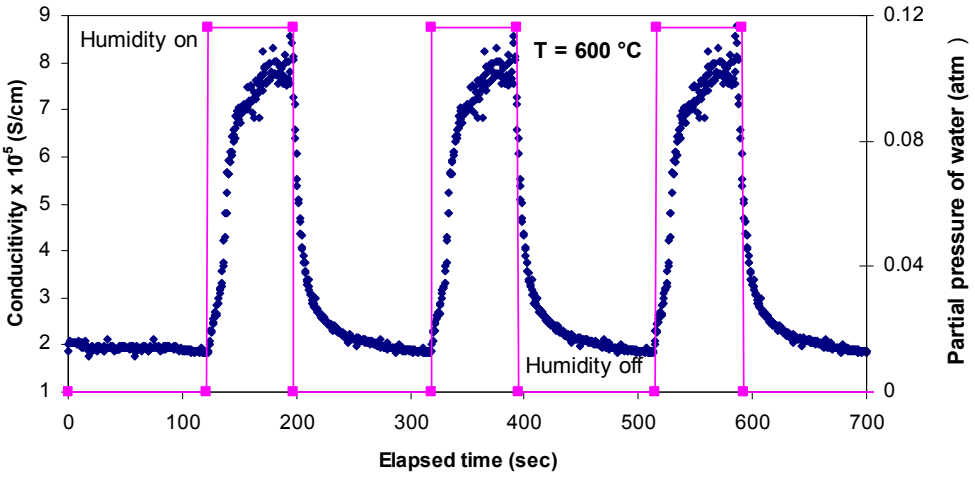

(b)

Fig. 6-6: Water vapor response of Y-doped $BaZrO_3$ thin films at a partial pressure of water of 0.116 atm for (a) 30 nm at 650°C, (b) 50 nm at 600°C, and (c) 50 nm at 650°C.

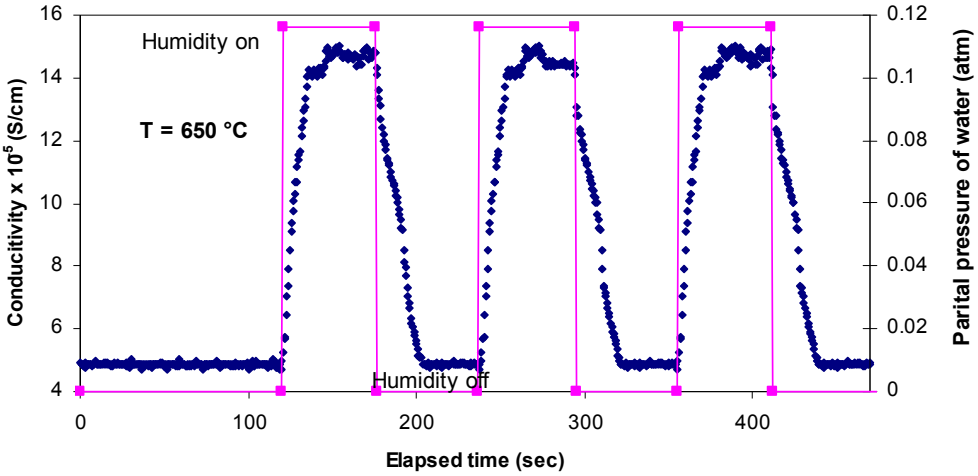
Humidity on
T = 650 °C
Humidity off
Conducitivity x 10^-5 (S/cm)
Parital pressure of water (atm)
Elapsed time (sec)
16
14
12
10
8
6
4
0.12
0.1
0.08
0.06
0.04
0.02
0
0
100
200
300
400

(c)

Fig. 6-6: (Cont.)

where S is the sensitivity in atm^{-1}, σ_g is the conductivity upon exposure to humidity at a given temperature T, σ_0 is the initial conductivity without humidity exposure at the same temperature. ΔC is the change in partial pressure of water in atmosphere. Sensitivities up to 4.2 atm^{-1} were measured for 30 nm films at 650°C. Sensitivities up to 29 atm^{-1} and 18 atm^{-1} were measured for 50 nm films at 600°C and 650°C. Measurements at both temperatures were carried out at a water partial pressure of 0.116 atm. No repeatable humidity measurements could be recorded: 1) below 650°C for 30 nm samples, and 2) below 0.116 atm of partial pressure of water for both 30 nm and 50 nm samples.

The humidity sensitivities at 650°C are 4.2, 18, 1, 0.6, 0.3, and 0.2 atm^{-1} for corresponding film thicknesses of 30, 50, 200, 300, 400, and 500 nm (Fig. 6-7). The humidity sensitivity for 30 and 50 nm films is significantly higher than for thicker samples, supporting our hypothesis of increasing humidity sensitivity with reducing film thickness.

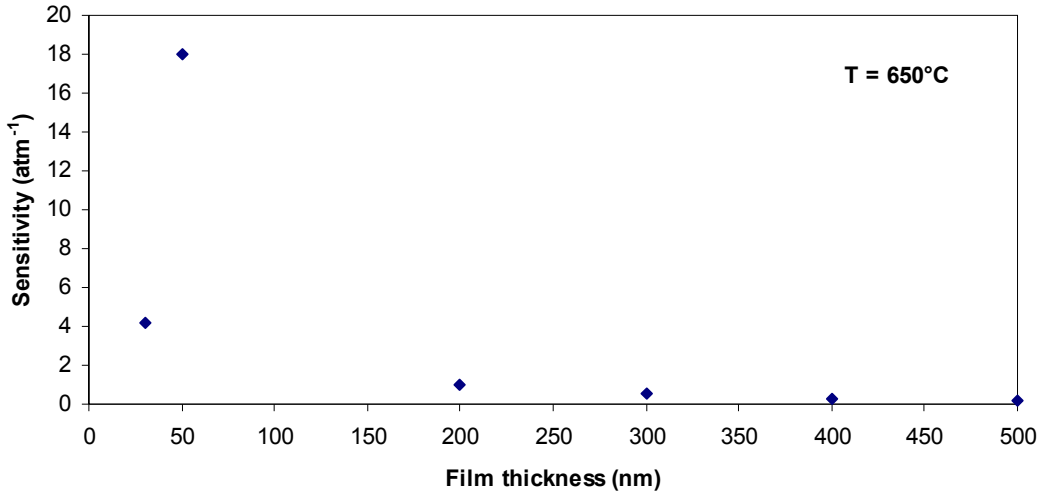

Fig. 6-7: Water vapor sensitivity as a function of film thickness for 30 - 500 nm of Y-doped $BaZrO_3$ PLD thin films in 0.116 atm partial pressure of water at 650˚C.

This behavior indicates that more defects which allow absorption of H_2O into the lattice and increase conductivity may exist in the surface layers than in the material bulk. The observed behavior could be modeled by two parallel resistors: one for a changing humidity sensitive top layer and one for a humidity independent base layer. Assuming such a model, the sensitivity of the entire film would increase with decreasing film thickness up until the film thickness is as thin as the sensitive top layer as indicated above. Literature also states that surface exchange and diffusion tend to be faster than bulk diffusion. Hence the subsequent higher mobility would further the increase in conductivity and response. Both, increased absorption due to higher defect density at the surface and faster ionic surface exchange will likely contribute to the overall sensor response.

As observed in multiple samples, the humidity sensitivity for 50 nm is consistently higher than that for 30 nm films, which could potentially indicate a change in trend or mechanism. Reasons for this change could lie in the technical challenges in contacting such a thin layer of sensitive film or in the beginning dominance of scattering effects for charge carriers at the interface between sensitive layer and substrate and at the top surface. Further investigations will need to focus on the cross sections and chemical compositions for the 30 nm films after the humidity measurements.

6.5.4 Sensor response time

In previous publications [1, 5, 8], we had discussed that H_2O molecules dissolving into the lattice would lower the oxygen vacancy concentration and release protons into the material in the presence of water vapor at high temperatures. We have characterized and correlated the response and the recovery times of the sensors and the film thickness

at operating temperature of 600 and 650°C at partial pressures of water of 0.116 atm as deposited (Fig. 6-8). The response time and recovery time are defined as the time required for the conductivity of the sensor element to reach 90% of the equilibrium value following a step increasing in water vapor concentration and the time required for the conductivity of the sensor to drop 90% of the base conductivity [16].

The sensors response recovery times appear to increase with increasing film thickness at both operating temperature of 600 and 650°C. For 30 nm and 50 nm films, the time constant (τ_{90}) is a factor of 2 – 5 times faster than other PLD samples. A possible explanation for the faster sensor response could lie in the surface ion exchange becoming the dominating ions transfer mechanism instead of a bulk diffusion mechanism.

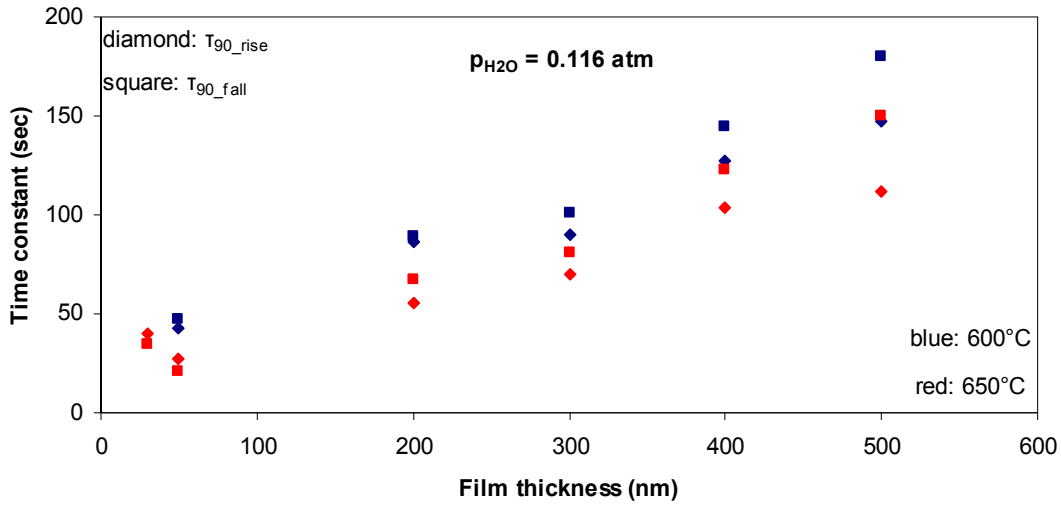

Fig. 6-8: Response and recovery times of the sensor element to reach or drop by 90% of the conductivity as a function of film thickness at 0.116 atm partial pressure of water at operating temperature of 600 and 650°C.

6.5.5 Stability

Life-time of the sensors is a major factor in evaluating the stability of the films and sensors and thus their relevance for future applications. We have recently presented long term stability for selected PLD films in excess of 52 weeks [1]. In an attempt to replicate typical user scenarios, we stored 30 and 50 nm PLD humidity sensors in gel-pac boxes at room temperature in the Utah Nanofabrication Laboratory clean room upon completion of the initial test runs. The sensors were then retested under identical conditions at regular time intervals. For each test cycle, the sensors were first placed into the test chamber while exposing them to dry N_2 gas at 1380 sccm while ramping up to 650°C for 2 hours to stabilize the initial electrical conductivity of the material. Then water vapor was introduced into the test chamber with between 0 and 0.116 atm of partial pressure of water. Once the electrical conductivity values have stabilized, the atmosphere is changed back to dry N_2. Fig. 6-9 illustrates the change in sensitivity and base resistivity of the 30 and 50 nm PLD humidity sensors over a period of 24 weeks with the corresponding film base resistivity as an indicator of sensor stability. The sensitivity of the 30 nm films dropped from 4.2 atm^{-1} to 0 atm^{-1} in 16 weeks. The resistivity however remained stable until the 24^{th} week. Fifty nm films retain stable sensitivity and resistivity throughout the 24-week time period. The shift in sensitivity observed in the 30 nm films may be caused by a change in film composition or structure, which however does not affect the baseline resistivity. This may further support that the sensing mechanism takes place in the surface layers of the film only, dominating the electrical conductivity at high temperatures and during humidity exposure.

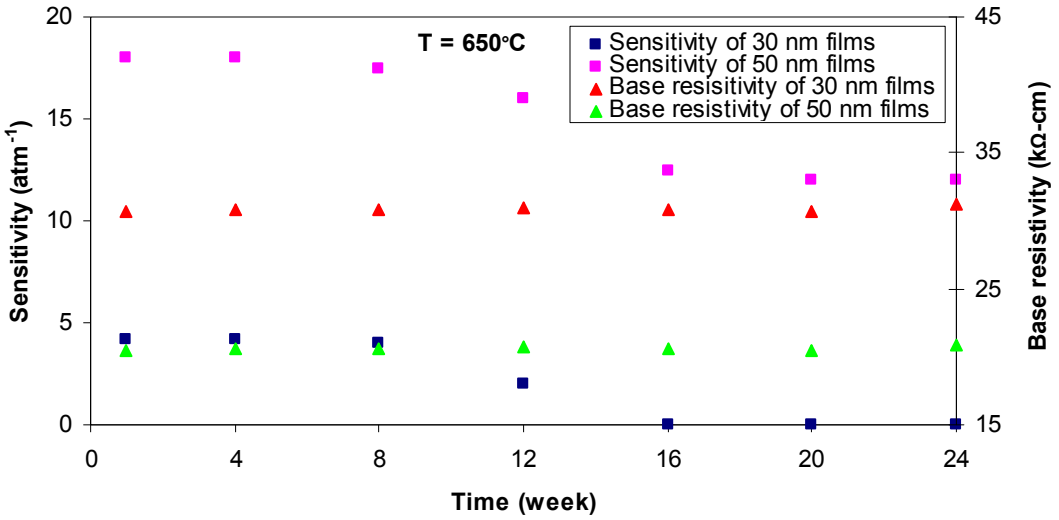

Fig. 6-9: Humidity sensor stability test for 30 nm and 50 nm thick PLD films over a 24 week period.

Without water vapor, the "bulk" of the film dominates the electrical properties. This hypothesis is supported by other literature on bulk Y-doped BZO that suggests surface or surface layer effects to be responsible for changes in electrical conductivity [6]. Upon complete failure of the device, we will analyze the chemical composition, structure and texture of the films again and compare with the initial measurements prior to the long term test in order to test for changes due to humidity exposure that can explain the drop in resistance.

The stability results in Fig. 6-9 clearly show an aging effect of the humidity sensors over time. The humidity sensitivity and base resistance of the 30 and 50 nm PLD films remain comparably stable under the harsh testing conditions and high temperatures for more than 6 months. Regular recalibration or high temperature cleaning routines of the sputtered film did not recover the film sensitivity.

6.6 Conclusion

The correlation between film thickness and sensor sensitivity and response time for Y-doped $BaZrO_3$ PLD samples with film thicknesses between 30 and 500 nm was studied. With the purpose of improving sensor sensitivity and response for PLD films beyond comparably faster sputtered films, data from previous experiments were analyzed for trends. Data showed that with decreasing film thickness, improved sensitivity and response time could be observed. Current understanding of the electrical conduction and sensing mechanisms appear to indicate that surface exchange and diffusion in this material system are faster than the bulk mechanisms and that there is a higher density of defects that can facilitate the sensing mechanism. To test the hypothesis new PLD samples were fabricated with 50 and 30 nm thickness (the lower limit for films that allowed reliable electrical measurements).

Films were deposited and tested as to their feasibility as thin film humidity sensing materials at high temperatures, similar to work previously published by us. XPS data showed that Ba is deficient in samples for both thicknesses. As deposited films with substrate temperature of 800°C were polycrystalline. The reflection counts were too low to be clearly visible for 30 nm thick films. Reflection intensity appeared to be increasing and FWHM was decreasing with increasing film thickness. This behavior was in agreement with our previous observations for 200 – 500 nm thick PLD films. AFM measurements show that as deposited films have low surface roughness similar in value to the BZO lattice constant. The particle size (19- 25 nm) as observed using AFM was confirmed by TEM measurements. The electrical conductivity was characterized using an IDE test structure over a temperature range of 200 - 650°C. The conductivity might have

contributions from electrons, electron-holes, and oxygen ions. The activation energies measured for these charge carriers appeared to be in accordance with data presented in literatures. The humidity sensitivity of the films was characterized as a function of partial pressure of water at 600 and 650°C. Both films exceed the trend and exhibit several factors (2-5) higher sensitivity and faster response than the thicker films at both operating temperatures. The sensitivity of 50 nm films is consistently higher than that of 30 nm films, which could potentially indicate a change in mechanism or technical challenges in contacting the thin film. This could be an indication that both surface exchange and bulk diffusion occur at the same time, with the surface ion exchange being the dominating ion transfer mechanism in the thinner layers. The 30 and 50 nm PLD films exhibited stable electrical/sensing properties for more than 6 months. In conclusion: reducing the thickness of PLD $BaZrO_3$ sensitive films to the low 10s of nm range increases sensitivity and reduces response time while maintaining the advantageous stability during high temperature humidity measurements. The behavior is in accordance with existing models explaining the impact of surface and bulk mechanisms on ionic conduction in this material group.

6.7 References

[1] X.X. Chen, L. Rieth, M.S. Miller, F. Solzbacher, Pulsed laser deposited Y-doped $BaZrO_3$ thin films for high temperature humidity sensors, Sens. Actuators, B Chem. 142 (2009) 166-174.

[2] Solomon, S., D. Qin, M. Manning, Z. Chen, M. Marquis, K.B. Averyt, M.Tignor, H.L. Miller (Eds.), IPCC, 2007: Summary for Policymakers. In: Climate Change 2007: The Physical Science Basis. Contribution of Working Group I to the Fourth Assessment Report of the Intergovernmental Panel on Climate Change, Cambridge University Press, Cambridge, United Kingdom and New York, NY, USA.

[3] http://en.wikipedia.org/wiki/Fossil_fuel_power_plant.

[4] R.K. Hanson, D.S. Baer, Multiplexed diode-laser gas sensor system for in-situ multispecies emissions measurements, Final report of national center for environmental research (1995).

[5] X.X. Chen, L. Rieth, M.S. Miller, F. Solzbacher, High temperature humidity sensors based on Y-doped $BaZrO_3$ thin films, Sens. Actuators, B Chem. 137 (2009) 578-585.

[6] W. Wang, A.V. Virkar, Ionic and electron-hole conduction in $BaZr_{0.93}Y_{0.07}O_{3-\delta}$ by 4-probe dc measurements, J. Power Sources 142 (2005) 1-9.

[7] W. Wang, A.V. Virkar, A conductimetric humidity sensor based on proton conducting perovskite oxides, Sens. Actuators, B Chem. 98 (2004) 282-290.

[8] X.X. Chen, L. Rieth, M.S. Miller, F. Solzbacher, Comparison of Y-doped BaZrO3 thin films for high temperature humidity sensors by RF sputtering and pulsed laser deposition, Sens. Actuators, B Chem. 148 (2010) 173-180.

[9] J.R. Frade, Theoretical behaviour of concentration cells based on ABO_3 perovskite materials with protonic and oxygen ion conduction, Solid State Ionics 78 [1995] 87.

[10] H-D. Baek, Modeling of electrical conductivity in high-temperature proton-conducting oxides, Solid State Ionics 110 [1998] 255.

[11] N.Bonanos, F.W. Poulsen, Structural and electrical characterisation of $SrCe_{1-x}Y_xO_\xi$, J. Mater. Chem. 9 [1999] 431.

[12] S.J. Song, E.D. Wachsman, S.E. Dorris, U. Balachandran, Hydrogen research for spaceport and space based applications, J. Electrochem. Soc. 150(6) [2003] A790.

[13] A.S. Patnaik, A.V. Virkar, Transport properties of potassium-doped BaZrO3 in oxygen and water vapor containing atmospheres, J. Electrochem. Soc. 153 (7) [2006] A1397-A1405.

[14] T. Ishihara, H. Matsuda, Y. Takita, Doped $LaGaO_3$ perovskite type oxide as a new oxide ionic conductor, J. Am. Chem. Soc. 116 (1994) 3801-3803.

[15] X.Y. Yu, G. Chen, Temperature dependence of thermophysical properties of GaAs/AlAs periodic structure, Appl. Phys. Lett. 67 (1995) 3554-3556.

[16] K.D. Kreuer, On the complexity of proton conduction phenomena, Solid State Ionics, vol. 149 (2000) 136-137.

[17] R. Glockner, M.S. Islam, T. Norby, Protons and other defects in BaCeO : a computational study, Solid State Ionics, vol. 122(1-4) (1999) 145-156.

[18] R.A. Davies, M.S. Islam, J.D. Gale, Dopant and proton incorporation in perovskite-type zirconates, Solid State Ionics, vol. 126 (1999) 323-335.

[19] H. Iwahara, T. Yajima, T. Hibino, K. Ozaki, H. Suzuki, Study on current efficiency of steam electrolysis using a partial protonic conductor $SrZr_{0.9}Yb_{0.1}O_{3-\alpha}$, Solid State Ionics, vol. 61 (1993) 65-69.

[20] T. Yajima, H. Iwahara, Defect structure analysis of B-site doped perovskite-type proton conducting oxide $BaCeO_3$ Part 1: The defect concentration of $BaCe_{0.9}M_{0.1}O_{3-\delta}$ (M = Y and Yb) Solid State Ionics, vol. 53-56 (1992) 983-988.

[21] T. Scherban, A.S. Nowick, Protonic conduction in Fe-doped $KTaO_3$ crystal, Solid State Ionics , vol. 53-56 (1992) 1004-1008.

[22]Y. Larring, T. Norby, Protons in $LaErO_3$, Solid State Ionics, vol. 70/71 (1994) 305-310.

[23] A.S. Nowick, Y. Du, High-temperature protonic conductors with perovskite-related structures, Solid State Ionics, vol. 77 (1995) 137.

[24] W. Wang, A.V. Virkar, Determination of ionic and electronic conductivities of $Ba_3Ca_{1.18}Nb_{1.82}O_{9-\delta}$ (BCN 18) in dry and wet atmospheres, J. Electrochem. Soc. 151 (10) (2004) 1565-1571.

CHAPTER 7

SUMMARY, CONCLUSION, AND FUTURE WORK

The main objective of this dissertation was to develop, fabricate and investigate Y-doped $BaZrO_3$ thin films for the use in microfabricated high temperature humidity sensors. We have found that this material is suitable for fast and stable high temperature humidity sensors that are selective to water vapor in power plants and automotive exhaust gas streams applications. In this chapter, we summarize our work that covered material studies, device and process technology development, and sensor response characterization. We also draw several principal conclusions that help further the understanding of the material and its use in this sensing application, as described in Section 7.2 below. Finally, we give some recommendations for future work.

7.1 Summary

We have developed deposition processes using sputtering and pulsed laser deposition (PLD) for Y-doped $BaZrO_3$ thin films for high temperature humidity measurements. In total, 212 thin film layers (200 sputtered and 12 PLD layers) were deposited and characterized. Out of these, 100 sputtered and 12 PLD layers were used in sensor devices.

Major effort went into developing the process parameters for deposition and the characterization of these thin films. Y-doped $BaZrO_3$ thin films with thicknesses of between 200 and 750 nm were sputtered onto oxidized 2 inch n-type Si wafers at room temperature from a ceramic target in an Ar sputtering ambient. Various deposition pressures (0.45 – 50 mTorr) and deposition powers (50 – 300 W) were used in order to understand the correlation between process parameters and film properties. Films were annealed at 800°C and 1000°C for 3 hours in air. The resulting films were characterized using X-ray photoelectron spectroscopy (XPS), X-ray diffraction (XRD), and Atomic

force microscopy (AFM) to determine their film compositions, microstructure, and surface morphology. PLD samples (30 – 500 nm) were deposited onto identical substrates at various substrate temperatures (RT - 800°C) in a VAC PLD system. All PLD samples were characterized as deposited. Selected PLD samples were also annealed at 1000°C for 3 hours in air and characterized again. Transmission electron microscopy (TEM) was used to confirm the particle sizes of 30 and 50 nm PLD films with AFM technique.

We identified Ba deficiencies in all deposited layers for both deposition methods. Sputter deposition appeared to have smaller process windows for closer stoichiometric compositions of 20 wt% Y- doped $BaZrO_3$ thin films with better sensitivity responses than PLD films. Film cracking appeared after annealing in most deposited thin films. This may be caused by either the tetragonal to monoclinic transformation of ZrO_2 due to the Ba deficiency, or the films being under tensile stress that was confirmed by XRD reflections and film stress studies before and after annealing. XRD reflection results revealed that reflection heights were increasing and full width half max (FWHM) was decreasing with increasing film thickness. PLD films appeared to have a more pronounced $BaZrO_3$ (BZO) structure than sputtered films. All deposited layers exhibit smooth surface roughness that is close to the BZO lattice constant (about 4.2 Å) and small particle sizes that seemed to increase with increasing film thickness. The particle sizes of the films were determined by AFM and TEM between 19 and 72 nm. A 4 – 9% variation between the TEM and AFM results were observed.

The first 25 sensor devices using sputtered films had the sensing material deposited on top of the interdigitated test structure (IDE) and showed no response to

humidity. The rest of the sensors were fabricated with the IDE on top of the sensitive material, yielding varying degrees of sensitive response. Another 25 sensors with sputtered films used Ti/Pt as metal contacts for humidity measurements, resulting in unstable and/or unrepeatable humidity response. The 50 remaining sensor devices using sputtered films as well as the 12 of PLD sensor devices used Cr/Au as IDE on top and produced fast, sensitive, selective, and long term stable humidity response. Therefore, Cr/Au appears to be recommendable choice for the use as metal contact materials for repeatable and stable humidity sensor responses, thereby limiting the operating temperature to below 1000°C. The film baseline resistivity was characterized as a function of film thicknesses and temperature to estimate the activation energies for the various electrical conduction mechanisms and to determine the types of charge carriers. Two distinct regions of activation energies were apparent in the electrical conductivity measurements, consistent with our expectations that electrons and electron-holes were the primary charge carriers at lower temperature ($T \leq 500$°C), and oxygen ions were the primary charge carriers at high temperature (500 - 650°C) prior to exposure to water vapor at high temperature. The activation energies seemed to increase with increasing film thickness in both temperature regions. The resulting activation energies for the sputtered samples were only slightly larger than PLD samples at lower temperatures (200 - 500°C) and much larger at higher temperature (500 - 650°C).

Y-doped $BaZrO_3$ thin film humidity sensors were tested towards humidity and typical mixed combustion gases to demonstrate its high sensitivity and selectivity to water vapor at high temperature. The sensitivity towards water vapor is at least one order of magnitude higher than towards other gas species. The humidity sensitivity appeared to

be increasing with decreasing film thickness down to 50 nm thick PLD films. The sensor devices were recorded as being 4 – 20 times faster in sensor response (τ_{60}) than other humidity sensor devices as discussed in Section 1.3 (Fig. 7.1). The time constant of the sensors decreased with decreasing film thickness. Long term stability and life time testing showed that the sensor devices were able to operating functionally in excess of 52 weeks of time, indicating usefulness for real world applications.

7.2 Conclusion

Y-doped $BaZrO_3$ material suitable for sensing devices can be deposited by thin film technologies, such as sputtering and pulsed laser deposition (PLD). By using thin film technologies, we were able to demonstrate the potential to fabricate comparably cheap, mass produced devices with very small dimensions. Ba deficiency is observed in all deposited layers, however, is still poorly understood in these thin films. Initial results appear to indicate that the Ba is more easily backsputtered/etched from the surface it has been deposited on during ion bombardment, leading to nonstoichiometric concentration. Sputtered films have a higher sensitivity towards humidity at lower temperature (T = 400°C) with fast sensor response (τ_{60}) between 6 – 27 seconds and an average life time of 12 weeks. PLD films yielded more stoichiometric films with sensor response (τ_{60}) between 17 – 56 seconds and 1 year life time even at higher temperature (500°C ≤ T ≤ 650°C). Thin film devices produced by both methods were highly selective to water vapor at high temperature. Therefore, Yttrium-doped barium ziconate (Y-doped $BaZrO_3$ or YBZO) is a promising material for fast, sensitive, selective, and stable high temperature (400°C ≤ T ≤ 650°C) humidity sensors.

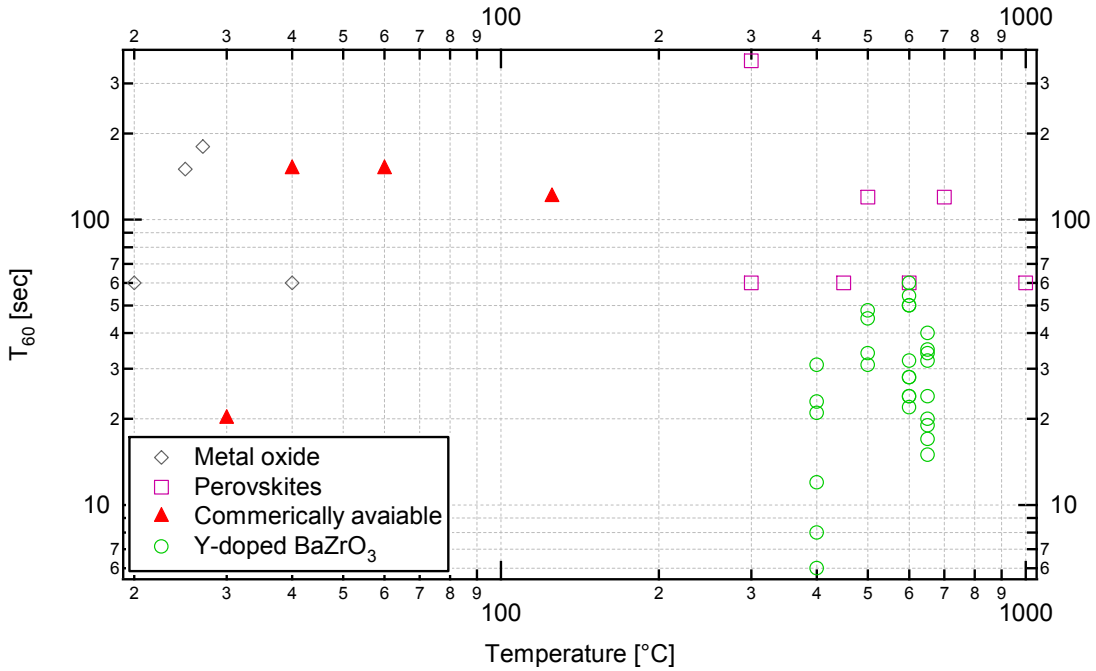

Fig. 7-1: Temperature vs. sensor response time of τ_{60} for some metal oxide, perovskite oxide, commercial avaiable humidity sensors based on Table 1-1, 1-2 and 1-3 in Chapter 1, and Y-doped $BaZrO_3$ thin film sensor devices that were presented in this work (Chapter 3, 4, 5, and 6)

7.3 Future work

Three principle issues should be addressed when continuing this work. First, we need to identify the reasons that caused the measured Ba deficiency in all deposited layers in order to control the film composition and understand better the correlation between deposition parameters and film compositions. Resputtering is a common mechanism that could cause Ba deficiency during the thin film deposition process. An initial resputtering effect has been studied and characterized as shown in Fig. 7-2. The XPS data are presented in Table 7-1. We have also observed changes of Ba atomic concentrations during XPS measurements when using different ion beam currents to etch the film surface for the same sample. This observation indicated that Ba could be removed more easily than other compounds by Ar^+.

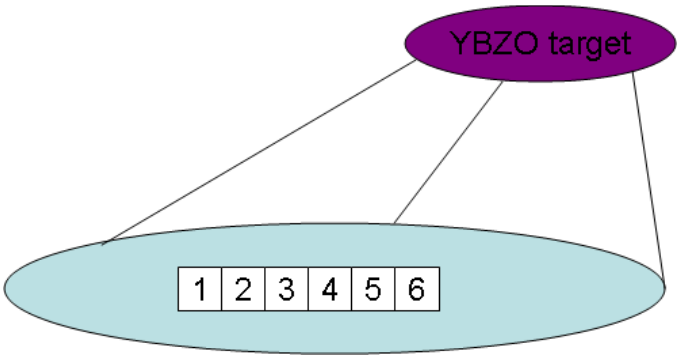

Fig. 7-2: Re-sputtering effect studies in Denton Discovery 18 system at room substrate temperature, yield film thickness of 130, 150, 180, 210, 220, and 285 nm from sample 1 to 6, respectively.

Table 7-1: XPS measurements for resputtering study samples after 4 mins Ar^+ etching

Sample Name	1 (130 nm)	2 (150 nm)	3 (180 nm)	4 (210 nm)	5 (220 nm)	6 (285 nm)
Ba 3d	6.37	7.37	10.50	11.15	9.23	7.76
O 1s	62.00	63.83	64.53	72.78	57.47	61.22
Zr 3p	21.99	20.02	17.96	4.14	24.95	21.41
Y 3p	7.55	7.18	4.52	7.26	6.51	6.46
Ar 2p	2.09	1.60	2.48	4.67	1.85	3.15

Thorough studies of resputtering are needed to determine whether this is the main reason for the Ba deficiency. Second, using Cr/Au recommended as the IDE test structure metal limits the operating temperature to below 1000°C. Previous YBZO bulk sample results have demonstrated a good repeatability and stable humidity response with Ti/Pt metal contact. In order to be able to test our sensors in a real combustion environment, we need to understand the differences 1) between our thin film sensors and the bulk film sensors, 2) interfaces transfer properties between YBZO material and Cr/Au or Ti/Pt. Third, impedance spectroscopy measurements should be carried out to help distinguish the conduction mechanisms and ion transfer mechanisms. Protons, oxygen ions, electrons, and electron-holes are all contributing to the electrical conductivity based on our knowledge.

It is however very difficult to separate each contribution for the total conductivity. And also surface ion exchange appeared to occur with bulk diffusion at the same time. Impedance spectroscopy measurements of the material would allow partial analysis of the role of the grain size and boundaries to the electrical conduction mechanism. It may also help identify the extent of the surface (or boundary layer) thickness of the material that dominates the sensing and current conducting mechanism further. If these data correlate with data obtained from the sensitivity and response time characterization as function of film thickness, this would further the understanding and support a model assuming a surface dominated mechanism. It would also possibly help quantify or at least estimate the thickness of this layer, thereby helping to maximize sensor response and performance and minimize processing time.